*"Our imagination is stretched to the utmost, not, as in fiction, to imagine things which are not really there, but just to comprehend those things which are there."*

Richard P. Feynman

*The Character of Physical Law (1965)*

# University of Alberta

PERFORMANCE EVALUATION OF SIGNAL CONDITIONING BOARDS AND SIMULATION OF THE IMPACT OF ELECTRONICS NOISE ON THE DEAP-3600 DARK MATTER DETECTOR

by

Rhys Timon Chouinard

A thesis submitted to the Faculty of Graduate Studies and Research
in partial fulfillment of the requirements for the degree of

Master of Science

Department of Physics


Spring 2013
Edmonton, Alberta

# Abstract

The Dark matter Experiment with Argon and Pulse shape discrimination (DEAP-3600) aims to detect the interactions of Weakly Interacting Massive Particles colliding with the nuclei of argon atoms. As particles interact with the argon in the DEAP-3600 vessel, scintillation light is emitted and detected by 255 photomultiplier tubes (PMTs) surrounding the target volume. Photons reaching the PMTs are converted into electrical pulses and sent along a data processing chain. The electronics are designed to maximise the detection of individual and multiple photon pulses, which is paramount for accurate particle identification. The Signal Conditioning Boards (SCBs) are electrical devices designed for DEAP-3600 to optimise single photoelectron detection, and maximise the signal to noise ratio. Versions of the SCBs were tested and improved to ensure the necessary signal to noise ratio was obtained. The impact of electronics noise on detector performance was studied.

# Acknowledgements

This thesis was completed while testing the limits of human ingestion of $C_8H_{10}N_4O_2$. A few people who made immeasurable contributions to my understanding of physics include: Aksel, Darren, Carsten, Craig, Pierre, Enrico, Wolfgang, Dick, Albert, David G., and Peter H. My computational and electronic abilities were honed by many, including Fabrice, Thomas Caldwell, Pierre, Paul Davis, and Rene Brun. The EDIT team had a profound influence on my desire to learn about the electrical substructure of particle physics experiments, and for that I am grateful to Thomas Jindra, Tara, Florian, Laura, and the rest who made the two weeks at Fermilab memorable. Many late nights and long hours were spent butchering ROOT macros until they bent to my will, and these experiences were often made bearable by office mates such as Zach, Logan, Tania, Sarah, and Chris S.

Outside of the academic arena, my support structure is composed of family and friends which kept me afloat admid rough seas. I am deeply indebted to Jason, Jared, Gillian, Brea, Quinne, Simone, Tyghe, Eily, Hawk, Adam, Cara, Jolene, and Heidi for their continued support. Finally, I need to thank Shalon McFarlane for providing the glue and rubber bands that at times holds my sanity together. You are my anchor to reality. I'll end with a quote by one of the great minds of the $31^{st}$ century:

*"And, now that I've found all the answers, I realise that what I was living for were the questions!"* - Professor H. J. Farnsworth

# Contents

# List of Tables

# List of Figures

# List of Abbreviations

List of commonly used abbreviations

| | |
|---|---|
| ADC | Analog to Digital Converter |
| AFG | Arbitrary Function Generator |
| AMU | Atomic Mass Units, ($1.66\times10^{-27}$ kg) |
| Bq | Becquerel, 1 decay/second (radioactivity) |
| CLEAN | Cryogenic Low Energy Astrophysics with Noble liquids |
| COBE | COsmic Background Explorer |
| CMB | Cosmic Microwave Background |
| COSMOS | Cosmic evolution survey |
| DAQ | Data Acquisition |
| DEAP | Dark matter Experiment with Argon and Pulse shape discrimination |
| DSPE | Digital Single Photoelectron detection |
| eV | electronVolt, $1.6\times10^{-19}$ Joules |
| GEANT | GEometry ANd Tracking software |
| GeV | Giga-electronVolt |
| GR | General Relativity |
| HQE | High Quantum Efficiency |
| HG | High Gain |
| HV | High Voltage |
| keVee | kilo-electronVolts electron equivalent |
| kg | kilogram |
| kpc | kiloparsec ($3.086\times10^{19}$ m) |
| LAr | Liquid Argon |

| | |
|---|---|
| LED | Light Emitting Diode |
| LET | Linear Energy Transfer |
| LG | Low Gain |
| LNGS | Laboratori Nazional del Gran Sasso |
| LSP | Lightest SuperSymmetric particle |
| LUX | Large Underground Xenon Experiment |
| MIDAS | Maximum Integration Data Acquisition System |
| mm | millimetres |
| Mpc | Megaparsec ($3.086\times10^{22}$ m) |
| mV | milliVolt |
| NDF | Number of Degrees of Freedom |
| Ne | Neon |
| NGC | New General Catalogue of Nebula and Clusters of Stars |
| nF | nanoFarads (capacitance) |
| NPE | Number of Photoelectrons |
| PCIe | Peripheral Component Interconnect express |
| PHD | Pulse Height Distribution |
| ppm | parts per million |
| PMT | Photomultiplier Tube |
| PSD | Pulse Shape Discrimination |
| RAT | Reactor Analysis Tool (Simulation software) |
| ROI | Region of Interest |
| RMS | Root Mean Square |
| SCB | Signal Conditioning Board |
| SM | Standard Model of Physics |
| S2N/SNR | Signal to Noise Ratio |
| SHV | Secure High Voltage |
| SNO | Sudbury Neutrino Observatory |

| | |
|---|---|
| SPE | Single Photoelectron |
| SHM | Standard Halo Model |
| SUSY | SuperSymmetry |
| TeV | Tera-electronVolt |
| TPB | Tetraphenyl Butadiene |
| UV | Ultra-Violet |
| Vpp | Voltage peak to peak |
| WF | Waveform |
| WIMP | Weakly Interacting Massive Particle |
| WMAP | Wilkinson Microwave Anisotropy Probe |
| Xe | Xenon |

# List of Symbols

List of commonly used symbols

| | |
|---|---|
| $\alpha$ | $^4$He nucleus |
| $^{39}$Ar | radioactive isotope of argon |
| $A$ | atomic mass number |
| $\beta$ | electron (particle) |
| c | speed of light, 299 792 458 m·s$^{-1}$ |
| C | Coulomb |
| $\chi$ | dark matter particle (WIMP) |
| $\epsilon$ | energy detection efficiency |
| $E_R$ | recoil energy of nucleus |
| $EV_{QPE}$ | reconstructed event energy |
| $H$ | Hubble's constant |
| $h$ | Planck's Constant, $6.626\times10^{-34}$ J·s |
| $\lambda$ | wavelength |
| LY | light yield (PE/keV) |
| $\Lambda_{CDM}$ | model explaining astrophysical data |
| $MC_{KE}$ | simulated event energy |
| $\mu_N$ | reduced mass of WIMP-nucleon system |
| $n$ | bit resolution |

| | |
|---|---|
| $\nu$ | frequency (light) |
| $\bar{\nu}$ | anti-neutrino |
| $\theta$ | scattering angle, centre of mass frame |
| $\Omega_{DM}$ | current dark matter fraction of universe |
| $q$ | charge on an electron, $1.6\times10^{-19}$ C |
| $QPE$ | detected photoelectrons |
| $\rho$ | dark matter density |
| $R$ | digitiser resolution |
| r | radius from centre of DEAP-3600 |
| $\sigma$ | velocity dispersion |
| $\sigma_{ann}$ | annihilation cross section for dark matter |
| $\sigma_0^{SI}$ | spin-independent cross section |
| $\sigma_{4ns}$ | 4 ns noise distribution standard deviation |
| $\sigma_{200ns}$ | 200 ns noise distribution standard deviation |
| $\tau$ | time constant |
| T | temperature |
| $v$ | dark matter velocity |
| $v_{lag}$ | velocity of Earth relative to Galactic Centre |
| $v_{sun}$ | velocity of Sun around center of galaxy |
| $V_D$ | dynamic range |
| $Z$ | number of protons |

# Chapter 1

# Introduction

Identification of dark matter remains one of the most important unresolved challenges in particle astrophysics. When astronomers observe the night sky they find overwhelming evidence for a particulate component of the Universe which does not interact electromagnetically. This unseen dark matter is revealed via the gravitational effect on the motions of astrophysical objects. It is thought to make up about 23% of the Universe. Evidence for the existence of dark matter comes in many forms. The earliest evidence was found during the 1930s from observations of a cluster of eight gravitationally bound galaxies, known as the Coma cluster. Based on the observed amount of luminous matter, galaxies in this cluster have velocities relative to one another which are too large for the cluster to remain gravitationally bound. Hence, some other unseen matter must be contributing to the cluster mass. Fritz Zwicky first referred to this as "*dunkle materie*", or dark matter [1].

Four decades later, additional evidence for dark matter was unveiled from a study of galactic rotation curves, which revealed a discrepancy in the amount of matter expected due to rotational velocities of stars and the amount of observed baryonic matter. Fast forward two decades and advances in the field of astrophysics permitted the study of temperature anisotropies in the Cosmic Microwave Background Radiation (CMB), providing information about the density anisotropies in the Universe when matter and radiation decoupled. A complete model, known as $\Lambda_{CDM}$, explains the CMB temperature anisotropies, the observations of supernovae (that also demonstrate a flat curvature for the Universe), and the large scale structure of galaxies. The $\Lambda_{CDM}$ model has parameters which separate the contribution of baryonic matter from the total matter in the Universe [2]. The best fit parameters show a discrepancy between the amount of baryonic matter and total amount of matter, which is in agreement with the amount of visible matter and dark matter observed [3]. Thus dark matter is postulated as some yet undiscovered form of non-baryonic matter.

Particle physics offers many theories beyond the Standard Model (SM) that predict particles with characteristics of potential dark matter candidates. SuperSymmetry (SUSY) is a theory which predicts that each standard model fermion has a heavier counterpart boson, and each standard model boson has a heavier counterpart fermion. These superpartners assist in explaining the hierarchy problem of why the mass of the Higgs boson is so much lower than the Planck mass scale. Many SUSY models predict a light, stable particle which is weakly interacting and has a mass that could explain the astrophysical observations of dark matter. This lightest supersymmetric particle (LSP), also known as the neutralino, is a leading dark matter candidate.

If one assumes dark matter was produced in the Big Bang and was in thermal equilibrium with normal matter, its annihilation cross section may be estimated. It is often referred to as the "WIMP miracle" [4] that an annihilation cross section on the order of the weak interaction scale provides a value consistent with the currently observed abundance of dark matter. This remarkable coincidence is an enticing hint that the dark matter particle may be weakly interacting with a mass ranging between 50 and 250 times the mass of the proton. A Weakly Interacting Massive Particle (or "WIMP") with these characteristics would explain both the temperature anisotropy distribution of the CMB and have the currently observed relic abundance.

Located two kilometres underground in Vale's Creighton mine near Sudbury, Ontario, Canada, DEAP-3600 will be one of the world's first tonne-scale direct detection dark matter experiments. The project seeks to capture evidence of WIMPs by observing the energy associated with nuclear recoils of dark matter particles that scatter from the nuclei of argon atoms.

This thesis outlines the development of the DEAP photomultiplier tube (PMT) Signal Conditioning Boards (SCBs). Developed at the University of Alberta, the SCBs are used to optimise the single photoelectron (SPE) detection efficiency of the DEAP-3600 PMTs. Chapter 2 of this thesis describes the dark matter problem, providing explanations of the gravitational evidence for WIMPs as well as the particle physics motivations for the neutralino. It ends with a short discussion on liquid noble detectors and their role in the direct detection of dark matter. In Chapter 3 an overview of the DEAP-3600 detector is given, and the electronic architecture of DEAP-3600 is described. SCBs and their role in enhancing the efficiency of DEAP-3600 are discussed. Chapter 4 discusses the results of commissioning two of the SCB versions. Key results pertaining to the performance of the SCBs will be discussed, including single photoelectron pulse heights, noise distributions, signal to noise ratios, and high gain vs low gain channel pulse height correlation. Chapter 5 presents simulation results that utilise input from the SCB tests to perform an accurate and realistic account of the expected effect of electronics noise on the pulse shape discrimination capability of DEAP-3600. The final chapter provides a brief summary of the results in the context of the SCB's impact on the performance of DEAP-3600. It also discusses DEAP-3600's projected sensitivity in terms of WIMP mass versus cross section and outlines the direction of future work related to the findings of this thesis.

# Chapter 2

# Evidence for Dark Matter and Liquid Noble Gas Detectors

At the time of writing this thesis, the matter/energy density of the Universe may be divided into the following approximate proportions [5]:

- 73% dark energy,
- 23% dark matter,
- 4% baryonic matter.

The vast majority of the energy density of the Universe (namely the dark component) remains yet to be directly measured. Since only the baryonic component has been identified, the nature of dark matter and dark energy are two of the most important unresolved problems in particle astrophysics. The existence of dark matter has been inferred from its gravitational effects on visible matter, from the galactic scale up to large galaxy clusters [6]. Dark matter has been postulated to be particulate in nature, and a favoured candidate is the non-baryonic Weakly Interacting Massive Particle, or WIMP for short. WIMPs are expected to interact via the weak force and gravity, but not participate in electromagnetic or strong interactions. The following sections outline observations that have provided indirect evidence for dark matter, discuss the issue of why WIMPs are expected to make up a component of dark matter, and evaluate their possible interactions. An overview of liquid noble dark matter experiments is included, as well as a brief description of single phase and dual phase detectors.

## 2.1 Evidence for Dark Matter

### 2.1.1 Galactic Rotation Curves

An early indication of dark matter originated from the study of galactic rotation curves. The measured velocity of stars (or gas clouds) versus the distance from the centre of the galaxy provides a distribution that may be represented by the virial theorem. If the mass of a galaxy consists entirely of luminous matter, most of the mass would be located in the central region, near the bulge, where the density of stars and gas is largest. In this scenario stars at the outer radii of the galaxy should rotate more slowly than the stars near the centre. This is analogous to the planets at the outer edge of the solar system which orbit slower than the inner planets due to their distance from the centre of mass of the system. However, the observed velocity of stars at the outer radii of spiral galaxies are found to be similar to those of stars at inner radii [7] (see Figure 2.1, showing the galactic rotation curve of NGC 3198). To prevent the outer stars from being ejected from the galaxy there must be additional matter at large radii which is contributing to the total mass of the galaxy. When the rotation curves of galaxies are compared to the Keplerian expectation, there exists a discrepancy that may be explained by assuming a dark matter component that forms a spherical halo distribution around the galaxy. This dark matter halo, when combined with the visible matter in the disk, results in a rotation curve that agrees with the experimental data. The rotational speed of luminous matter in one galaxy is shown on the y-axis of Figure 2.1 in $\mathrm{km{\cdot}s^{-1}}$, while the radius from the centre at which that matter is located is shown on the x-axis in units of kiloparsecs. The data points are shown to fit well with the top curve, which is the combination of a contribution from a dark matter halo component and (visible matter) disk component. The individual contributions are shown in the lower curves for clarity.

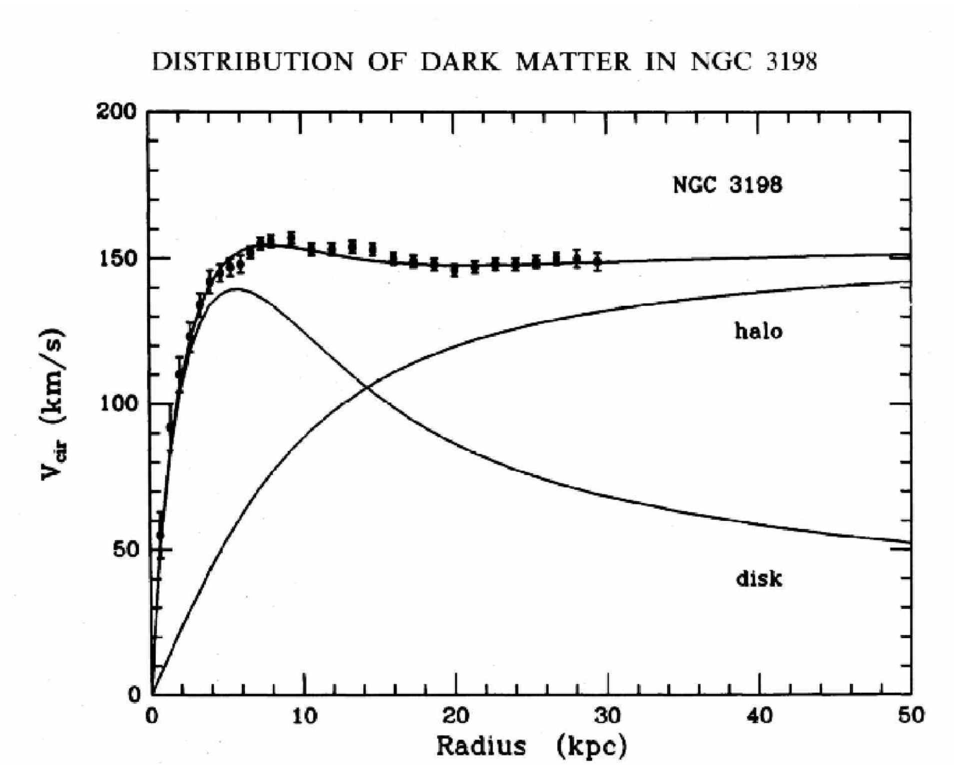


Figure 2.1: Galactic rotation curve of NGC 3198 [8]. The rotational velocity of hydrogen gas clouds are plotted versus their radius from the centre of the galaxy in kiloparsecs [9]. The data points are fit well to a combination of the visible matter in the disk plus a dark matter halo component.

Different types of galaxies display different rotation curves, but most galaxies studied show evidence for a dark matter component in some form [10]. Figure 2.2 shows families of rotation curves of four individual classes of galaxies. Although these galaxies have a variety of shapes, sizes, and average rotational speeds, they all display some evidence for dark matter as indicated by the flat rotation curve at large radii.

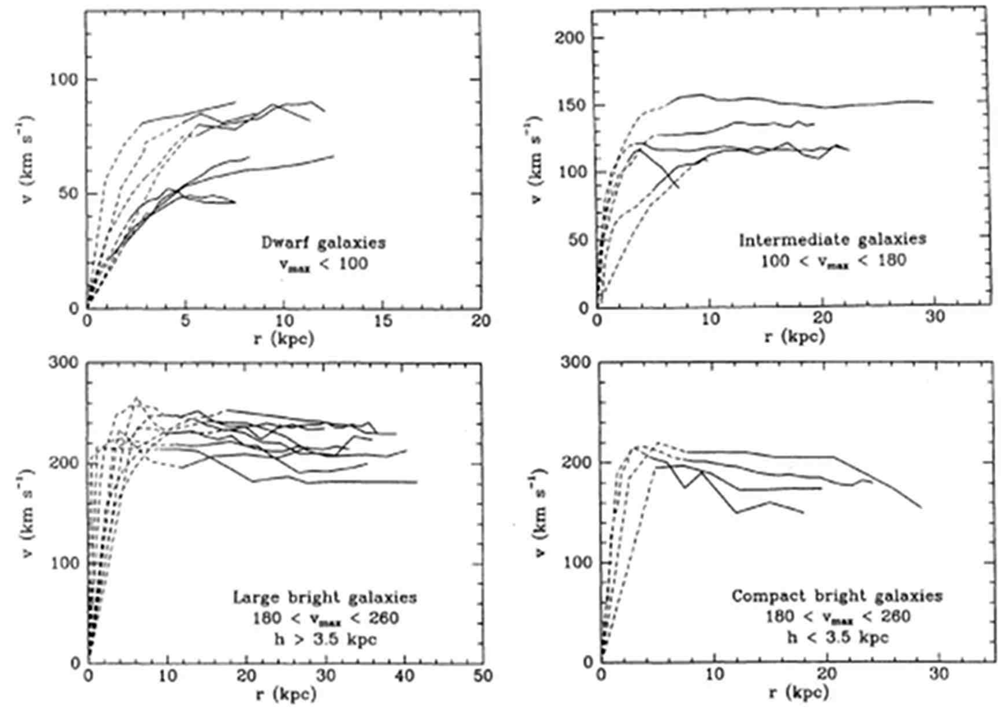


Figure 2.2: Velocity curves of different galaxy types [11]. All galaxies show a rotation velocity distribution that flattens out as radius increases, an indication of a dark matter component.

### 2.1.2 Gravitational Lensing

Einstein's theory of general relativity (GR) states that anything with mass (or energy) will distort 4-dimensional Euclidean space-time, causing light paths to bend. It was among the first successfully demonstrated predictions of GR, following the explanation of the perihelion precession of Mercury. In an astronomical context, the large amounts of matter that create gravitational fields which produce noticeable lensing effects are typically stars, galaxies, or cluster of galaxies. When photons travel through this region of distorted space-time, their path is deflected to travel along the shortest path in space-time. This is similar to the deflection caused when light passes through a lens, hence the term "gravitational lensing" [12]. A schematic showing gravitational lensing of a distant galaxy as seen on Earth is shown in Figure 2.3.

Gravitational lensing was first observed during a solar eclipse in the year

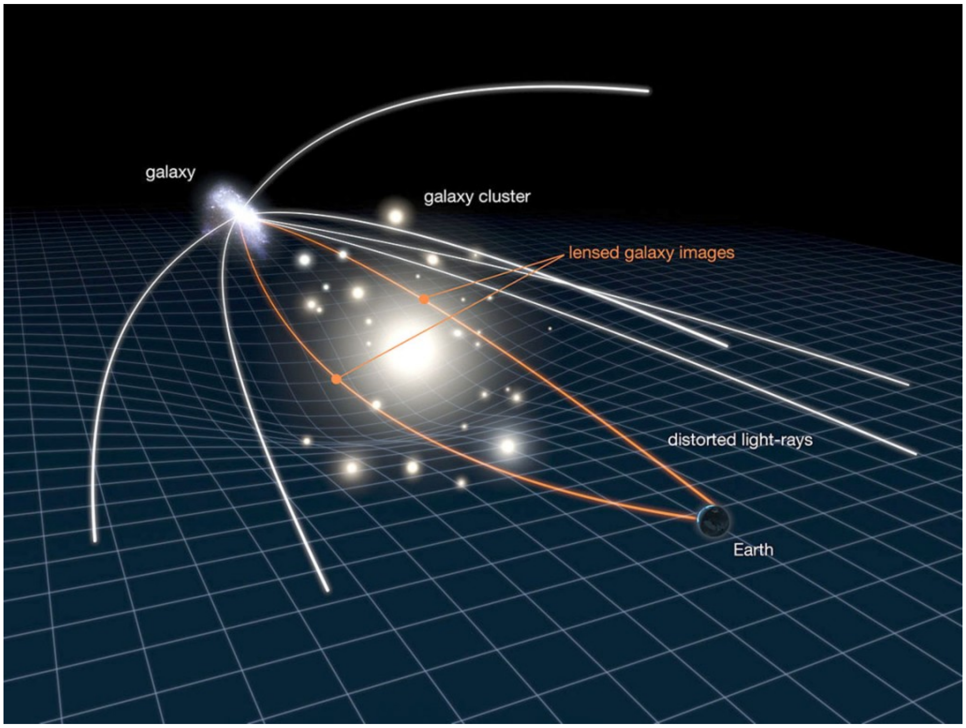


Figure 2.3: A graphical representation of light from a distant galaxy being gravitationally lensed by an intermediate galaxy cluster, with the light being detected at Earth. Illustration credit: NASA, ESA & L. Calada [13].

1919 [14]. However, it was not until the advent of powerful space-based telescopes in the 1990s that the true power of gravitational lensing as an astronomical tool was brought into focus [15].

If a large amount of matter is situated between the Earth and a distant galaxy, the light from the distant galaxy may be deflected by the galaxy cluster and observed on Earth when it otherwise would not be observed. The ability of the light to reach Earth is due to the increased number of paths from the source created by the gravitational lense (see Figure 2.3). If the galaxy being lensed is not directly behind the lensing galaxy, the light from distant galaxy will be seen as arcs of light by the observer on Earth. Figure 2.4 shows an image of the galaxy cluster Abell 2218 taken by the Hubble Space Telescope. The circular arcs of light seen surrounding the bright cluster on the left of the figure are gravitationally lensed images of a distant galaxy.

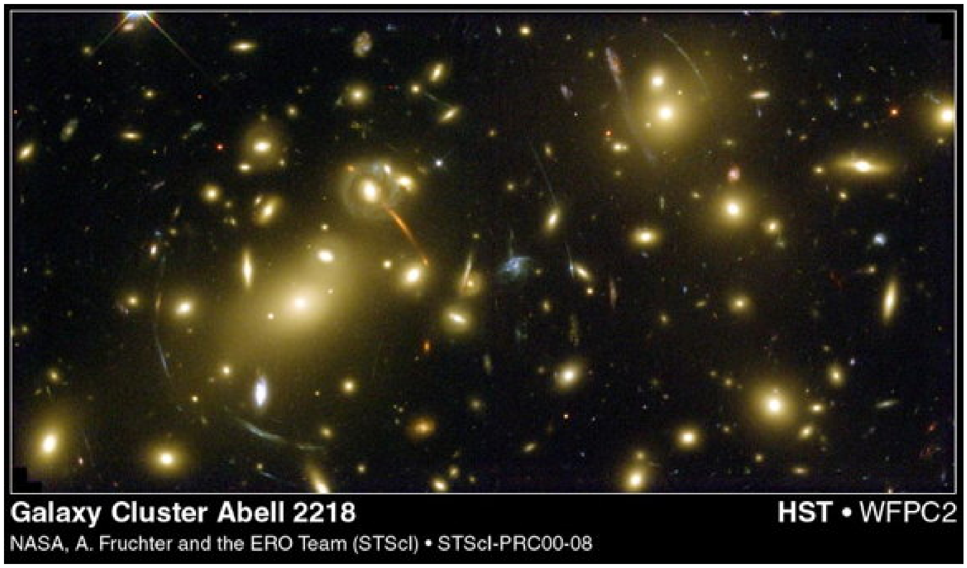


Figure 2.4: Shown are the arcs created by the galaxy cluster Abell 2218 gravitationally lensing the light from galaxies behind the cluster [16].

The degree of gravitational lensing is directly proportional to the mass of the objects causing it. By observing distant galaxies which are being lensed over a period of time, astronomers are able to create maps of the mass distribution of the lensing objects. The distribution of mass may then be compared to the location and amount of luminous matter. In many cases the mass of the lensing galaxy is much greater than can be accounted for by the baryonic component, indicating some other unseen mass contribution [17].

Figure 2.5 shows an image of the Bullet Cluster, a pair of galaxy clusters that have recently undergone a collision which led to the separation of the baryonic matter from the dark matter halos. One interpretation of the image is that the baryonic matter from the two galaxy clusters interacted electromagnetically during the collision, causing the gas to slow down, heat up, and emit x-rays which were detected at Earth. However, the dark matter halos from each galaxy (where most of the mass is situated) did not interact during the collision, and the two halos simply passed through each other unimpeded. The separation between the dark matter halo and baryonic components of the cluster caused by the collision is shown by generating mass distribution maps.

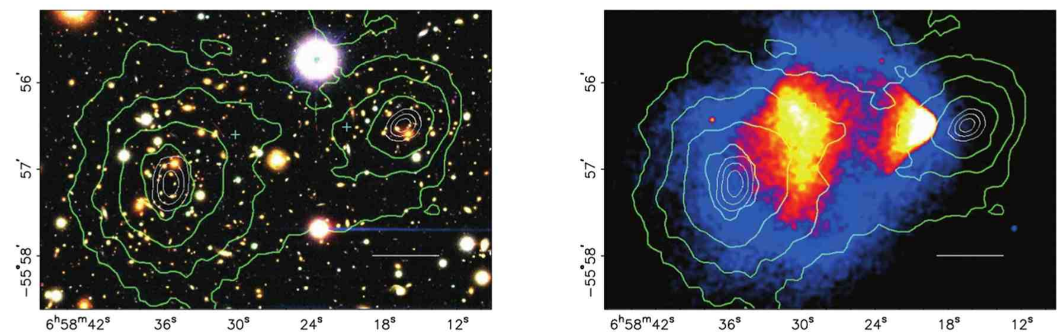


Figure 2.5: Map of the baryonic matter of two colliding galaxies (show in red on right side) and the reconstructed centres of the mass distributions as determined via gravitational lensing (green contour maps in both images). The baryonic matter has reduced velocity during the collision due to electromagnetic interactions, while the dark matter halos are observed to pass through each other, separating from the ordinary matter [18].

The majority of the mass, represented by dark matter and shown by the green contours, has been separated from the electromagnetically interacting hot gas (shown on the right in red).

### 2.1.3 Large Scale Structure

The evolution of large scale structures in the Universe (such as galaxies and galactic clusters) is influenced by mass density fluctuations present after the Big Bang, which permits an independent measurement of the total fraction of dark matter in the Universe. Figure 2.6 shows a 3-dimensional map of the dark matter distribution as a function of time. This map was generated by analysing data from the COSMOS survey, performed by the Hubble Space Telescope. Left to right in the image represents time, with the left part of the map being later times in the Universe's evolution. Further in the past dark matter was more evenly distributed, as indicated by a lack of clumping of galaxies. As time progresses the dark matter gradually contracts into specific regions due to gravitational interactions, which are consistent with the locations of light emitting galaxies.

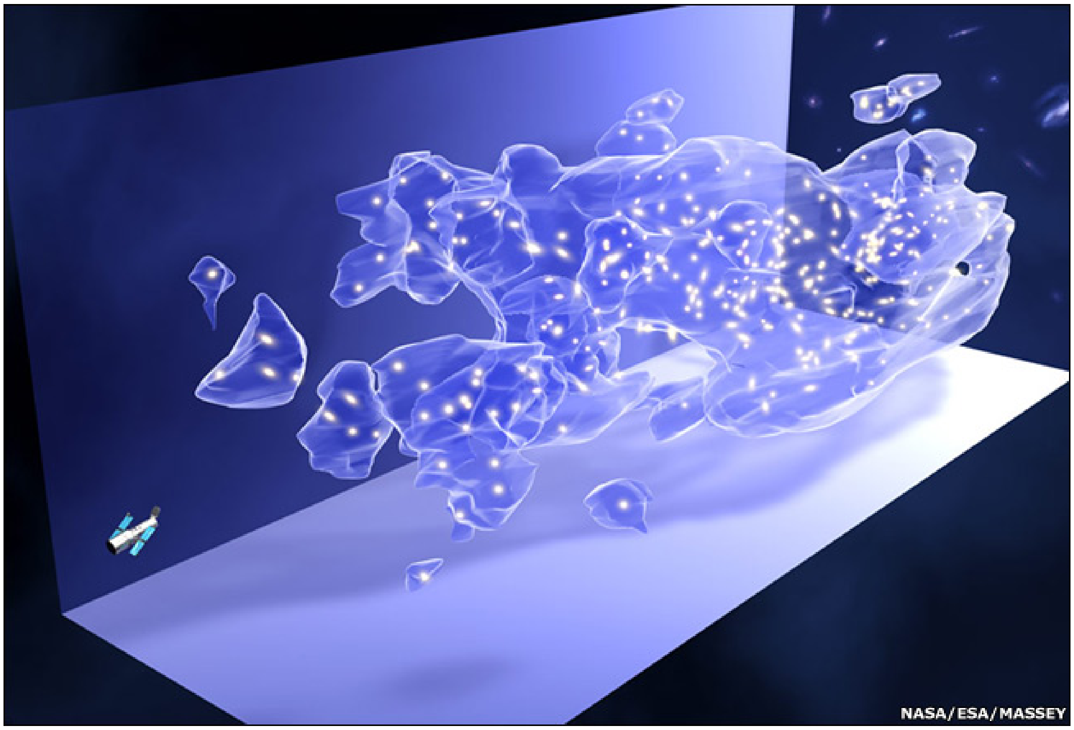


Figure 2.6: The COSMOS survey 3-dimensional dark matter map. Earlier in time (right), dark matter is more evenly distributed. As time increases (moving left) the dark matter begins to collect into structures due to gravitational attraction [19].

Figure 2.7 shows an image of a distribution of dark matter generated from gravitational lensing surveys using the Hubble Space Telescope (right), as well as a distribution of baryonic matter (left) from the same region of sky. Comparing the distributions shows the two types of matter are co-located, reinforcing the idea that the gravitational potential from localised dark matter overdensities in the early Universe trapped primordial gas, which later formed stars and galaxies, leading to the large scale structure of visible matter. The filament structure observed was also found to be a good match to the results of n-body simulations of large scale structure formation which was dominated by gravitational collapse from dark matter in the early Universe [20, 21].

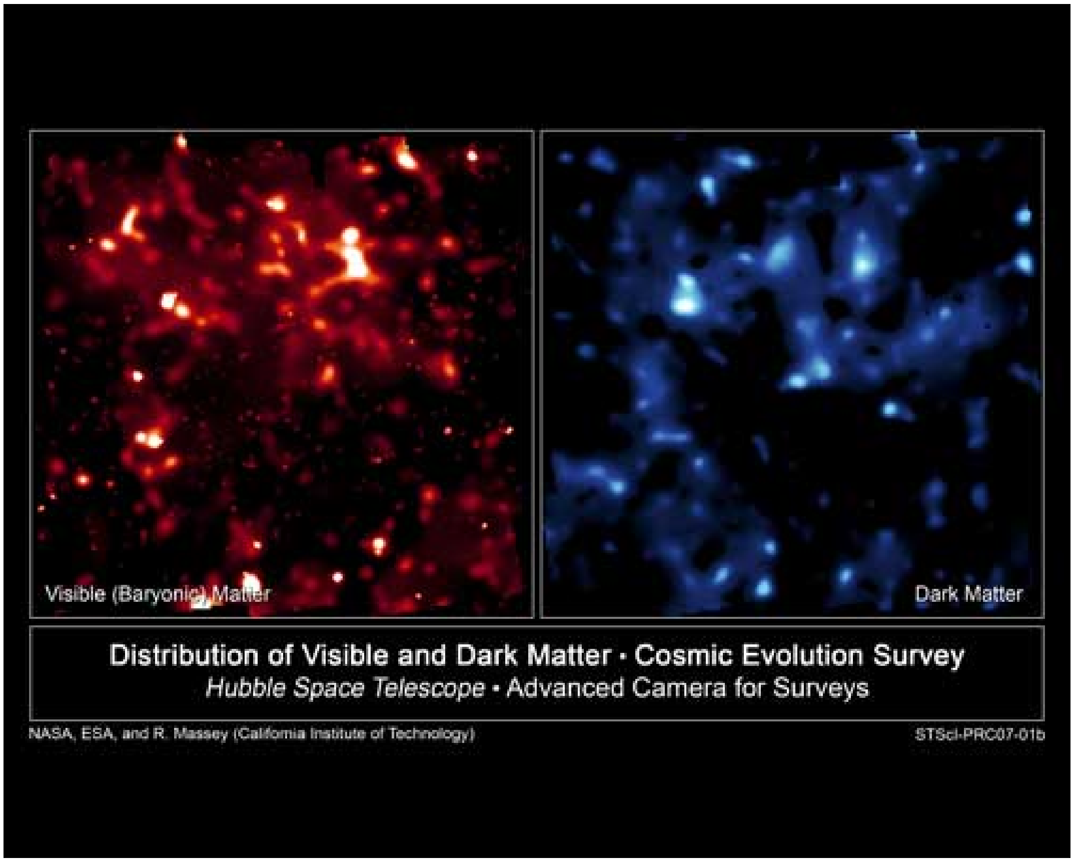


Figure 2.7: Luminous matter (left) and dark matter (right) mass distributions as deduced by the Hubble Space Telescope [19]. The two types of matter are co-located, indicating dark matter plays a role in galactic evolution.

### 2.1.4 Cosmic Microwave Background

The Cosmic Microwave Background (CMB) comprises relic photons which are remnants from the Big Bang. Immediately after the Big Bang the Universe was extremely hot and dense, and as a result electrons were not able to bind with protons. This led to light scattering from the ionised plasma that permeated the Universe. Due to this coupling of matter and photons the scattering length of light was very short, and the Universe was essentially opaque. Roughly 380,000 years after the Big Bang the Universe had expanded and cooled to a point that electrons could bind with protons, forming stable atoms [22]. At this time of de-coupling the Universe became transparent to photons. Photons released at the time of last scattering are gradually red-shifted as the Universe expands, and at the present day their wavelength is predominantly on the order of millimetres (microwave). The spectral distribution of CMB photons follows a blackbody distribution (Planck's Law), corresponding to a temperature of 2.726 K. Satellite experiments measuring the CMB, such as the Cosmic Background Explorer (COBE) and the Wilkinson Microwave Anisotropy Probe (WMAP), have determined that the Universe has a nearly isotropic temperature distribution, with minor fluctuations on the order of tens of microkelvin [23]. The size of the temperature fluctuations may be used to extrapolate information about the total and baryonic matter densities at the time of decoupling. Temperature anisotropies are usually expanded using spherical harmonics $Y_{lm}(\theta, \phi)$ [24]:

$$\frac{\delta T}{T}(\theta, \phi) = \sum_{l=2}^{\infty} \sum_{m=-l}^{+l} a_{lm} Y_{lm}(\theta, \phi) \ . \tag{2.1}$$

The variance of $a_{lm}$ is given by:

$$C_l \quad \equiv \quad \langle |a_{lm}|^2 \rangle \quad \equiv \quad \frac{1}{2l+1} \sum_{m=-l}^{l} |a_{lm}|^2 \ . \tag{2.2}$$

A Universe which is statistically isotropic implies that all values of $m$ are equivalent, meaning there is no preferred length scales [25]. Combining this with the assumption of Gaussian temperature fluctuations, the CMB temperature anisotropies can be plotted as a power spectrum, which shows how $C_{lm}$ varies with $l$.

Figure 2.8 shows a power spectrum, where $l(l{+}1)\mathrm{C}_l/2\pi$ is plotted versus $l$. The red line shows the $\Lambda_{CDM}$ six parameter model fit to the WMAP data. The results of the fit give the following abundances of matter and baryons [24]:

$$\Omega_m H^2 = 0.14 \pm 0.02 \qquad\qquad \Omega_b H^2 = 0.024 \pm 0.001, \tag{2.3}$$

where $H$ is Hubble's constant in units of 100 km$\cdot$s$^{-1}\cdot$Mpc$^{-1}$ (value $\approx$ 0.7). These results indicate the baryonic mass density of the Universe ($\Omega_b$) is in-

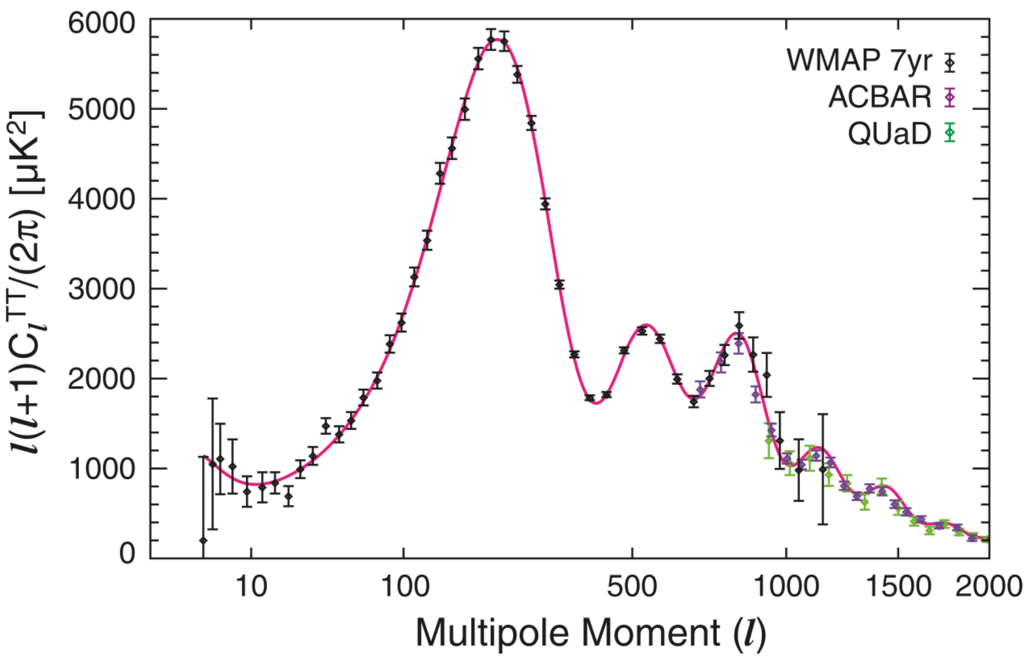


Figure 2.8: CMB temperature anisotropy power spectrum from various experiments. Red line shows a fit of the six parameter $\Lambda_{CDM}$ model to WMAP data for a flat Universe [26].

sufficient to account for the total mass density ($\Omega_m$), reinforcing the idea of a non-baryonic dark matter component of the Universe, which is entirely independent from the study of galactic rotation curves and gravitational lensing.

## 2.2 WIMP Dark Matter

### 2.2.1 Relic Density

A favoured candidate for dark matter is the Weakly Interacting Massive Particle. If WIMPs were produced in thermal equilibrium during the early stages of the Universe, followed by a freeze-out at the appropriate abundance due to a weak self-interaction cross section, then they would currently have an abundance that agrees well with the measured value for dark matter [24]. An approximation for the present relic density of dark matter is given by:

$$\Omega_{DM} H^2 \approx \frac{3 \times 10^{-27}\ \mathrm{cm^3 s^{-1}}}{\langle \sigma_{ann} v \rangle} \tag{2.4}$$

where $\Omega_{DM}$ is the current relic density, $\sigma_{ann}$ is the dark matter annihilation cross section, and $v$ is the average particle velocity [24]. Assuming $\Omega_{DM} \approx 0.25$ one obtains:

$$\langle \sigma_{ann} v \rangle \approx \frac{3 \times 10^{-27}\ \mathrm{cm^3 s^{-1}}}{0.1} = 3 \times 10^{-26}\ \mathrm{cm^3 s^{-1}}\ . \tag{2.5}$$

For a particle to be a viable candidate for dark matter, it must be heavy enough to have been moving non-relativistically at the time of galaxy formation. Considering a particle with a mass of around 100 GeV·c$^{-2}$ and an average velocity relative to Earth of about 270 km·s$^{-1}$ [27], the cross section obtained is

$$\langle \sigma_{ann} \rangle \approx 1 \times 10^{-33}\ \mathrm{cm^2}\ , \tag{2.6}$$

which is a typical cross section of weak interactions [28]. Dark matter particles being heavy, $O(10^2)$ to $O(10^3)$ GeV·c$^{-2}$, and weakly interacting allows them to fit the requirements of the observed relic density, and led to the name "WIMPs".

### 2.2.2 SuperSymmetry

The Standard Model of particle physics does not predict any viable dark matter particles. Extensions to the Standard Model have been proposed in attempts to solve the hierarchy problem: the challenge of why the Planck mass, $O(10^{19})$ GeV·c$^{-2}$, is many orders of magnitude greater than the physical mass of the Higgs boson, $O(10^2)$ GeV·c$^{-2}$ [29]. SuperSymmetry (SUSY) is an extension to the Standard Model which potentially solves the hierarchy problem by introducing super-partners to all Standard Model particles which are greater in mass and possess a spin which differs from their Standard Model counterparts by one-half. This implies that all Standard Model fermions have boson super-partners, and all standard model bosons have fermion super-partners. SUSY is also appealing because it makes a prediction that the electromagnetic, strong, and weak forces all unify at an energy near $10^{16}$ GeV [30]. Grand Unification would mean all of the fundamental interactions excluding gravity are effectively manifestations of the same force.

Most SUSY theories introduce a new conserved quantity known as R-parity:

$$R = (-1)^{3(B-L)+2S} \tag{2.7}$$

where B is the baryon number, L is the lepton number, and S is the spin. Standard Model particles have even R-parity, whereas supersymmetric partners have odd R-parity. Conserving R-parity in decay and scattering processes implies that supersymmetric particles may be generated in pairs and will decay into lighter states. The lightest supersymmetric particle, called the neutralino, must be stable since it is the end product of the decay of heavier, unstable SUSY particles [31, 30]. The neutralino should have a mass less than a few TeV and should interact weakly with ordinary matter, making it a viable candidate for the role of the WIMP. It is of interest to note that SUSY was postulated for reasons completely unrelated to dark matter, yet it provides candidates which could have the properties of WIMPs.

## 2.3 Dark Matter Direct Detection

Although there exists alternatives to direct detection of dark matter, known as indirect dark matter detection, only the former will be discussed in detail in this thesis. Note, however, that indirect detection experiments look for a signal of standard model particles created by self-annihilation or decay of dark matter particles, which may be detected on Earth. For a current review of the indirect search for dark matter, the reader is directed to [32]. This section begins by describing the astrophysical model assumptions used when calculating the WIMP interaction rates for direct detection experiments. WIMP interaction cross sections are described in the following subsection. The last two subsections, 2.3.3 and 2.3.4, explain some useful properties of liquid noble gases as dark matter interaction targets, and describe the difference between two general types of detectors (single and dual phase).

### 2.3.1 Astrophysical WIMP Model Assumptions

The galactic Standard Halo Model (SHM) for dark matter generally assumes the following parameters; a dark matter density ($\rho$) in the local neighbourhood of the solar system of 0.3 GeV$\cdot$cm$^{-3}$, and a rotational velocity of the sun around the centre of the galaxy $v_{sun}$ = 220 km$\cdot$s$^{-1}$. A velocity distribution of WIMPs relative to Earth that follows a Maxwell-Boltzmann distribution [27] is given by Equation 2.8;

$$f(\mathbf{v}) = \frac{C}{\sigma^3} \cdot exp\frac{-(\mathbf{v} - \mathbf{v}_{lag})^2}{2\sigma^2} \;, \tag{2.8}$$

where $\mathbf{v}_{lag}$ is a velocity parameter which incorporates the Earth's motion relative to the Galactic centre, $\sigma$ is the velocity dispersion of stars in the Milky Way, and C is a constant [33]. The average velocity value of 230 km$\cdot$s$^{-1}$ is often used for WIMP velocity relative to Earth (see Figure 2.9). The relative velocity of the WIMP particle is directly related to the interaction energy of the nuclear recoil events in direct detection experiments.

### 2.3.2 WIMP Interaction Cross Section

It is believed WIMPs ($\chi$) may be detected when they scatter elastically from a target nucleus. For the DEAP-3600 project, where argon is the target material, the interaction may simply be written as:

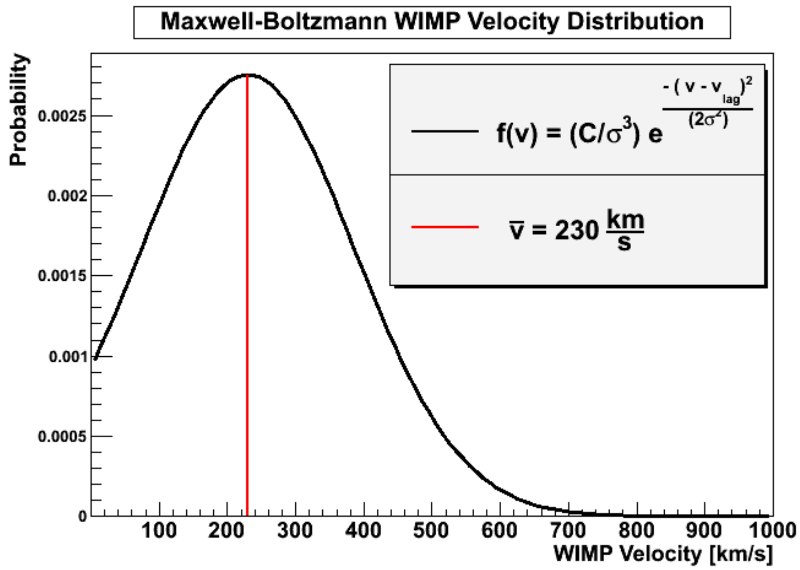


Figure 2.9: Maxwell-Boltzmann WIMP velocity distribution [33]. The red line indicates the most probable velocity.

$$\chi + Ar \to \chi' + Ar' \; . \tag{2.9}$$

The interaction with WIMPs may be axial-vector coupled (spin-dependent) or scalar (spin-independent). DEAP-3600 will be sensitive to WIMPs interacting via spin-independent (scalar) interactions. In many theoretical models the spin-independent WIMP interaction on a nucleus dominates over the spin-dependent interaction for nuclei with A $>$ 30. For the neutralino, and other WIMPs which interact primarily through Higgs exchange (see Figure 2.10), the spin-independent scalar coupling is roughly the same for protons and neutrons [34]. The cross section associated with the spin-independent interaction is given by:

$$\sigma_0^{SI} = \frac{4}{\pi}\mu_N^2[Zf_p + (A-Z)f_n]^2 \tag{2.10}$$

where $\mu_N = m_\chi m_N/(m_\chi + m_N)$ is the reduced mass of the WIMP-nucleus system, $f_{p,n}$ are the coupling of the WIMPs to protons/neutrons, A is atomic mass number, and Z is the number of protons in the target nucleus [34]. Tree level

Feynman diagrams providing the main contribution to the spin-independent elastic scattering interactions of neutralinos (WIMPs) on quarks are shown in Figure 2.10.

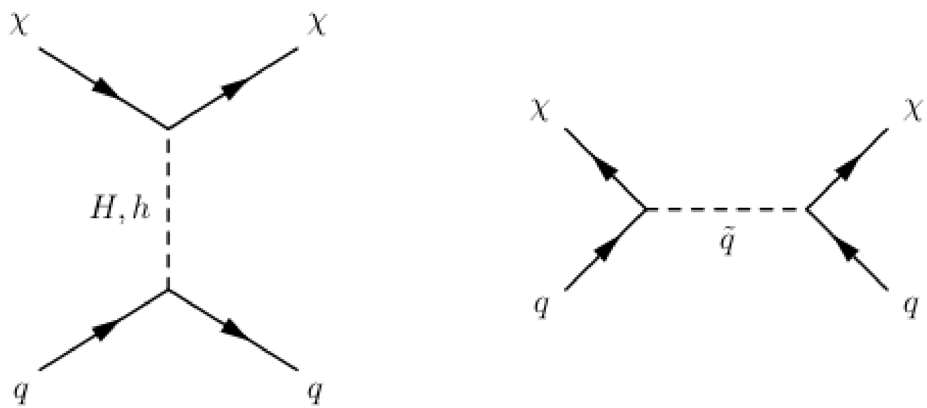


Figure 2.10: Tree level (first order) Feynman diagrams for spin-independent elastic scattering of neutralinos (WIMPs) on nuclei [30]. The t-channel Higgs exchange is shown on the left, while a s-channel squark exchange is shown on the right.

### 2.3.3 Liquid Noble Gases for Dark Matter Detection

Three liquid nobles gases (neon, xenon, and argon), are often considered for use in dark matter direct detection experiments due to their properties of being excellent scintillators with high light yields [35]. Krypton, a scintillator used in medical imaging and electromagnetic calorimeters, is omitted from dark matter considerations due to the activity of naturally occurring radioactive isotopes, including $^{85}$Kr and $^{81}$Kr. Key properties to consider when choosing a noble liquid for a target material are summarised in Table 2.1.

Other than properties of light yield and cost, the atomic weight, natural backgrounds, and ratio of singlet to triplet time constants guide the type of detector one may construct. As discussed in Section 2.3.4, the small difference for singlet and triplet time constants defines the possibility of a single phase, purely pulse shape discrimination based detector versus a dual phase

Table 2.1: Critical parameters of noble liquids considered for dark matter experiments [36, 37, 38, 39, 35]. Yield is defined as the number of generated scintillation photons per MeV of recoil energy (electron equivalent).

| Parameter | neon | argon | xenon |
|---|---|---|---|
| Yield (x$10^4$ photons/MeV) | 1.5 | 4.0 | 4.2 |
| Singlet time constant $\tau_1$ (ns) | 2.2 | 6 | 2.2 |
| Triplet time constant $\tau_3$ (ns) | 2900 | 1590 | 21 |
| Peak $\lambda$ (nm) emitted | 77 | 128 | 174 |
| Rayleigh scattering length (cm) | 60 | 90 | 60 |
| Approx. Price ($/kg) | 330 | 5 | 1200 |
| Atomic Weight (AMU) | 20.18 | 39.95 | 131.30 |
| Radioactivity | None | $^{39}$Ar 1Bq/kg | $^{136}$Xe $< 10\mu$Bq/kg |
| Fraction in Atmosphere [ppm] | 18.2 | 9340 | 0.09 |

experiment. Of these three noble liquids, only neon has no natural radioactive isotopes making it an attractive medium for rare event searches. However, its low atomic weight provides a smaller target for nuclear interactions, which may result in fewer WIMP events. Argon is found to have a high light yield relative to neon, a moderately sized nucleus (increasing the spin-independent cross section for nuclear interactions), and is the least expensive of the three noble liquids considered due to its relatively high natural abundance. It also has the largest Rayleigh scattering length, meaning a minimum amount of light is redirected as it traverses a target volume.

Figure 2.11 shows a plot of predicted number of WIMP events versus recoil energy for the three different noble gases considered. The calculation used to make this plot assumed a 100 GeV$\cdot$c$^{-2}$ mass WIMP with a cross section of $1.0\times10^{-45}$ cm$^2$, a live-time of three years and a fiducial mass of 1000 kg. Xenon's events at higher energies are suppressed due to a nuclear cross section form factor, but due to its larger nucleus it performs better at lower recoil energies [35]. Argon has a greater rate than neon for the entire range, and begins to exceed the xenon event rate above recoil energies near 50 keV.

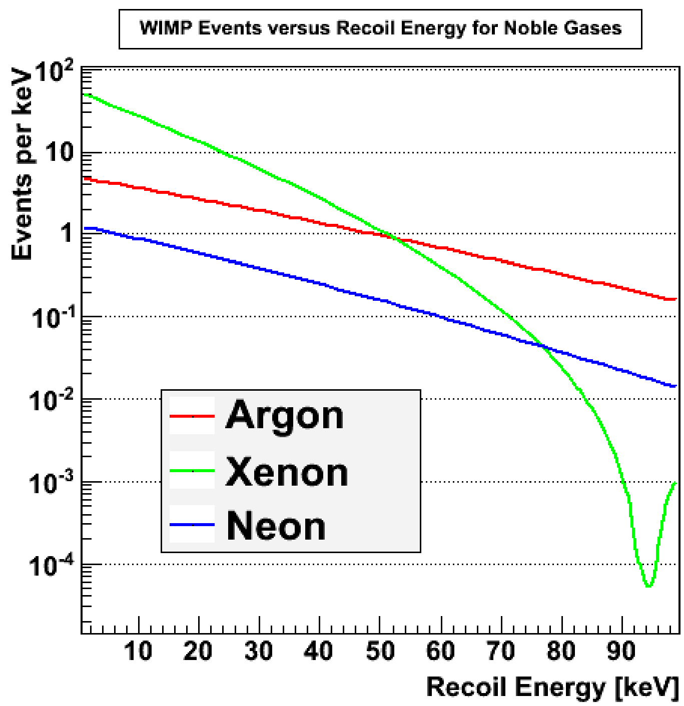


Figure 2.11: Predicted number of WIMP events per keV of recoil energy (assuming a 100 GeV$\cdot$c$^{-2}$ mass WIMP) for a 1000 kg fiducial mass detector operating for three years, assuming a WIMP spin-independent cross section of $1.0\times10^{-45}$ cm$^2$. This figure was produced using the Dark Matter Online Tools program [40].

### 2.3.4 Single Phase versus Dual Phase Detection

DEAP-3600 is designed to be one of the world's first tonne-scale single phase dark matter direct detectors. Single phase detectors rely solely on the scintillation light from particle interactions for event discrimination. This is contrasted with dual phase detectors, which have two signals: primary scintillation light from the particle interaction in a liquid, and a secondary ionisation signal from the electrons of the initial ionisation that are drifted in an electric field towards a gas phase. Figure 2.12 shows a schematic of a dual phase detector in operation, with the two different light signals being represented by the S1 and S2 on the right hand side graph. Using the ratio of the primary to secondary scintillation signal sizes, one may differentiate particle interaction types in a dual phase detector [41]. The current leading limit set on WIMP spin-independent interaction cross section as a function of mass is set by the dual phase experiment XENON100, operated at Laboratori Nazional del Gran Sasso (LNGS) in Italy [42].

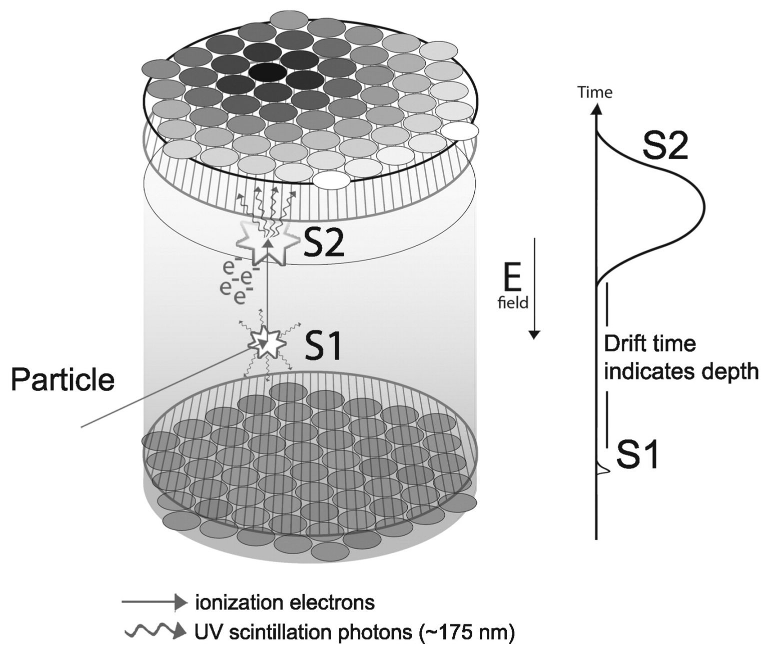


Figure 2.12: Schematic of the dual phase dark matter detector LUX, which will use liquid xenon [43].

Dual phase detectors have the challenge of requiring an electric field within the detection medium. Thus, additional materials (including metals) need to be brought closer to the target volume, which increases the likelihood of background events. It is also argued that single phase detectors are easier to scale to larger sizes since they can be created in spherical geometries which maximises the volume of target material contained per square meter of surface area. This spherical geometry maximises self-shielding of the target materials, and facilitates increased photocathode coverage by allowing photomultiplier tubes (PMTs) to surround the detector. In contrast, dual phase detectors are typically cylindrical in geometry to facilitate the electric field and secondary gas phase. With this design, a dual phase detector has increasing difficulty achieving uniformity in the electric field needed for the electron drifting as the detector size is increased. Dual phase detectors typically have PMTs situated only at the top and bottom of the detector, and as a result the detectors sacrifice photocoverage for the benefit of the secondary ionisation signal. However, due to the cylindrical geometry dual phase detectors have excellent position reconstruction, allowing for very precise fiducialisation.

In a single phase detector like DEAP, discrimination between types of particle interactions arise from the differences in the pulse shape between nuclear recoils and electromagnetic events. The in-depth discussion of pulse shape discrimination in DEAP-3600 is deferred to Chapter 3. When the noble liquid is ionised from a particle interaction, the liquid forms excited dimer states in either the singlet or triplet configuration. The two states have distinct lifetimes and amplitudes. In argon, the triplet state has a time constant (the time it takes for a sample full of excited atoms to decay to $1/e$ of its original size) of 1.6 $\mu s$, while the singlet state has a time constant of 6 ns [36].

The scintillation light from a liquid noble gas comes from ionising radiation producing excitons $N^*$ (Equation 2.11) and ions $N^+$ (Equation 2.12) [44]:

$$\begin{aligned} N^* + N + N &\rightarrow N_2^* + N, \\ N_2^* &\rightarrow 2N + h\nu \end{aligned} \tag{2.11}$$

$$\begin{aligned} N^+ + N &\rightarrow N_2^+, \\ N_2^+ + e^- &\rightarrow N^{**} + N, \\ N^{**} &\rightarrow N^* + heat, \\ N^* + N + N &\rightarrow N_2^* + N, \\ N_2^* &\rightarrow 2N + h\nu \end{aligned} \tag{2.12}$$

where $N^{**}$ decaying to $N^*$ and heat is a non-radiation transition, and $h\nu$

denotes the ultraviolet photon emitted by the noble gas. Once the ultraviolet photons are emitted they traverse the detector and are either detected directly by PMTs or converted into photons of longer wavelength and then detected by PMTs. Since WIMPs distributed throughout the local neighbourhood are assumed to have non-relativistic speeds, the energy imparted to a recoiling nucleus is given by:

$$E_R = \frac{\mu_N^2 v^2 (1 - cos\theta)}{m_N} , \tag{2.13}$$

where $v$ is the velocity of the WIMP relative to the nucleus, $\theta$ is the scattering angle in the centre of mass frame, and $m_N$ is the mass of the recoiling nucleus [24]. DEAP-3600 is designed for a target threshold (minimum detectable energy) of 20 keVee (kiloelectronVolt electron equivalent). These units are used to distinguish between the amount of energy converted to scintillation light from electromagnetic events versus nuclear recoils. Equation 2.14 shows the relationship between energy converted into scintillation photons by a particle through electronics recoils ($\mathrm{E}_{ee}$) and the amount of energy converted into scintillation light by a particle with the same energy, but through a nuclear recoil ($\mathrm{E}_{NR,scint}$):

$$\mathrm{E}_{NR,scint} = \mathrm{E}_{ee} \cdot \mathrm{Q} \tag{2.14}$$

where Q represents the quenching factor. The quenching factor for nuclear recoils in liquid argon is 0.25 for the energy range 10 keV $< \mathrm{E}_{ee} <$ 250 keV [45]. Thus, for a particle which would generate 80 keVee of energy worth of scintillation photons through electronic recoils, only 20 keV of energy will be converted into scintillation photons through a nuclear recoil. Due to this quenching effect, the DEAP-3600 threshold of 20 keVee implies a sensitivity to events depositing 20 keV of energy into scintillation photons from electronic recoils, and nuclear recoils events with 80 keVee of energy.

# Chapter 3

# DEAP-3600

This chapter provides a brief introduction to the DEAP-3600 dark matter detector, discussing the basic detector design, and the principle of Pulse Shape Discrimination (PSD) which is central to single phase detectors. The production of SPEs by PMTs will be discussed, and that will segue into the next section on the DEAP-3600 electronics system.

## 3.1 The DEAP-3600 Experiment

The DEAP-3600 (Dark matter Experiment with Argon and Pulse shape discrimination) detector is being constructed at the SNOlab underground facility near Sudbury, Ontario, Canada. SNOlab is located in an active Vale Corporation nickel mine $\sim$ 2072 meters below the surface which provides 6010 meters water equivalent of overhead shielding [46]. At these depths SNOlab experiments benefit from a significant reduction in cosmic ray flux, $< 0.23\ \mu/\text{m}^2/\text{day}$ [47], the primary source of the cosmogenic neutron background for rare event neutrino experiments and dark matter searches.

DEAP-3600 is a single phase detector incorporating 3600 kilograms of liquid argon as the target medium for expected dark matter interactions. A schematic cross section of DEAP-3600's primary components is shown in Figure 3.1. For

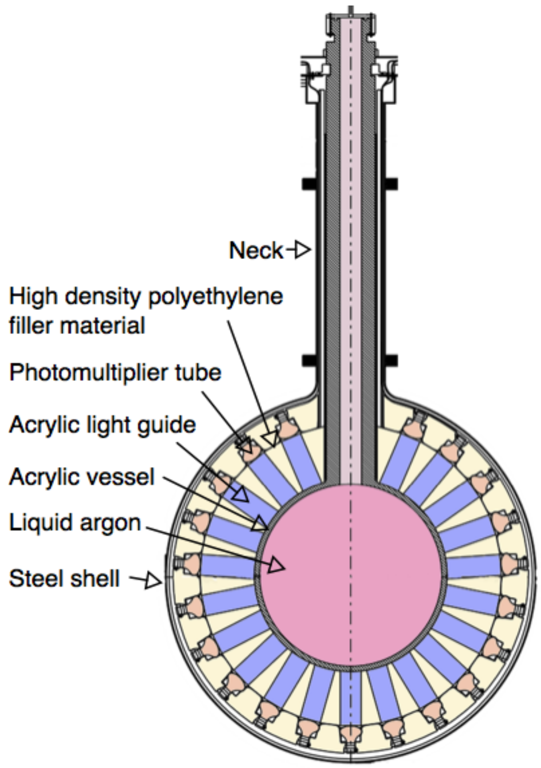


Figure 3.1: Cross section view showing major components of DEAP-3600 detector [48]. The acrylic sphere has an inner diameter $\approx 1.7$ m.

scale, the inner diameter of the acrylic vessel is 1.7 m, with the cylindrical light guides attached to the outside of the sphere measuring 50 cm in length.

The dominant background for the DEAP experiment is the signal from $^{39}$Ar $\beta$-decays and, assuming DEAP-3600 achieves its target energy threshold of 20 keVee, the detector must reject the $^{39}$Ar $\beta$-decays at a level of $10^{-10}$ to achieve a 3-tonne-year exposure without background events entering the region of interest [49]. Discrimination power is defined to be the ratio of mis-identified background events as nuclear recoils to the number of background events successfully rejected. A discrimination power of $10^{-10}$ means an experiment can correctly identify and reject 10 billion background events with less than one leakage into the signal region of interest. It is expected that DEAP-3600 will have less than 0.2 background $^{39}$Ar $\beta$-decays in the WIMP region of interest in a three year run [49].

### 3.1.1 Detector Design Basics

Acrylic is chosen as the primary detector material since it can be manufactured with high radio-purity, thus reducing the potential for background events produced close to the fiducial volume. The acrylic used for DEAP-3600 also has high optical transmission for the wavelength of light emitted by the wavelength shifter tetraphenyl butadiene (TPB) that will coat the inner acrylic vessel surface. A long neck attached to the top of the acrylic vessel provides a path for the argon recirculation. Attached to the outer surface of the acrylic vessel will be 255 cylindrical acrylic light guides, each weighing $\sim 17$ kg. The acrylic light guides serve two main purposes: first, they create a thermal gradient which separates the PMTs from the cryogenic temperature of the LAr; second, they act as neutron shielding for ($\alpha$,n) reactions generated by the PMT glass which contain naturally occurring concentrations of uranium and thorium [50]. The space between the light guides is also filled with layers of Styrofoam and acrylic for additional neutron shielding.

When 128 nm UV photons produced from argon scintillation are emitted, they propagate within the noble liquid until they reach the inner acrylic surface of the DEAP-3600 vessel. At the inner surface, which is coated with TPB, the photon is absorbed and re-emitted isotropically with a spectrum peaked at 440 nm [51]. The $\lambda$-shifted photons are then detected by DEAP's 255 Hamamatsu R5912 high quantum efficiency (HQE) PMTs attached to the end of the acrylic light guides, and the signals are transferred to the electronics system for processing.

For a WIMP event transferring 80 keVee of energy ($E_{ee}$) to an argon nucleus situated in the centre of the acrylic vessel, roughly 800 UV photons will be isotropically emitted (Equation 2.14 multiplied by light yield, Y). In the worst case scenario (only 1.0 $\mu m$ thick layer of TPB) there will be a one-to-one conversion of 128 nm photons to 440 nm photons ($\kappa = 1.0$), although this is a conservative (under-estimated) value. These blue photons are isotropically re-emitted, and are able to travel relatively freely through the acrylic light guides (attenuation length > 4.0 m) to the PMTs. Accounting for PMT photocoverage (S = 0.75) and average quantum efficiency (QE ≈ 0.32 at 440 nm), the total photoelectrons ($PE_{total}$) collected for the 80 keV recoil energy event is:

$$PE_{total} = E_{ee} \cdot Q \cdot Y \cdot S \cdot \kappa \cdot QE = 192 \, , \tag{3.1}$$

where Q = 0.25 (quenching factor), and Y = 40 UV photons per keVee (see Section 2.3.4). This implies that for a central event, the DEAP-3600 detector will collect $PE_{total} \sim 200$ PE with its 255 PMTs (less than 1 PE per PMT on average), which emphasises the need for an electronics system that maximises the SPE detection efficiency.

The acrylic vessel and surrounding neutron shielding structure will be encased in a steel shell immersed in a tank of ultra-pure water, 7 m in diameter, and 7 m tall (see Figure 3.2). The water serves as further mitigation of cosmogenic neutrons created by cosmic ray muons interacting with the surrounding cavern walls. The water shield will be viewed with veto PMTs to detect cosmic ray muons passing through the water, allowing rejection of events coincident with spallation products of cosmic ray muons interacting with the detector materials. These layers of radioactive shielding are increasingly radio-pure as one moves inwards toward the fiducial volume.

Table 3.1: Background budget (requirements) for DEAP-3600 during a three year run time [52].

| Background | # Events in Energy ROI | # Events in Fiducial ROI |
|---|---|---|
| $^{39}$Ar $\beta$s | $1.6\times10^9$ | $< 0.2$ |
| Neutrons | 30 | $< 0.2$ |
| Surface Events ($\alpha$) | 150 | $< 0.2$ |

The background requirements for DEAP-3600 during a three year run are shown in Table 3.1. Total background event leakage into the fiducial volume region of interest (ROI) should be less than 1 in three years. The $^{39}$Ar $\beta$s will

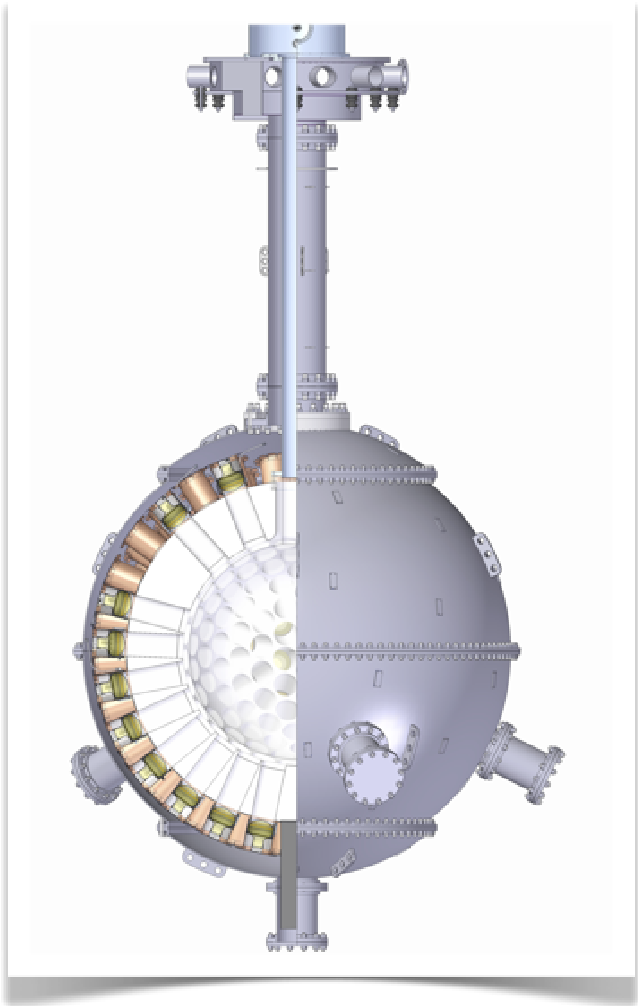

Figure 3.2: Schematic of the DEAP-3600 detector and steel containment shell [48].

be mitigated with energy and $F_{prompt}$ cuts (see Section 3.1.2), and the neutrons will be moderated with passive shielding (acrylic, water, and LAr). Remaining surface events from alpha backgrounds will be tagged with energy and radial cuts.

### 3.1.2 Pulse Shape Discrimination

When particles interact with argon it can be excited into either the short lived singlet, or longer lived triplet state. Electromagnetic backgrounds have a low linear energy transfer (LET) in the argon, and as a result the triplet state is predominantly excited. Note that linear energy transfer is the energy dissipated per unit of path length, dE/dx [53]. This triplet state excitation results in argon decaying to scintillation photons with a time constant of 1.6 $\mu s$. When a nuclear recoil occurs, the result is a high LET that predominantly excites the singlet state. With a time constant of 6 ns for the singlet state, most of the scintillation light from nuclear recoils ($\sim 75\%$) is produced in the first hundred nanoseconds of the interaction, as shown in the top of Figure 3.3.

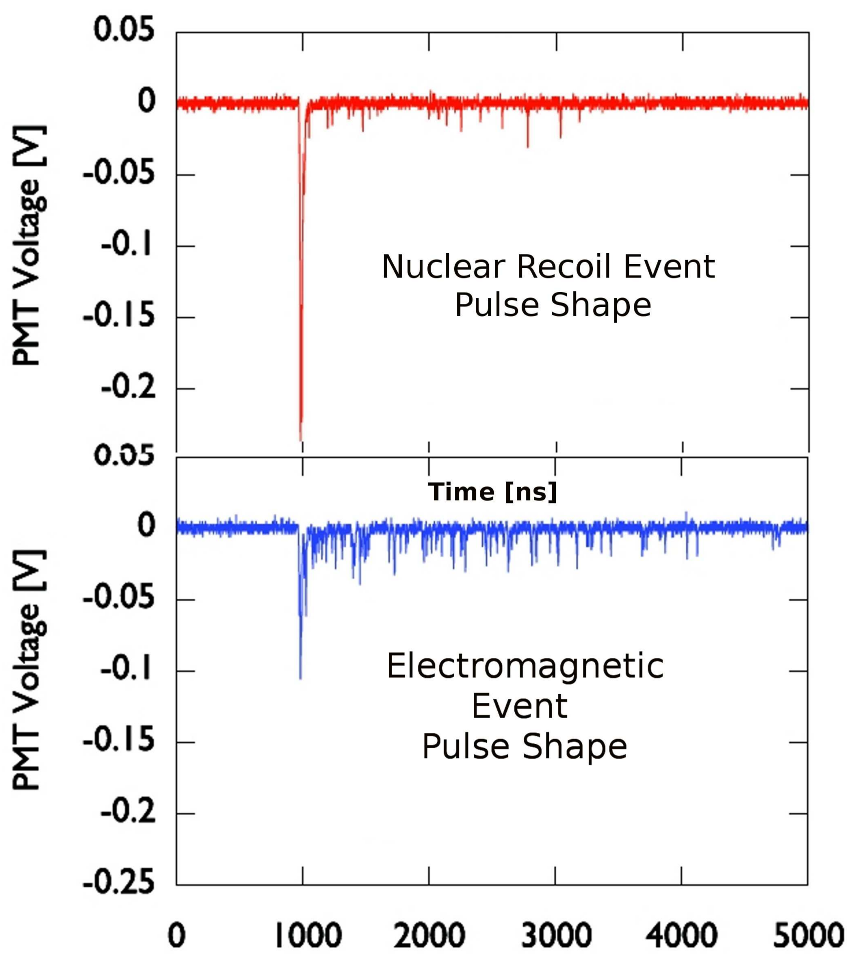


Figure 3.3: Pulse shape (total PMT voltage $\propto$ detected scintillation light vs time) for nuclear recoils (top, red) and electromagnetic backgrounds (bottom, blue) [54].

For electromagnetic events in argon like $^{39}$Ar $\beta$s, the triplet state is excited three times as frequently as the singlet state. Due to the longer triplet time constant (1.6 $\mu s$), only $\sim$ 25% of the light occurs within the prompt window (0 - 9 $\mu s$, see the bottom of Figure 3.3). The general trend for particle interactions in argon is that an increase in the LET of the event increases the total percentage of scintillation light due to the singlet state [53]. The difference in these two pulse shapes may be applied to a discrimination between nuclear recoils and electromagnetic backgrounds.

In Figure 3.3, the collected light has been converted to electrical pulses by the PMT, such that the amount of detected light is represented by the total voltage above baseline over time. Every photoelectron produced by the PMT creates a voltage which is added to a waveform like the one in Figure 3.3. DEAP-3600 characterises pulse shape differences with the parameter $F_{prompt}$, which is the ratio of early to total light, where the prompt light window is usually chosen as the first 150 ns of the event:

$$F_{prompt} = \frac{\int_{t_a}^{t_b} V dt}{\int_{t_a}^{t_c} V dt} \ . \tag{3.2}$$

Here $t_a$ is the start of the event, $t_b$ is the end of the prompt window ($\sim$ 150 ns), $t_c$ is the total event length ($\sim$ 9 $\mu s$), and V is the voltage recorded by the PMTs. The $F_{prompt}$ distributions of signal and background events can be shifted by modifying the prompt window size, but on average nuclear recoil events have a mean value of $\sim$ 0.75, while electromagnetic events, such as $^{39}$Ar $\beta$-decays, have a mean $F_{prompt}$ of $\sim$ 0.30. Plotting the $F_{prompt}$ of the event versus its total energy demonstrates that the nuclear recoils can be distinguished from the electromagnetic backgrounds (see Figure 3.4).

The total energy of the event is obtained from the following equation:

$$E_{total} = \text{QPE} \cdot k \tag{3.3}$$

where QPE is the number of detected single photoelectrons, and $k$ is the average

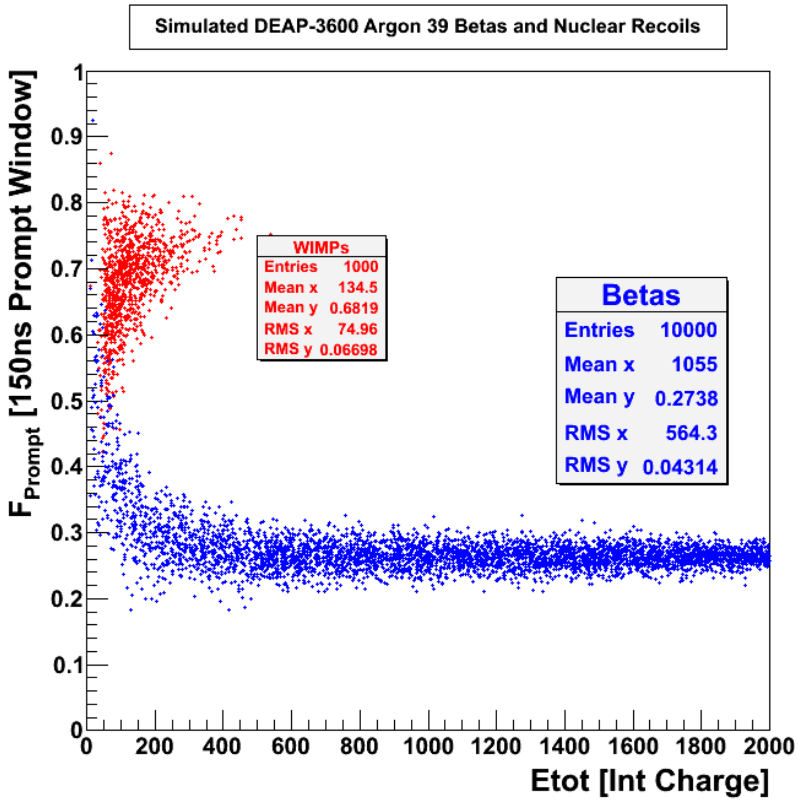


Figure 3.4: $F_{prompt}$ vs energy measured in integrated charge, which is proportional to collected scintillation light, for simulated electromagnetic and nuclear recoil events in DEAP-3600.

energy deposited to produce a single photoelectron. Above a certain energy threshold, the two distributions are well separated. The region of interest for WIMP interactions is obtained by defining a cut region where the probability of electromagnetic background leakage into the ROI is statistically limited. The precise region of interest will be determined once the calibration of DEAP-3600 has been performed, and the light yield has been characterised.

## 3.2 DEAP-3600 Electronics Overview

DEAP-3600 will detect particle interactions in argon using light detecting instruments known as photomultiplier tubes (PMTs). Photomultiplier tubes generate an initial electron via the photoelectric effect when a photon strikes the photocathode (see Figure 3.5). High voltage between the photocathode and

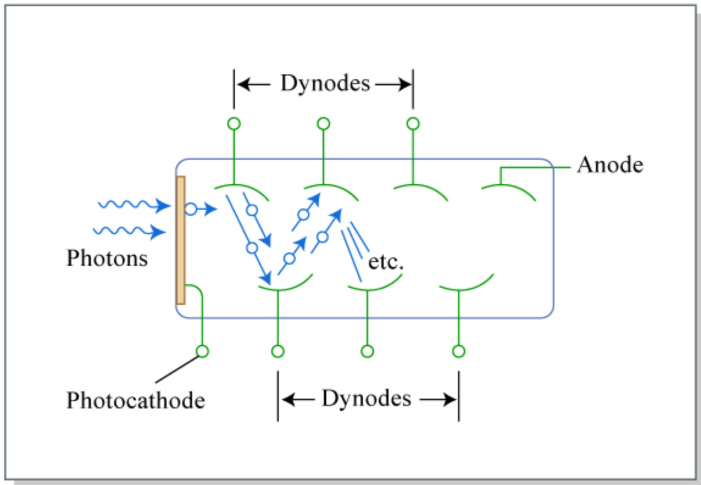


Figure 3.5: Schematic of the dynode structure used by a PMT for charge amplification [55].

first dynode accelerates the electron, until it strikes the first dynode. The dynode then releases two or more electrons, which are accelerated to the second dynode where they each release multiple electrons, and so forth, until the charge has been amplified to the point where it can be easily read out by an electronic device. For the majority of events occurring within the fiducial volume of DEAP-3600, the light detected by the PMTs will generate single photoelectron pulses which vary in shape and height, due to small differences in amplification from one dynode to the next, as well as the statistical nature of the conversion of photons to electrons [56]. The number of secondary electrons that an initial electron creates upon contact with a dynode depends on the energy of the initial electron, implying the variance in initial electron energies also contributes to the distribution of pulse heights generated by a PMT. The PMT used for DEAP, a Hamamatsu R5912 HQE, has a peak quantum efficiency of $\approx 32\%$ near 420 nm [57, 58]. The quantum efficiency is maximised for the blue region of visible light, which is the wavelength of light predominantly generated by the wavelength shifter TPB coating the inside of the acrylic vessel.

In order to identify the particle interacting with the argon, the information about the light generated as a function of time must be recorded electronically and analysed offline. To cope with the expected 3.6 kHz of background events from $^{39}$Ar $\beta$-decays, a hardware trigger system is used to reduce the number of recorded events. The overall electronic framework for DEAP-3600 is shown in Figure 3.6.

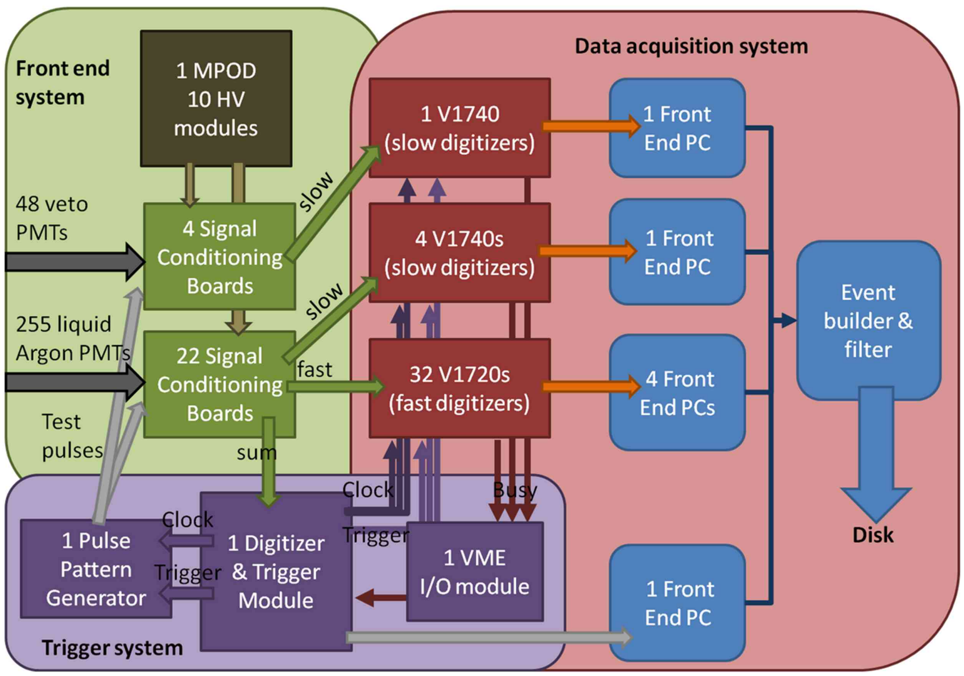


Figure 3.6: DEAP-3600 electronics data flow concept. The three sections represent the front end system, trigger system, and data acquisition system.

As shown in Figure 3.6, the first components to receive information from the PMTs are the signal conditioning boards (SCBs). The SCBs relay information to the trigger system which provides a threshold decision of interest in the event for recording. The information from the digitisers is sent to front end computers, where a second level of filtering is performed before the information is finally written to disk.

### 3.2.1 Analog Electronics

The following subsection will briefly describe how information from particle interactions propagate through the DEAP-3600 electronic infrastructure. This is to emphasise the importance of the SCBs for which the results of their testing is reported in Chapter 4. The electrical system discussion is divided into two parts: analog electronics, and digitiser electronics (readout). Further details of the operation of individual electrical components will be discussed after the overall purpose of each electrical component within the larger framework has been established.

Once a PMT converts the photons from a particle interaction into electrons, an electrical signal is generated and sent to the SCBs through a secure high voltage (SHV) cable. A single SHV cable for each PMT reduces the amount of material close to the liquid argon, saving on space used by the electronics system and reducing the potential for production of background events from the material in the cables. Each SCB has twelve PMT inputs, meaning there are a total of 22 SCBs for the 255 primary PMTs. Four additional SCBs receive the signals from the 48 muon veto PMTs. The SCB decouples the PMT signal from the PMT high voltage. An image of a signal conditioning board which was used for testing purposes is shown in Figure 3.7. Each SCB produces an analog sum of the twelve input PMT signals, and the sum from each of the 22 SCBs is sent to the Digitiser and Trigger Module (DTM). The sum is used to determine whether or not to pass the event information along the data processing chain by performing a fast estimation of the energy and $F_{prompt}$ of the event. The Digitiser and Trigger Module is being designed and developed at the TRIUMF National Laboratory in Vancouver, British Columbia. The goal of the DTM is to reduce the event rate by filtering 90% of the $^{39}$Ar $\beta$-decays. The event rate reduction by the DTM will ensure the digitisers are not overloaded at any point during operation, reducing the risk of potential detector dead time.

The SCB also outputs the PMT signals into two other channels to be sent

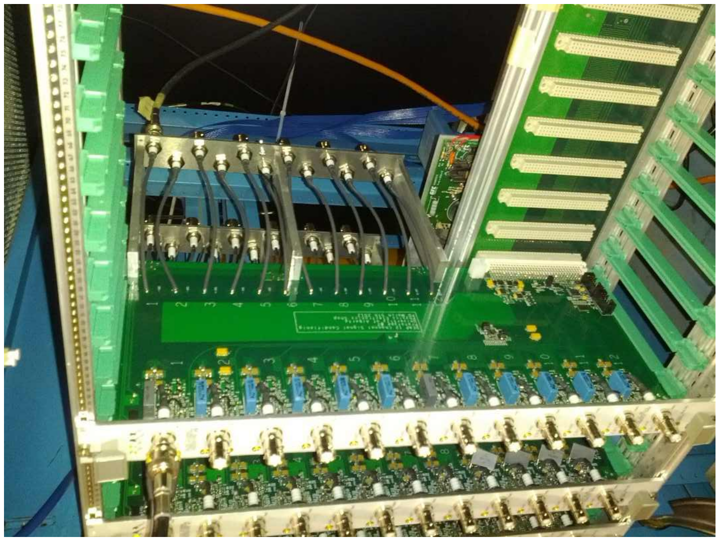

Figure 3.7: Signal Conditioning Boards in a crate, set up for performance testing at TRIUMF.

to the CAEN digitiser modules: high (HG) and low gain (LG). HG is a fast output channel with moderate pulse height amplification and pulse widening with a 4 to 8 ns time constant (selection of an appropriate time constant is discussed in Chapter 4). The HG channel on the SCB will be used to record information about high frequency and low light events, such as argon $\beta$-decays and nuclear recoils. The pulse widening is designed to maximise the signal to noise ratio (S2N) and alter the pulses so that their rise time can be recorded over a number of time bins by the digitiser. If the pulses are too narrow with respect to the sample size on the digitiser (4 ns), then information about the pulse shape will be lost due to the precision of the digitising device.

Higher energy events which may saturate the high gain channel (such as alpha decays on the surface of the acrylic vessel) are read out using the low gain channel. This reduces the overall dead time of the detector, and permits high energy background events to be studied. The low gain channel attenuates the PMT signal by a factor of approximately 10 relative to the high gain, and widens the single photoelectron (SPE) pulses to about 100 ns. Given that low gain channels are read out by slower digitisers (65 MegaSamples/second), the pulses must be relatively wide in order to retain the shape information. The properties of the SPE pulses which are tunable using the SCBs are:

- Pulse height (controlled by amplifiers on the SCB)
- Pulse rise and fall time (controlled be amplifier speed, capacitors)
- Integrated pulse charge (controlled by amplification and pulse widening)

These pulse properties are characterised during the SCB performance tests to ensure the optimal SPE detection efficiency can be achieved (see Chapter 4). Electronics noise for a number of integration windows was also characterised to ensure a maximum signal to noise ratio.

### 3.2.2 Digitiser Electronics (Readout)

After the SCB has processed the PMT signals, they are transferred to the Analog to Digital Converters (ADCs).

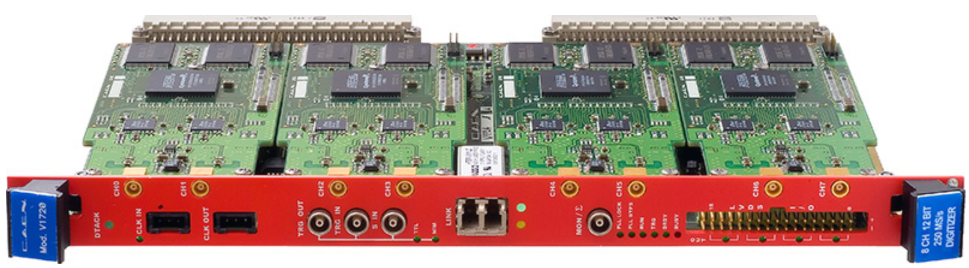

Figure 3.8: CAEN analog to digital converter model V1720. 32 fast ADCs will be used by DEAP-3600 to process information about low light, high frequency events. Image from CAEN website.

The function of the ADC is to convert the raw electrical signal (measured as a voltage) into a binary word [59]. DEAP-3600 uses CAEN V1720 12 bit ADCs (see Figure 3.8) for the fast output, which have a sampling rate of 250 MegaSamples/second [60]. The CAEN V1720 has 8 channels, meaning there are a total of 32 V1720 digitisers to receive the 255 PMT signals. The size of the bins on the time axis ($\Delta t$) of the digitised waveform is given by:

$$\Delta t = \frac{1}{R_s} = \frac{1}{250 \times 10^6 \text{ S/sec}} = 4 \text{ ns} \tag{3.4}$$

where $R_s$ is the sample rate of the digitiser. The resolution of a digitiser refers to the smallest change in input voltage it can theoretically measure, neglecting noise. A 12 bit digitiser, combined with a 2 Volt peak-to-peak dynamic range ($V_D$), gives a digitiser resolution ($R$) of [61]:

$$R = \frac{V_D}{2^n} = \frac{2000 \text{ mV}}{4096} = 0.488 \text{ mV} \tag{3.5}$$

where $n$ is the bit resolution of the ADC. With the above resolution, the ADC units recorded by the digitiser correspond to $\approx 0.5$ mV. The ADCs continually convert the analog electrical signal into a digital signal which is kept in a cyclical buffer until the digitiser is triggered to read out. The information in the buffer is then read and sent to a PCIe card, with a maximum transfer rate of 80 MB/s. The front end computer writes the data to disk using the Maximum Integration Data Acquisition System (MIDAS) software, which is a simple and flexible data acquisition (DAQ) system developed by researchers at the Paul Scherrer Institute in Switzerland, and TRIUMF National Laboratory in Canada [62]. When the DTM registers a high light event, such as an alpha decay on the surface of the DEAP-3600 detector, it will signal the digitisers to read out the low gain channel of the SCBs. The signals from the SCB low gain channels will be sent to the CAEN V1740 digitisers, where each slow digitiser (V1740) can accept up to 64 input channels. Four of the slow digitisers (256 channels) will be used for the LG channels of the SCBs, and a fifth V1740 will be used to accept the signals from the 48 muon veto PMTs.

# Chapter 4

# Signal Conditioning Board Performance Tests

## 4.1 SCB Chapter Overview

The Analysis Methodology section that follows is divided into a series of subsections. It explains the process behind the analysis which is performed in the following two sections (on SCBv2 and SCBv3). The first subsection of Analysis Methodology will describe the DEAP electronics testbed setup at the University of Alberta for the purpose of performance testing the SCBs. Next, the pulse finding algorithm DSPE is discussed to give the reader an idea of the process behind the average waveform and pulse height distribution production. The remainder of the Analysis Methodology section describes in detail the process behind all of the performance tests. Results may be found in the Performance Tests sections.

The SCBv2 section starts with a description of the board (with some design specifications), and then proceeds with the results of the performance tests. The results show the distributions which were obtained from the analysis outlined in the Analysis Methodology section, and discusses the implications of the results.

The SCBv3 Pre-Testing section explains how an updated version of the SCB was analysed to determine which channel, from a variety of channels with different characteristics, was selected for rigorous testing. The SCBv3 Channel 10 Performance Tests section then outlines the same analysis as outlined in the Analysis Methodology section to determine the overall performance of the selected channel and compare it with the results of the previous iteration of the board (SCBv2). Chapter 4 concludes with a short section on two auxiliary tests completed with SCBv3 to determine if design specifications with respect to dynamic range are met.

## 4.2 Analysis Methodology

The Analysis Methodology section of this thesis is meant to provide the reader with an in-depth understanding of how the results of the following sections are obtained. It may be useful to refer back to this section after reading the SCB Performance Tests sections. The various distributions and histograms explained in this section all have the common theme of providing some measure for the performance of the SCB being tested. Some parameters are not an absolute measure of the SCB performance by themselves, but aid in determining whether an improvement has been made by comparing with the same parameter measured with a different board. For example, the peak to valley ratio (Section 4.2.4) is just a dimensionless quantity, but an increase in peak to valley from one board to another can indicate that the changes made to the hardware have had a beneficial impact on the board's pulse height distribution shape.

### 4.2.1 Electronics Testbed

To facilitate the signal conditioning board performance tests, an electronics testbed was established. A dark box (light tight container) was constructed for the purpose of PMT testing, which is approximately 100 cm × 50 cm × 40 cm in size. A Bertran Model 375P High Voltage power supply was used to power the PMT. A schematic showing the main components of the electronics testbed is shown in Figure 4.1.

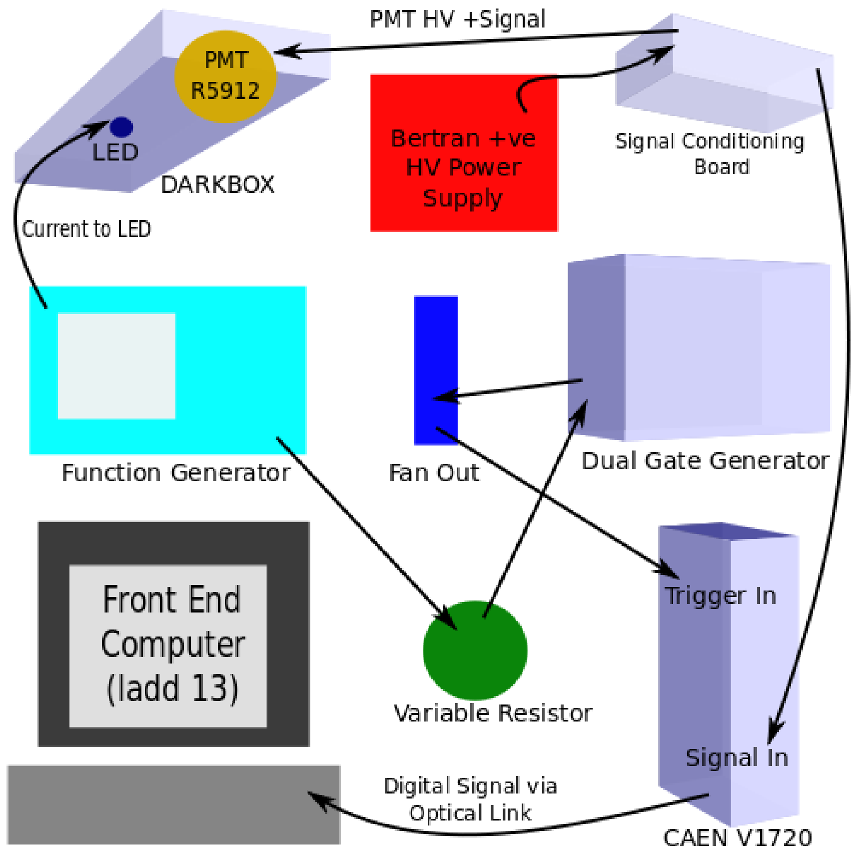


Figure 4.1: DEAP-3600 electronics testbed schematic.

The high voltage is separated (decoupled) from the PMT signal at a SCB, since both share a common cable. The SCB output is sent to a CAEN V1720 digitiser, and the signal from the digitiser is sent via optical link to the PCIe card on the front end computer. Photons are generated with a blue light emitting diode (LED) which is attached to a fibre optic cable. The LED and cable are placed inside the dark box facing the PMT. An arbitrary function generator (AFG) is used to generate voltage pulses which are converted into a trigger signal and sent to the digitiser. A copy of the AFG signal is sent to the LED to generate light. To ensure that most of the pulses generated by the LED contain on average a single photon, the signal from the AFG is set to be as narrow as possible (typically 30 ns wide). Approximately 80% of the pulses sent to LED do not generate photons, which ensures that the number of multiple photoelectrons generated by the PMT are statistically limited.

The front end computer receives the digitised waveforms from the V1720, and saves the information in a file format compatible with the DAQ software MIDAS. Raw waveforms are then processed through analysis algorithms developed by DEAP-3600 researchers to identify the event topology. All of the analysis performed in the following sections on SCB performance tests was facilitated with computer programs created by the author, which were derived from earlier code written by researchers at TRIUMF that served the primary purpose of interfacing with the MIDAS file storage.

### 4.2.2 DSPE: Digital Single Photoelectron Detection

One of the primary goals of the electronics testbed for DEAP-3600 is to measure the performance of the SCBs. Ultimately, the ability to distinguish a WIMP signal from electromagnetic background events with DEAP relies on the effectiveness of the electronics system to accurately record and process information from the particle interactions within the LAr. The digitised pulses from the electronics testbed follow the same signal conditioning pattern which will be implemented in the DEAP-3600 detector. This permits testing of pulse detection algorithms prior to detector installation and commissioning. To effectively separate signal from background, the waveforms recorded by the DAQ setup must provide an accurate measurement of $F_{prompt}$ and energy (recall Equations 3.2 and 3.3). This may be accomplished if the waveforms have a high signal to noise ratio (S2N = the ratio of pulse height to noise distribution width). A S2N of $\geq 30$ is required for DEAP-3600 in order to maximise the SPE detection efficiency. For S2N less than 30, SPE detection becomes prone to leakage from noise pulses, which are comparable in size to smaller SPE pulses. This leakage from noise pulses at low S2N values reduces the precision of the reconstructed $F_{prompt}$ and energy.

Digital/Derivative Single Photoelectron detection (DSPE) is the name given to one of the leading algorithms used to detect SPEs in DEAP-3600 waveforms. The algorithm must be highly efficient in identifying SPEs to provide the most accurate value for the total charge of the particle interaction. The algorithm determines the change in voltage from one time bin to another by moving through the waveform and subtracting the previous bin contents from that of the current bin. This algorithm utilises the fact that SPE pulses generated by the PMT rise faster than pulses generated by random electronics noise. It then sets a threshold on this "derivative" histogram. The threshold for the derivative histogram is usually set to:

$$T_{DSPE} = 5 \cdot \sigma_{4ns} \tag{4.1}$$

where $\sigma_{4ns}$ is the standard deviation of the single time bin noise distribution (recall that the digitised waveforms have a bin size of 4 ns). This threshold was chosen because it reduces the leakage from noise pulses to the $10^{-4}$ level (less than one leaked noise pulse per $10^4$ PMT-generated pulses), which helps to statistically limit the effect of noise pulses on the average waveform calculation. The start of a recorded pulse ($T_{start}$) is defined at the point where the derivative threshold is first crossed. Once the derivative returns to zero, the end of the pulse ($T_{stop}$) is assigned. While a waveform is processed with the DSPE algorithm, the total charge (sumQ) is calculated by integrating the signal over time. To determine the peak pulse height the maximum voltage is subtracted from a baseline, set by the digitiser for the zero pulse region. Figure 4.2 shows an example of a digitised SPE pulse.

For a typical background event occurring at the centre of the DEAP-3600 detector (such as a 100 keV $\beta$-decay), each PMT is expected to receive a

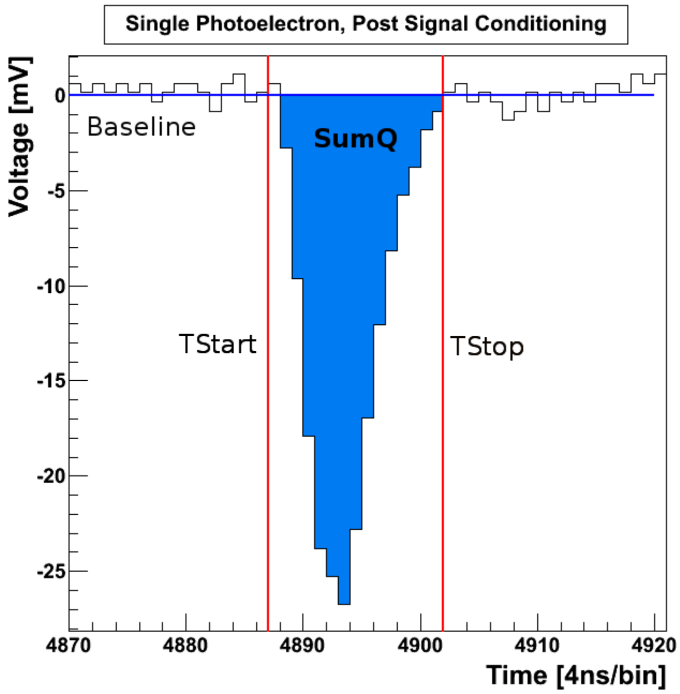


Figure 4.2: Pulse found by DSPE with integrated charge shaded in blue, blue line showing the baseline, and the red lines showing the calculated start and stop time of the pulse.

few well separated photoelectrons, with minimal pileup. The SPE detection efficiency is therefore crucial for a proper event energy measurement. This requirement is the reason why signal conditioning is performed: to maximise SPE detection efficiency, as well as signal to noise ratio. SPE counting is crucial for dark matter experiments where pulse shape discrimination is the primary background rejection technique. This is contrasted with other particle detectors such as those housed in accelerator laboratories, where the signal is composed of many events in a short period of time, or where the signal is high energy and generates many photons in a short period of time.

### 4.2.3 Pulse Height Distributions

High voltage power supplies are connected to the SCBs with single SHV cables. The SHV output of the SCB is then connected to the PMT base, which distributes the voltage to the dynodes in the PMT. Since the SCB and PMT base have different total impedances, the high voltage reaching the PMT is not equal to the high voltage applied to the SCB. To determine the HV applied to the PMT base for a given HV applied to the SCB, the following equation may be used:

$$V_{base} = V_{SCB} \cdot \frac{R_{base}}{R_{base} + R_{SCB}} \ , \tag{4.2}$$

where $R_{base}$ is the impedance of the base (22.5 MΩ) and $R_{SCB}$ is the impedance of the SCB (1.5 MΩ). This means that roughly 94% of the HV that is applied to the SCB is applied to the PMT base.

The optimal PMT voltage depends on the application of the detector, as well as dynamic range requirements (the maximum number of PEs an electronics system must be able to detect in a short time window without saturating). For the DEAP-3600 detector, the optimal voltage is defined as the supply voltage where the signal to noise ratio is large enough to adequately distinguish SPEs from noise and the average pulse heights avoid saturating the digitiser when multiple SPEs occur within a time window of 40 ns (the average length of a pulse). The voltage should be high enough to meet the signal to noise requirements, but below the maximum operating voltage to ensure longevity of the PMT, and to minimise the dark pulse rate that would otherwise affect the measurements of energy and $F_{prompt}$ for particle interactions in DEAP-3600. Dark noise is discussed further in Section 4.2.7.

Choosing a PMT operating voltage below the maximum PMT voltage is also beneficial because of the smaller width of the pulse height distribution at lower voltages. A narrow pulse height distribution will enhance the calculation accuracy of the number of photoelectrons per event in DEAP-3600, increasing the precision of both the $F_{prompt}$ and energy calculations, and therefore optimising the detector discrimination power.

By increasing the PMT voltage, one increases the gain of the PMT, or charge amplification of the final output pulse. The gain of the PMT is also a function of the number of dynodes. A plot of the gain versus PMT HV (R5912 model) is shown in Figure 4.3. The lower gain model of PMT (R5912) has fewer dynodes (10) than the R5912-02 (14), which results in a lower slope of the gain vs supply voltage curve.

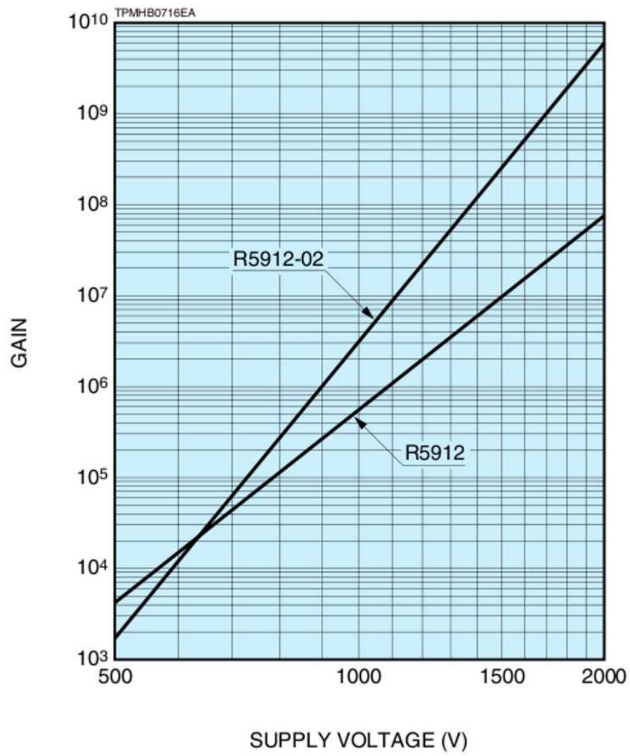


Figure 4.3: PMT gain versus high voltage. The PMT used for this analysis is an R5912, so the less steep line represents its gain vs high voltage relationship [58].

To determine the behaviour of the PMT and SCB for increasing HV, the supply voltage to the PMT is increased in increments of 100 V and the corresponding pulse height distribution is evaluated. Pulse height distributions are generated with the electronics testbed in SPE mode, meaning the LED is pulsed in such a way that around 20% of the LED voltage pulses generate an SPE in the PMT. SPE mode ensures that the electronics testbed produces a statistically limited number of multiple photoelectron pulses. The digitiser is triggered on a modified version of the voltage pulse that is sent to the LED such that most SPEs found in the digitised waveforms are the result of LED generated photons, with dark noise SPEs in the waveforms being suppressed to the level of roughly one dark SPE per 20 digitised waveforms.

Digitised waveforms are recorded and scanned for the largest pulse height beyond the baseline. For waveforms containing a SPE pulse, the SPE pulse height is added to the distribution while waveforms containing pure noise contribute a maximum noise value. This results in two peaks: a noise peak centred around a few mV, and an SPE pulse height distribution centred at the most probable pulse height. A plot of a sample pulse height distribution is shown in Figure 4.4. Locations of peak and valley are labelled for clarity, and the peak to valley ratio is discussed in the next section.

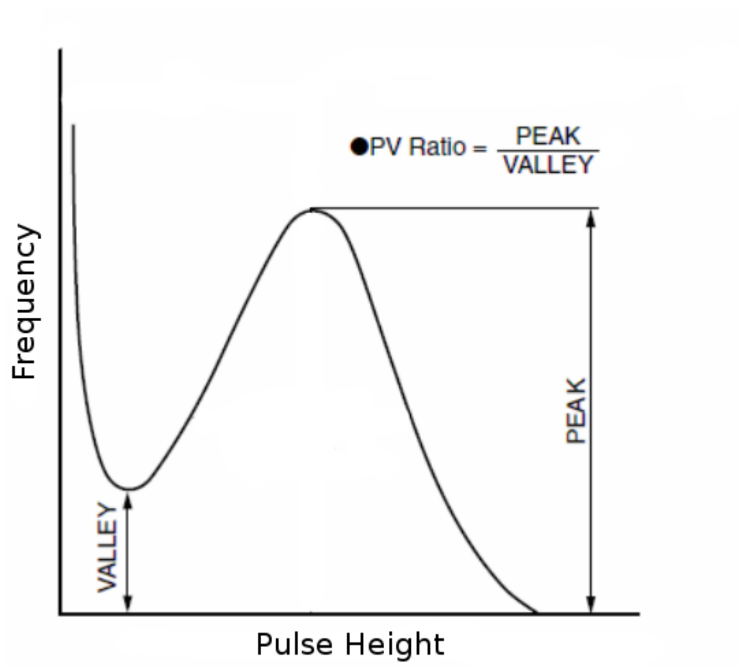


Figure 4.4: Example of a PMT pulse height distribution for SPE mode. Figure adapted from [63].

### 4.2.4 Peak to valley ratios

To determine the peak to valley ratio for each distribution a $6^{th}$ order polynomial function is fit to the region containing the peak of the SPE distribution and the valley in between the noise peak and SPE peak. The fit is performed strictly to find a reasonable agreement with the data in order to determine the peak to valley ratio, and is not intended to represent any underlying physics contributing to the curve. After the maximum (peak) of the SPE distribution and minimum (valley) of the inter-peak region is identified, they are divided to obtain a peak to valley ratio. The peak to valley (P2V) ratio is a relative indicator of SCB performance where a large P2V indicates the size of the SPE peak is large with respect to the leakage from noise pulses, implying less noise will leak into the SPE spectrum and bias the data. If the P2V ratio increases from one board to another without changing PMT voltage, then the second board has either superior amplification, reduced noise, or both.

### 4.2.5 Average SPE Waveforms

Average pulse shape waveforms are generated to determine the average SPE pulse height used to calculate a signal to noise ratio. Once SPE pulses are identified in the digitised waveforms using the DSPE algorithm, average waveform histograms are produced by aligning the individual pulses so that all leading edges ($T_{start}$) begin at the same time. Average waveforms are typically left in the voltage units which are produced by the digitiser (based on its resolution). These units, which are referred to in this thesis as "ADC units" can be converted to mV by multiplying by 0.488 mV/ADC (see Equation 3.5). "ADC units" are the smallest division of charge which a particular digitiser can output, and in the case of the CAEN V1720 this corresponds to $\approx 0.5$ mV. The average height of the SPE waveform depends both on the applied PMT voltage and the number of small noise pulses that leak into the SPE spectrum. The effect of the noise pulses may be mitigated by increasing the derivative threshold used for DSPE. DEAP-3600 strives for an average SPE pulse height of about 20-30 mV from the HG channel. This pulse height is considered the ideal trade-off: it increases the signal to noise which enhances SPE detection, but it is also low enough to keep the dynamic range of the digitiser around 100 PEs for the HG channel. The digitiser has a dynamic range of 2.0 Vpp (Volts peak-to-peak), so an average pulse height of 20 mV means that 100 PE could pile-up in a short time window and still be recorded from the HG channel (without saturation of the V1720). This 100 PE dynamic range is necessary to maintain an accurate event energy reconstruction for particle interactions at larger detector radii which may have $\sim$ 10 - 100 scintillation photons arrive at individual PMTs.

### 4.2.6 SumQ (Integrated Charge) Distributions

SumQ refers to the integrated charge of each pulse, or equivalently the amount of charge contained in the pulse for the duration of its occurrence. The integrated charge of each pulse is a function of both the pulse height and the pulse width. SumQ is also related to the gain of the amplifier on board the SCB and the gain imparted by the PMT. It is thus directly affected by the PMT supply voltage. A sumQ distribution having a narrow width is desirable since it represents a minimal statistical variation of pulse sizes, which permits increased accuracy when counting multiple PE pulses. A large mean value for the sumQ distribution is also beneficial since an increase in the integrated charge per pulse results in greater discrimination of the SPE pulses from background electronic noise pulses.

After plotting the sumQ distribution for SPEs (in units of V·ns), the area between the noise peak and SPE peak is fit with a $9^{th}$ order polynomial. This polynomial fit is not meant to represent any underlying physics contributing to the histogram, it is only meant to obtain an analytic representation of the curve, which provides an accurate determination of the maximum value of the SPE peak.

### 4.2.7 Sources of Noise

There are many types of electronics noise, but only a few are relevant to the analysis presented in this thesis. "Dark counts" are a type of noise where pulses are generated by thermionic emissions from the photocathode or dynodes which do not have a photon progenitor [64]. The number of dark counts per second is referred to as the dark rate, and it is affected by the PMT HV, PMT temperature, cathode material, and photocathode area [65]. The dark rate is a background level for photoelectrons that is removed from energy measurements via calibrations.

A second type of noise known as "Johnson noise" is a voltage generated by any resistor [66]. The amplitudes of Johnson noise follow a Gaussian distribution, which is the rationale for certain noise distributions in this thesis being fit with Gaussian functions. "Flicker noise" is another electronics base noise that comes from slight variances in the actual resistance of a resistor. The amount of flicker noise depends on the type of material used for the resistor, but the RMS of the noise distribution is typically on the order of fractions of $\mu V$ [66].

One final kind of noise which will be discussed is transient signal interference, referred to as "pick-up" noise. Pick-up noise can come from many sources, including 60 Hz interference from power supplies, radio station signals, or computer monitors nearby the electrical equipment. These noise sources can be mitigated with a variety of techniques such as band-pass filtering, magnetic shielding, or equipment relocation.

### 4.2.8 Noise Distributions

To generate 4 ns noise distributions, digitised waveforms for $\sim$ 50000 events were recorded and the contents of an arbitrarily chosen "noise bin" in every waveform were histogrammed once the calculated baseline was subtracted. In order for the SPE detection to remain reasonably efficient (say above 95% for accurate particle identification), the standard deviation of the 4 ns integration time noise distribution should be less than 0.025 PE. The noise level, in photoelectrons, for the 4 ns window is given by:

$$N_{4ns,PE} = \frac{\sigma_{4ns}}{V_{SPE,ADC}} \tag{4.3}$$

where $\sigma_{4ns}$ is the standard deviation of the noise distribution and $V_{SPE,ADC}$ is the average pulse height of a single PE.

During the trigger operation of DEAP-3600, the $F_{prompt}$ of an event is estimated using a method that digitises and sums 255 waveforms (from the 22 SCBs analog sums of the 12 channels on each board), integrates the pulses, and then divides by the average charge in a SPE. The feasibility of this method requires the noise in a 200 ns window to be less than 0.050 PE. To determine the $\sigma$ of the 4 ns noise distribution in PE, the single bin noise values are plotted in a histogram and fit with a Gaussian. For the 200 ns window, 50 consecutive bins from a randomly chosen location in the digitised waveforms are summed (after subtracting the baseline), and the resulting 200 ns noise histogram (produced from the 50000 waveforms) is fit with a Gaussian. The standard deviation of the Gaussian fit in photoelectrons (PE) is converted from raw ADC values by dividing by the average pulse height of an SPE for a 4 ns time window (Equation 4.3), or by the average sumQ of an SPE for a 200 ns window (Equation 4.4):

$$N_{200ns,PE} = \frac{\sigma_{200ns}}{SumQ_{SPE,ADC}} \tag{4.4}$$

Here $N_{200ns,PE}$ is the noise level in PE for the 200 ns time window, and $\sigma_{200ns}$ is the standard deviation of the 200 ns noise distribution.

### 4.2.9 Signal to Noise Ratio

The signal to noise ratio (S2N) is defined to be:

$$\text{S2N} = \frac{V_{SPE}}{\sigma_{4ns}} \tag{4.5}$$

where $V_{SPE}$ is the average pulse height of a single photoelectron and $\sigma_{4ns}$ is the standard deviation of the electronics noise distribution for the 4 ns time bins. DEAP-3600 strives to achieve a S2N exceeding 30, in order to facilitate optimal SPE detection. S2N may also be used to compare the performance of one electrical component to another, permitting a comparison of the overall performance of SCBs.

## 4.3 Version 2 of the Signal Conditioning Board: Performance Tests

### 4.3.1 SCBv2 Design and Specifications

The first signal conditioning board operated with the setup described in the electronics testbed section is referred to as Version 2 (SCBv2). This board is populated with a HG channel having a narrow pulse width (4 ns time constant), and a 4.7 nF coupling capacitor. The amplifier used on SCBv2 is the AD8005: a high speed (270 MHz) and low power (4 mW) amplifier selected for its low noise properties. The SCBv2 results in this section represent a benchmark to which future versions of the boards can be compared when evaluated with the electronics testbed.

### 4.3.2 SCBv2 Pulse Height Distributions

The pulse height distribution for the SCBv2 is shown in Figure 4.5. The peak from the noise pulses is evident at the left of the distribution near zero, with a distinct SPE pulse peak located to the right of the noise peak.

Figure 4.5 shows the general trend of increasing average pulse height for

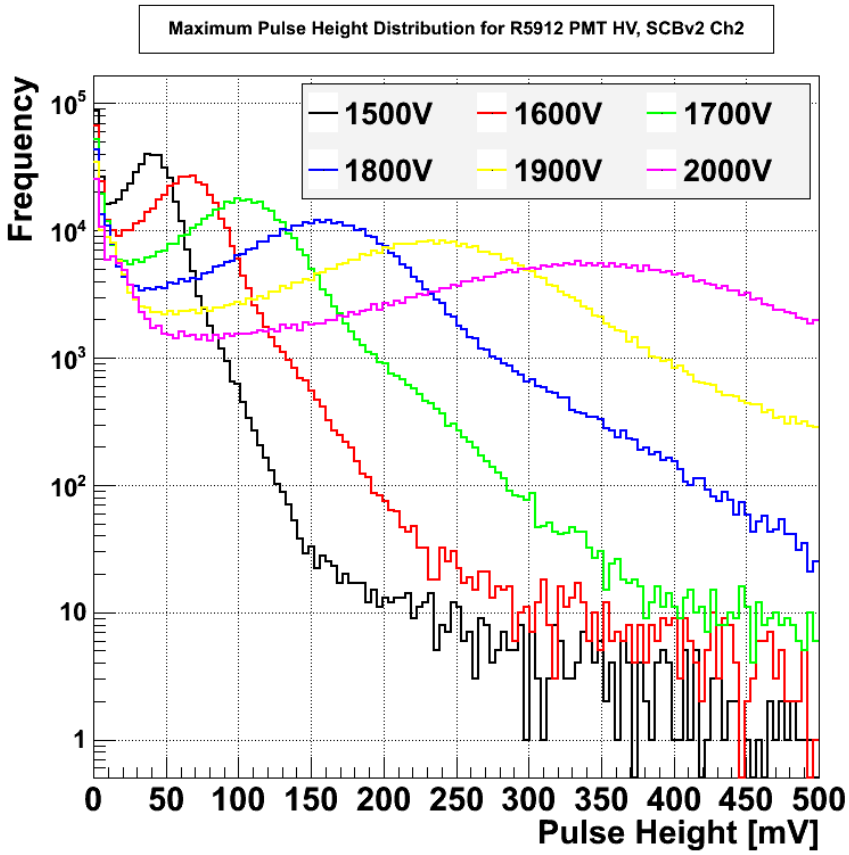


Figure 4.5: Pulse height distribution for various PMT supply voltages using the SCBv2.

increasing PMT high voltage, as well as a widening of the SPE pulse height distribution (PHD) for increasing high voltage. The endpoint of the measurement at 2000 V on the PMT represents the maximum operating voltage of the PMT, at which point the gain should be about $5 \times 10^7$. The PHD for the SCBv2 indicates the PMT is operating normally, with a predictable change in the pulse height for varying PMT voltage (discussed in the next section).

### 4.3.3 The SCBv2 Peak to Valley Ratio

The peak to valley (P2V) is the ratio of the tallness of the SPE pulse height distribution to the height of the valley between the SPE pulse height distribution and noise peak (recall Figure 4.4). This ratio is an indication of the separation of the noise and SPE signal in the pulse height distribution. A larger P2V is preferred, as it indicates the noise is more readily distinguishable from SPE pulses. P2V can be used to compare the performance of one board to another, when operated within the same testbed. For more information on how P2V is calculated, refer to Section 4.2.4. The measured peak to valley ratio vs PMT HV for the setup with the SCBv2 is shown on the left of Figure 4.6, and the data points are interpolated with a cubic spline. The peak to valley ratio increases with PMT high voltage, and begins to turn over near the maximum operating voltage. If one recalls the earlier discussion on SPE pulse height distributions, the P2V result indicates that an optimal pulse height (for S2N and dynamic range) can be obtained by tuning the PMT supply HV, without sacrificing the P2V ratio at higher voltages. The Hamamatsu corporation states the average peak to valley ratio for the R5912 is 2.5 [58], and all experimental P2V ratios were above this value. This experimental increase in P2V may be a result of the pulse height amplification introduced by the SCB.

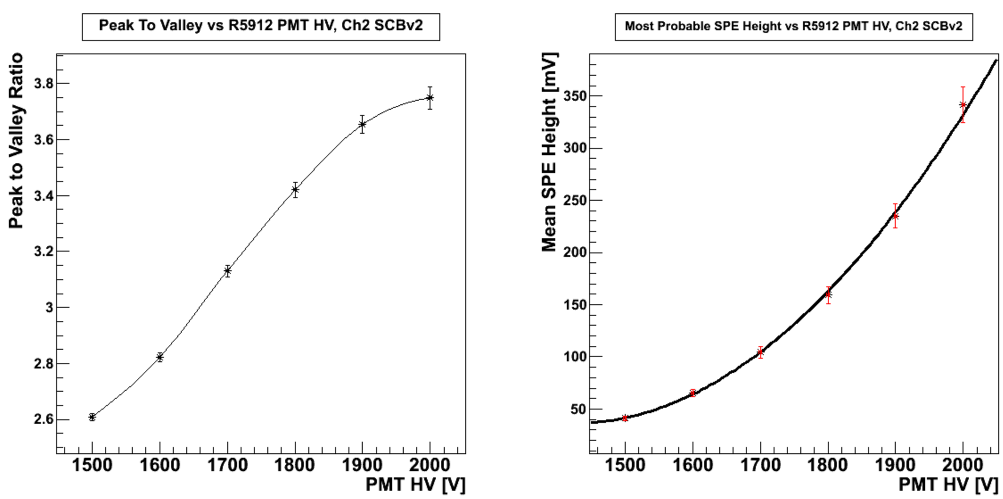


Figure 4.6: SCBv2 peak to valley ratio versus PMT HV (left), and most probable SPE pulse height versus PMT HV (right), fit with a second order polynomial.

The right hand plot in Figure 4.6 shows the peak of the SPE pulse height distribution plotted versus PMT HV. The curve is fit with a second order polynomial, indicating the most probable SPE pulse height increase with voltage increase is fairly easy to characterise. Thus one may diagnose potential unanticipated PMT voltage changes by monitoring SPE pulse heights, which is important for the study of the long term reliability of the PMTs. Any potential change in PMT gain with time could impact the detector energy efficiency, and thus needs to be monitored and accounted for during the detector's operation.

### 4.3.4 The SCBv2 Average SPE Waveforms

The SCBv2 average SPE waveforms are generated by applying 1500 V to the PMT base (1600 V to the SCBv2, as indicated by Equation 4.2). This voltage was chosen to give a reasonable average SPE pulse height, thereby minimising the pulse height distribution width and dark count rate.

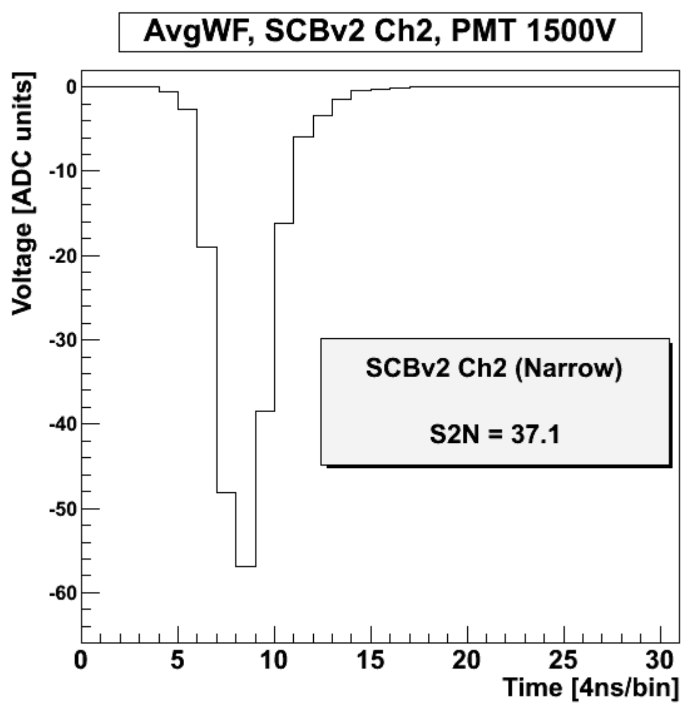


Figure 4.7: Average waveform for an SPE with the PMT at 1500 V, conditioned by the SCBv2, with an average pulse height 27.81 ± 0.05 mV.

Figure 4.7 shows the average waveform for SCBv2 Channel 2 with a pulse height of 56.95 ± 0.11 ADC units (or 27.81 ± 0.05 mV). The fall time (drop from baseline) is $\sim$ 16 ns, compared to a rise time (return to baseline) of $\sim$ 20 ns. No overshoot (voltage above baseline upon return from a pulse) is observed, but a small anomaly is seen near time bin 30 that is potentially due to a cable reflection, or after-pulsing. This is not expected to affect the overall pulse shape discrimination, due to both its small relative size and separation from the stop time of the pulse. We note that the average SPE pulse height is not equal to the most probable SPE pulse height (value corresponding to peak of SPE distribution). However, due to the asymmetric nature of the pulse height distribution, the *average* pulse height is a value lower than the most probable pulse height. As a result, the average waveform pulse height 56.95 $\pm$ 0.11 raw ADC units is lower than the most probable SPE pulse height, 81.90 $\pm$ 0.09 raw ADC units.

### 4.3.5 SCBv2 SumQ Distributions

An example of a sumQ distribution for the R5912 PMT with a supply voltage of 1500 V is shown in Figure 4.8. To produce this figure, the LED is pulsed in such a way that $\sim$ 20% of the digitised waveforms contain an SPE. The distribution is shown to have a shoulder on the side closest to the noise peak from pulses which obtained less charge than average, possibly originating from electrons being thermionically emitted from the first dynode, and therefore missing a stage in the amplification chain. The blue line in Figure 4.8 shows the $9^{th}$ order polynomial fit applied to the region of the SPE peak and a portion of the noise dominated region. From the fit result the location of the peak of the SPE distribution is found to be -0.419 $\pm$ 0.001 V·ns, or equivalently in units of ADC·4ns: $\mu_{SPE}$= 215 $\pm$1 ADC·4ns. The most probable value of the sumQ distribution will be discussed with respect to its implications for the 200 ns noise in the next section. The shape of the distribution reveals a wide peak from detected SPE pulses (to the left), and a tall narrow peak (at the right) from noise pulses which leaked into the distribution. Noise pulses in the distribution typically have just enough of a voltage change to trigger the DSPE derivative threshold, but do not exist for very long, resulting in a very low integrated charge value.

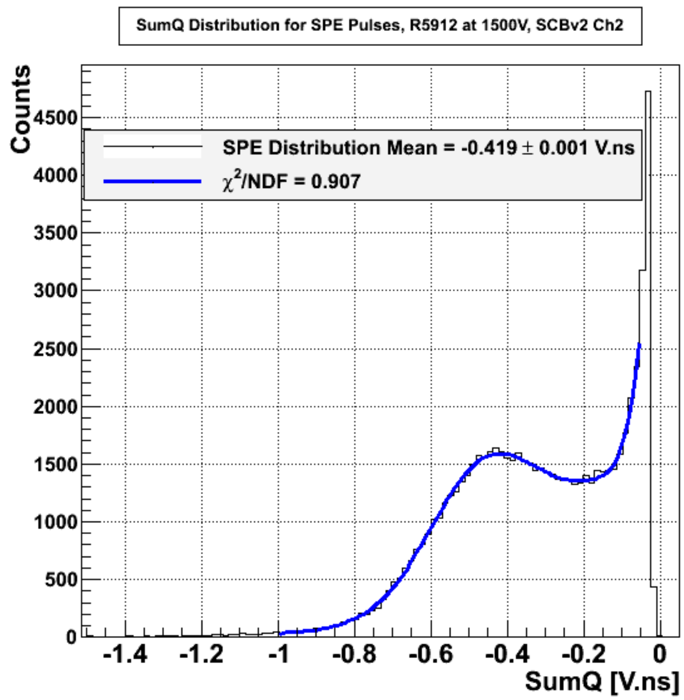


Figure 4.8: SumQ (integrated charge) distribution, for the SCBv2 Channel 2, with the PMT at 1500 V. The blue line shows the $9^{th}$ order polynomial fit which is used to determine the most probable SPE sumQ value. Leakage from noise pulses is seen at the right peak.

### 4.3.6 The SCBv2 Noise Distributions

The noise distribution for a single bin (4 ns) of the digitised waveforms is shown in Figure 4.9. The RMS of the distribution is 1.535 ± 0.005 ADC units, and is well described by a Gaussian function. Applying Equation 4.3, this RMS translates to a 4 ns noise level of 0.027 PE (± 0.4%) which is not sufficient for the design goal of 0.025 PE. Further discussion of this result is given at the end of the SCBv2 signal to noise discussion in Section 4.3.7.

Figure 4.10 shows a noise distribution for the SCBv2 for a 200 ns inte-

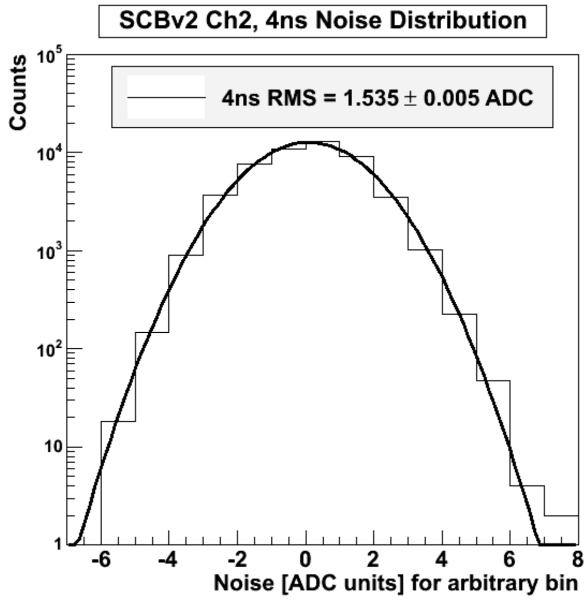


Figure 4.9: Noise distributions for 4 ns integration windows fit to a Gaussian (black curve) for the SCBv2.

grated window. The RMS of this distribution, again for a Gaussian fit, is 27.09 $\pm$ 0.09 ADC. The average charge value from the sumQ distribution, applied in conjunction with Equation 4.4, provides a measure of the noise in the 200 ns time window equal to 0.126 $\pm$ 0.004 PE. This fails to meet the design goal of $\leq$ 0.050 PE of noise per 200 ns time window. These results indicate reduction of the noise level would be a crucial feature in a subsequent version of the SCB. This may be partially offset by increasing the pulse width to enhance the average collected charge per SPE since the charge contained in an SPE pulse is directly related to the width of the pulse. Improvements of the 200 ns noise should augment the accuracy of $F_{prompt}$ and energy estimates, which are obtained by stacking separate PMT waveforms and integrating over extended time ranges. Seeking a low 200 ns noise level is desirable since the analog sum on the SCB adds the HG channels and is used to perform a preliminary estimate of the event energy and $F_{prompt}$ at the first stage of the data filter.

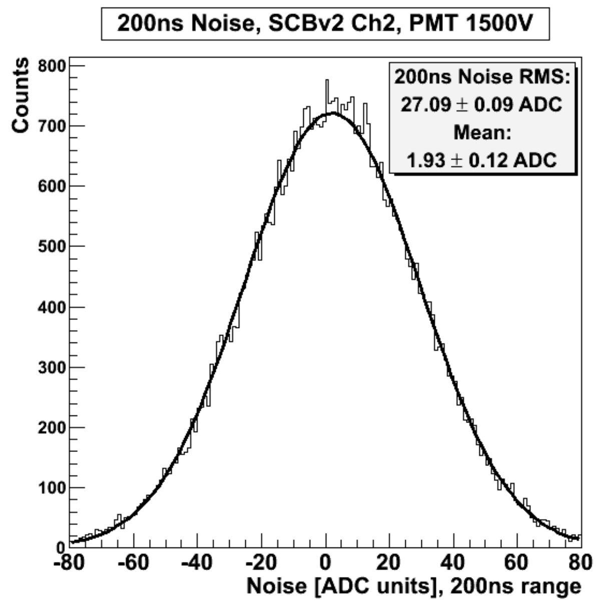


Figure 4.10: An example of a noise distribution for 200 ns integration windows for the SCBv2. The data are fit to a Gaussian shown as the black curve.

### 4.3.7 SCBv2 Signal to Noise Ratio

Referring to Figure 4.7, which showed the average waveform for the SCBv2 Channel 2 with a pulse height of 56.95 ± 0.11 ADC units (27.81 ± 0.05 mV), and Figure 4.9, showing a 4 ns noise distribution with an RMS of 1.535 ± 0.005 ADC units (0.750 ± 0.002 mV), one obtains a signal to noise ratio of:

$$\mathrm{S2N}_{SCBv2} = \frac{Avg\ Height = 27.81\ \mathrm{mV}}{Noise\ RMS = 0.750\ \mathrm{mV}} = 37.1\ \ . \qquad (4.6)$$

The error for this signal to noise value is ± 0.4%. This signal to noise ratio is acceptable, exceeding the design goal of 30. However, the inverse translates to a 4 ns noise level of 0.027 PE (± 0.4%), which does not meet the goal of 0.025 PE. This result indicates that the next iteration of the SCB should have a smaller 4 ns noise RMS, and an increased pulse height (amplification). These two changes will increase the signal to noise ratio and reduce the noise to a level which is deemed acceptable.

### 4.3.8 Summary of the SCBv2 Benchmark Tests

The results of the SCBv2 performance tests are summarised in Table 4.1. These results indicate that the overall noise level requires reduction in the next iteration of the SCB. An alternative amplifier selection may also potentially increase the signal to noise ratio. The effects of changing amplifiers are discussed in the SCBv3 Design and Specifications section.

Table 4.1: Summary of the results of the SCBv2 performance tests.

| Parameter | Value | Units | Minimum Req. | Acceptable |
|---|---|---|---|---|
| Avg Pulse Height | $56.95 \pm 0.11$ | ADC | 40.96 | Yes |
| SumQ Peak | $-0.419 \pm 0.001$ | V·ns | - | - |
| 4 ns Noise | $0.027 \pm 0.4\%$ | PE | 0.025 | No |
| 200 ns Noise | $0.126 \pm 0.004$ | PE | 0.050 | No |
| Signal to Noise | $37.1 \pm 0.4\%$ | None | 30.0 | Yes |

## 4.4 The Signal Conditioning Board Version 3b Pre-Testing

### 4.4.1 SCBv3b Design and Specifications

The next version of the SCB had twelve channels, each with varying pulse shapes, coupling capacitances, and two types of amplifiers. The purpose of this board (referred to as SCBv3b) was to determine an optimal pulse width, coupling capacitance, and to determine the ideal high gain channel amplifier (providing minimal noise) for the DEAP-3600 detector. Specifications for each of the twelve channels are outlined in Table 4.2. Note that the coupling capacitor can affect the rise and fall time of the pulse while the amplifiers affect the pulse height, pulse shape, and noise levels of the waveforms. The SCBv3b had one channel using the amplifier from SCBv2 (the AD8005), with the remaining channels using a new amplifier (the AD8001) which is faster than the

AD8005, providing an increased bandwidth of 800 MHz. This increased speed ($3\times$ faster than the old amplifier) comes at the expense of requiring roughly 12 times more power (50 mW). The increased speed is expected to reduce an issue of changing pulse shape with pulse height observed with the AD8005 (discussed in Section 4.4.5).

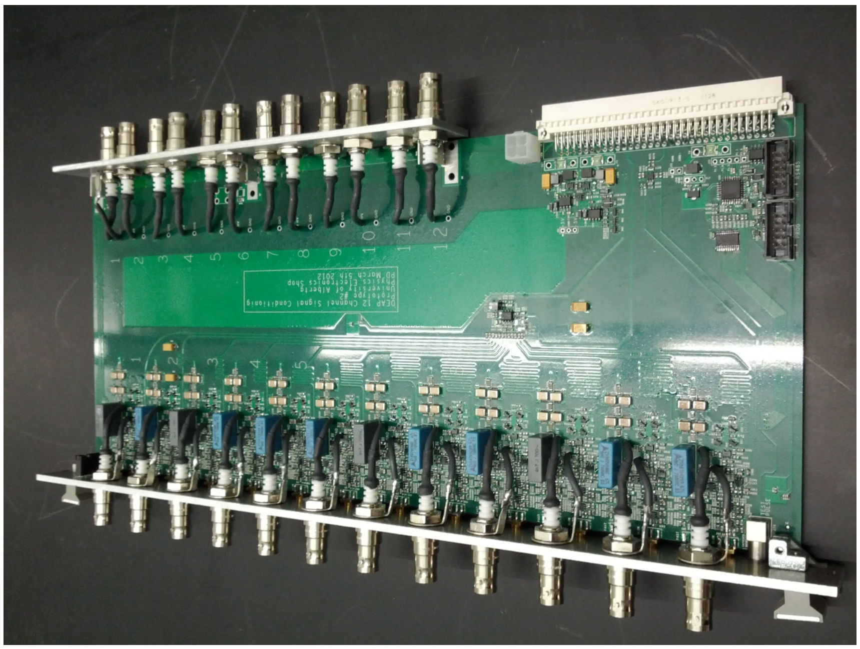

Figure 4.11: A photograph of the SCBv3b, with twelve populated channels (HG and LG). The board is powered by the large pin (top right), which is also used for slow control (turning on and off individual channels externally).

An image of the SCBv3b is shown in Figure 4.11, where the SHV cables connecting to the HV power supply connect to the twelve inputs shown at the top of the image. The HV is supplied to the PMTs with the twelve connectors shown at the bottom of the image. The components (resistors, capacitors) shown near the bottom connectors perform the PMT signal decoupling and pulse shaping. The large connector pin (top right corner) provides power to the board components and slow control.

The degree of pulse shaping is determined by:

$$\tau_{RC} = R_{circuit} C_{circuit} \ , \tag{4.7}$$

Table 4.2: Specifications for the individual channels on the SCBv3b. $\tau_{RC}$ is the time constant of the pulse shaping circuit.

| Channel | HG Amp | Capacitance [nF] | Pulse Shaping | $\tau_{RC}$ [ns] |
|---|---|---|---|---|
| 1 | AD8005 | 4.7 | Wide | 8 |
| 2 | AD8001 | 4.7 | Wide | 8 |
| 3 | AD8001 | 4.7 | Wide | 8 |
| 4 | AD8001 | 6.8 | Wide | 8 |
| 5 | AD8001 | 8.2 | Wide | 8 |
| 6 | AD8001 | 4.7 | Narrow | 4 |
| 7 | AD8001 | 4.7 | Narrow | 4 |
| 8 | AD8001 | 6.8 | Narrow | 4 |
| 9 | AD8001 | 8.2 | Narrow | 4 |
| 10 | AD8001 | 4.7 | Medium | 6 |
| 11 | AD8001 | 6.8 | Medium | 6 |
| 12 | AD8001 | 8.2 | Medium | 6 |

where $R_{circuit}$ and $C_{circuit}$ are the resistance and capacitance of the pulse shaping circuit.

### 4.4.2 Pre-testing the SCBv3b to Determine Optimal Channel Characteristics

The following sections, 4.4.3 - 4.4.7, discuss a number of preliminary tests with the SCBv3b to determine the channel with optimal characteristics for DEAP-3600. Once an ideal channel is selected, the analysis described previously in the Analysis Methodology section is performed. Thorough analysis is only completed for the ideal channel to reduce unnecessary testing on channels that will not be considered in the final design.

### 4.4.3 The SCBv3b Pulse Shape Differences for Different Coupling Capacitances

The effect of changing the coupling capacitance on the SPE pulse shape is investigated in this section to determine an optimal value. To investigate potential pulse shape changes with increased accuracy, a 5 GigaSamples/second oscilloscope is used in place of the digitiser to average the SPE waveforms. The oscilloscope is set to trigger on SPE pulses from the PMT, which is supplied 1400 V to inhibit the dark count rate. Waveforms containing averaged SPE pulses are saved and plotted together on a single graph. Three channels with the same pulse shaping but varying coupling capacitance are overlaid with the peaks of the average waveforms aligned. Nine channels (three pulse widths, three capacitances) are shown on the same graph in Figure 4.12. The overall trend demonstrates that the rise and fall time is essentially identical for all of the coupling capacitances, with slight variations in the average height of the SPE pulse.

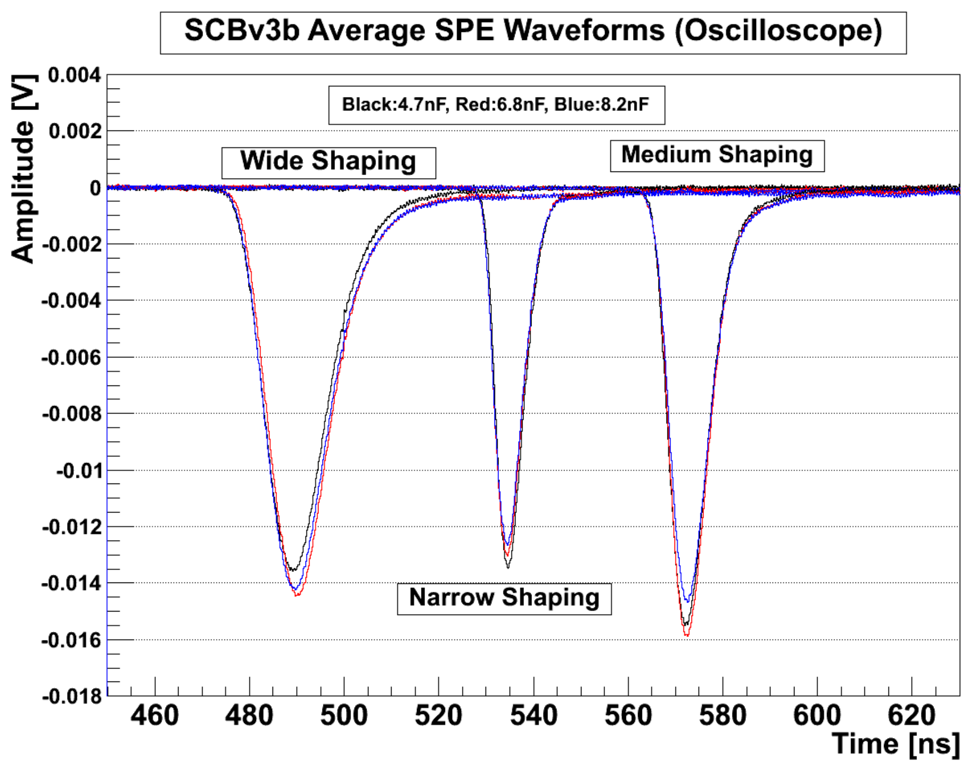


Figure 4.12: Average SPE waveforms for each pulse width (4, 6, and 8 ns time constants), with coupling capacitance varied from 4.7 nF to 8.2 nF.

To further investigate differences between pulse shapes for various coupling capacitances, the 6 ns time constant (medium width) channel data is plotted with normalised pulse heights (see Figure 4.13). The increase in capacitance results in a slightly longer rise time (return to baseline). A faster return to baseline is desirable because it reduces the possibility of SPE pulses overlapping. Following this result, the 4.7 nF coupling capacitance was chosen for the final design implementation of the Signal Conditioning Boards to minimise the time of return to baseline.

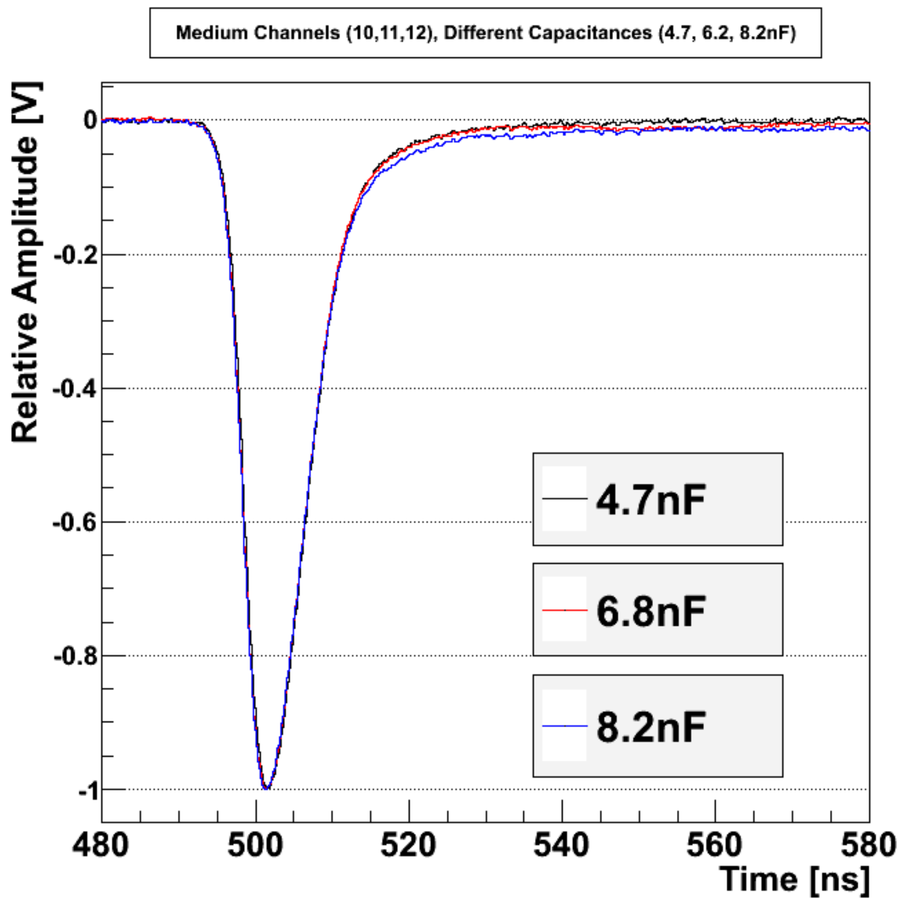


Figure 4.13: Average SPE waveforms for medium pulse shaping (Channel 10 through Channel 12), varying the coupling capacitance. Pulse heights are normalised to one.

### 4.4.4 The SCBv3b Signal to Noise Ratio for Different Pulse Widths

The next step in pre-testing the SCBv3b involves determining an optimal pulse width. Three channels (2, 6, and 10) with different pulse widths are compared while the other components of the channel are kept constant, with 4.7 nF coupling capacitors and the AD8001 amplifier. The wide channel (Channel 2) uses an 8 ns time constant pulse shaping, the medium channel (Channel 10) has a 6 ns time constant, and the narrow channel (Channel 6) has a 4 ns time constant.

Data is taken with the digitiser while the LED and R5912 PMT setup are operated in SPE mode. SPEs are extracted from the digitised waveforms using DSPE, and average SPE waveforms are generated. The 4 ns noise distributions are also generated, and fit with a Gaussian. The resulting average SPE pulse height and noise RMS values are used to calculate a signal to noise ratio for each of the three channels. Results are shown in Figure 4.14, and summarised in Table 4.3. Based on the signal to noise ratio, and overall lowest noise level, the medium pulse shape channel (6 ns, Channel 10) is selected as having the optimal pulse width. These measurements prompted a 6 ns time constant to be implemented in the design of the final version of the signal conditioning boards.

Table 4.3: Summary of the SCBv3b pre-test results.

| Channel | Pulse Width | Parameter | Value |
|---|---|---|---|
| 2 | Wide | Noise RMS | $1.044 \pm 0.003$ ADC |
| 2 | Wide | Signal to Noise | $65.2 \pm 0.01$ % |
| 6 | Narrow | Noise RMS | $0.976 \pm 0.003$ ADC |
| 6 | Narrow | Signal to Noise | $48.9 \pm 0.01$% |
| 10 | Medium | Noise RMS | $0.972 \pm 0.003$ ADC |
| 10 | Medium | Signal to Noise | $63.876 \pm 0.01$% |

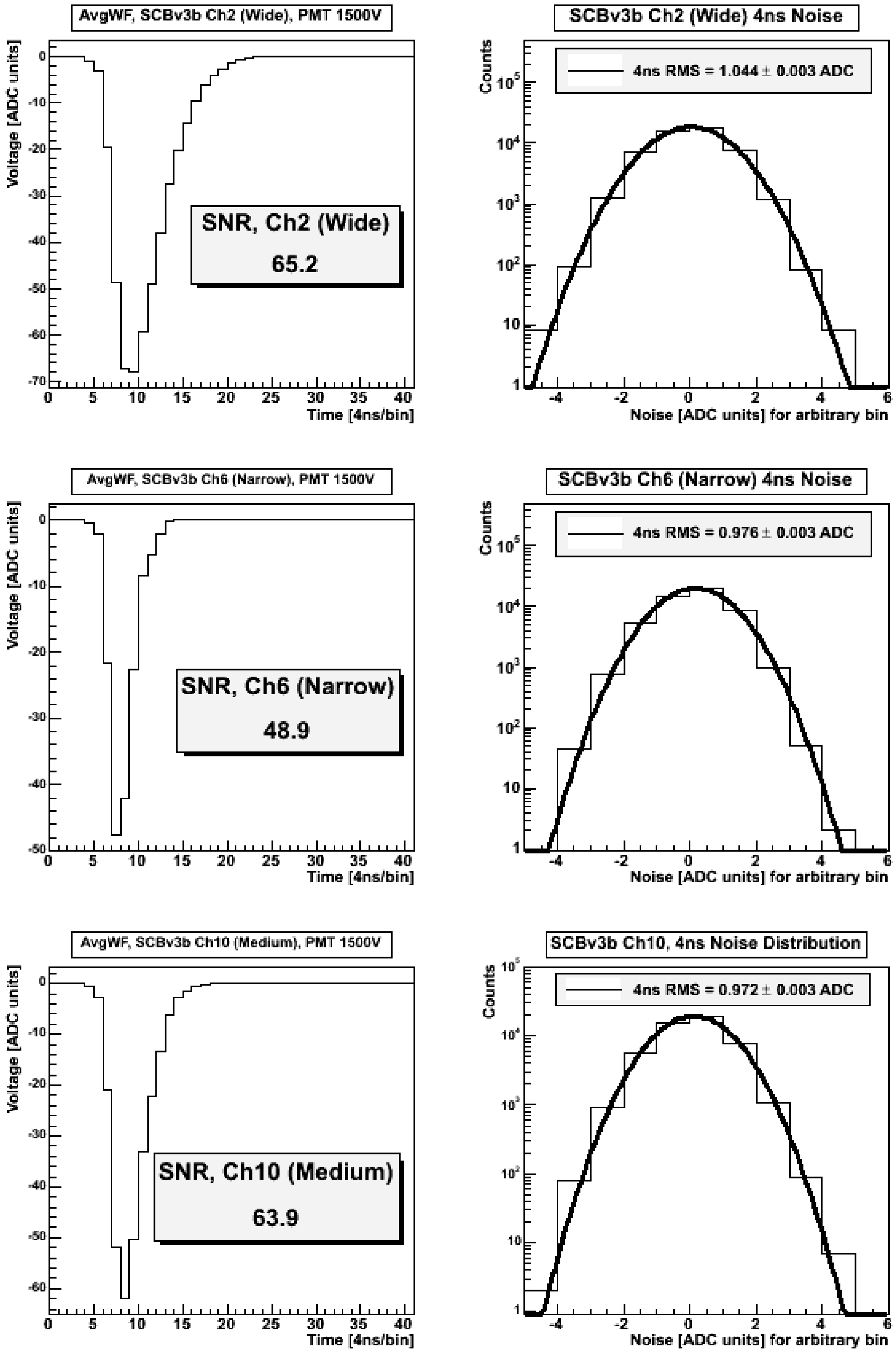


Figure 4.14: Average SPE waveform, 4 ns window noise distributions, and signal to noise ratio for three different pulse width channels on the SCBv3b.

### 4.4.5 The SCBv3b High Gain Pulse Shape Differences for Two Amplifiers

Both the SCBv2 Channel 2 and the SCBv3b Channel 1 use the AD8005 amplifier. The remaining channels on the SCBv3b (2-12) use the AD8001 amplifier. Channels using the AD8005 amplifier display a changing pulse shape with increasing pulse height, most notably in the rise time and overshoot feature, which is undesirable for a number of reasons. A changing pulse shape with pulse height complicates simulation of DEAP-3600 since a range of templates must be produced for different sized pulses. Pulse shapes that are constant with pulse height simplify the simulation of a multiple photoelectron pulse since it will closely resemble a scaled SPE pulse. A changing pulse shape with height also complicates extracting the number of photoelectrons contained in a large pulse. If the pulse shape remains constant with pulse height, the probability density functions used in the analysis to determine whether a pulse is from an SPE or multiple PEs remains consistent for all events.

To determine if the second amplifier (AD8001) reduces the effect of changing pulse shape with pulse height an arbitrary function generator (AFG) is used to produce a controlled pulse height input to the HG channel of the SCBv3b. Using the AFG instead of the PMT ensures greater precision over the size and shape of the input pulse, and hence a more consistent output pulse. The test input signal is tuned until the output pulse of the HG channel (on Channel 1) is $\sim$ 5 mV. The average pulse shape output by Channel 1 (AD8005) and Channel 2 (AD8001) is recorded with the 5 GigaSamples/second oscilloscope. The pulse height is then increased, generating HG output pulses with the following pulse heights: 25 mV, 50 mV, 100 mV, 250 mV, and 500 mV. The output pulses from Channel 1 and Channel 2 are scaled such that their heights are equal to 1.0 V and all pulses for each channel are plotted together.

Normalised height pulse shapes for increasing input pulse height are shown

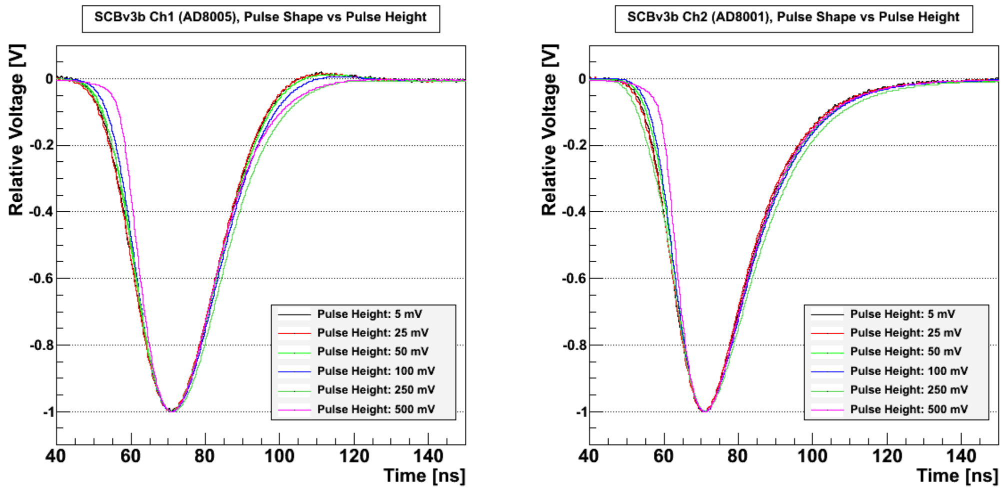


Figure 4.15: Average pulse shape waveforms for pulses of varying heights, generated for amplifier comparison: AD8005, left, and AD8001, right.

in Figure 4.15 for Channel 1 HG (AD8005, left) and Channel 2 HG (AD8001, right). Channel 1 shows a varying pulse shape with pulse height, most notably on the return to baseline. The smaller pulses (between 5 mV and 110 mV) have an overshoot of the baseline by a few percent upon return. The AD8001 amplifier on Channel 2 does not demonstrate this effect. The AD8001 amplifier has therefore been selected for the final version of the SCB. The demonstrated reproducibility of pulse shape with pulse height increases the accuracy of multiple photoelectron determination in DEAP-3600, and thus will maximise the energy detection efficiency as well as facilitate an accurate $F_{prompt}$ calculation, both of which are critical parameters for particle identification.

### 4.4.6 The SCBv3b Low Gain Pulse Shape Differences for Two Amplifiers

The TRIUMF picosecond light pulser setup with an R5912 PMT provides a similar pulse shape versus pulse height study for the low gain channel. The setup is first configured in SPE mode so that on average an SPE per waveform is recorded. An oscilloscope with a sampling rate of 2.5 GigaSamples/second is used to record average waveforms for Channel 1 LG on the SCBv3b. The light level is then doubled using variable light attenuators, and the next average waveform is recorded. This process is repeated up until a pulse size of 64 PE is achieved. The PMT gain for this test is not tuned, such that the dynamic range for the LG terminates at 10000 PEs since only the pulse shape as a function of pulse height is being considered. As before, the purpose of this study is to compare Channel 1 LG on the SCBv3b to Channel 10 LG on the SCBv3b and determine if the AD8001 amplifier has any effect on the pulse shape at various pulse heights. Average waveforms are collected with the oscilloscope, then are scaled so that all pulse heights are equal to one, and the peaks are aligned to occur at the same time. The results are shown in Figure 4.16, and a magnification of the overshoot region is shown in Figure 4.17.

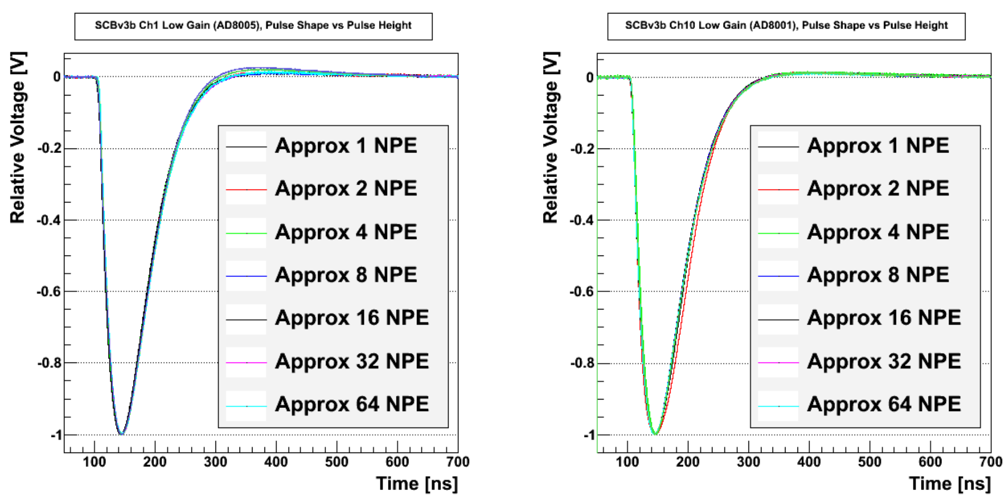


Figure 4.16: The SCBv3b Channel 1 LG vs Channel 10 LG: pulse shape versus changing input pulse height. Output pulse heights normalised.

Figure 4.16 (left) indicates Channel 1 LG experiences a greater overshoot than Channel 10 LG (right). This is confirmed in Figure 4.17. Channel 10 LG has a much more consistent pulse shape with pulse height in the overshoot region, confirming the results of the study of the high gain channel. The AD8001 amplifier provides greater pulse shape consistency with increasing pulse height in the overshoot region, as well as a lower overall level of overshoot, and for these reasons it will be used in the final version of DEAP-3600's signal conditioning boards.

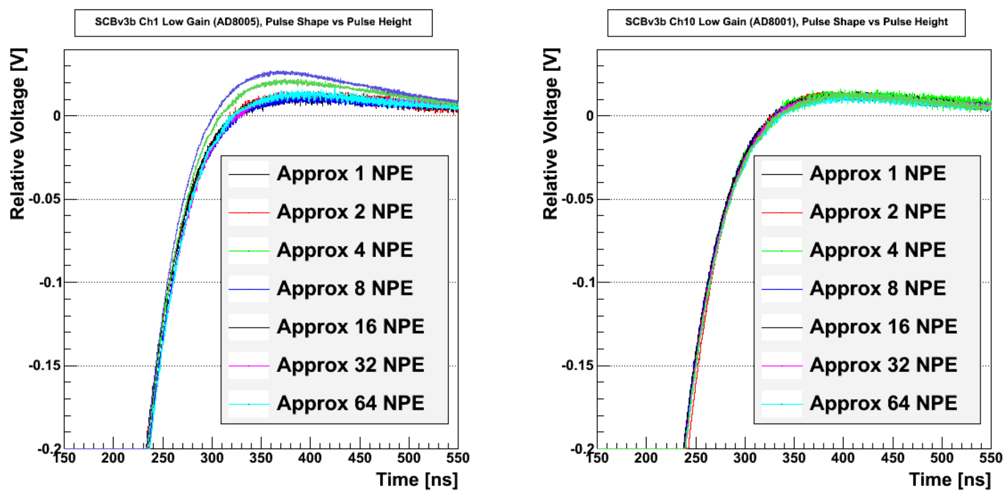


Figure 4.17: The SCBv3b Channel 1 LG (left) and Channel 10 LG (right), magnification of the overshoot region.

### 4.4.7 Summary of Results from SCBv3b Pre-Testing

Results of the pulse shape examination for various coupling capacitors indicate that a 4.7 nF coupling capacitor is ideal. Signal to noise ratios for various pulse widths leads to the decision that the 6 ns time constant pulse shaping is most desirable. Finally, the results of the HG and LG pulse shape for different amplifiers lead to the conclusion that the AD8001 amplifier is preferred for DEAP-3600's application. The end result of the pre-testing is that SCBv3b Channel 10 will be used as a blue print for the final SCB channel design.

## 4.5 The SCBv3b Channel 10 Performance Tests

After determining an optimal pulse width, amplifier, and coupling capacitance, the SCBv3b Channel 10 was chosen as having the optimal characteristics for signal conditioning. Recall that this channel has a 6 ns time constant for pulse shaping (medium), 4.7 nF coupling capacitance, and uses the AD8001 amplifier. The following sections present the same analysis as performed on the SCBv2 to determine the performance of the SCBv3b Channel 10.

### 4.5.1 The Channel 10 Pulse Height Distributions

Figure 4.18 shows the pulse height distributions (PHD) generated for the R5912 PMT at various input voltage levels. The setup is operated in SPE mode so that the pulse height distributions show regions of noise to the left (near zero) and SPE pulse height distributions (which are wider) at larger pulse heights. Similar to the PHDs for the SCBv2, Figure 4.18 shows a smoothly increasing average SPE pulse height with PMT voltage and a gradual widening of the SPE pulse height distribution.

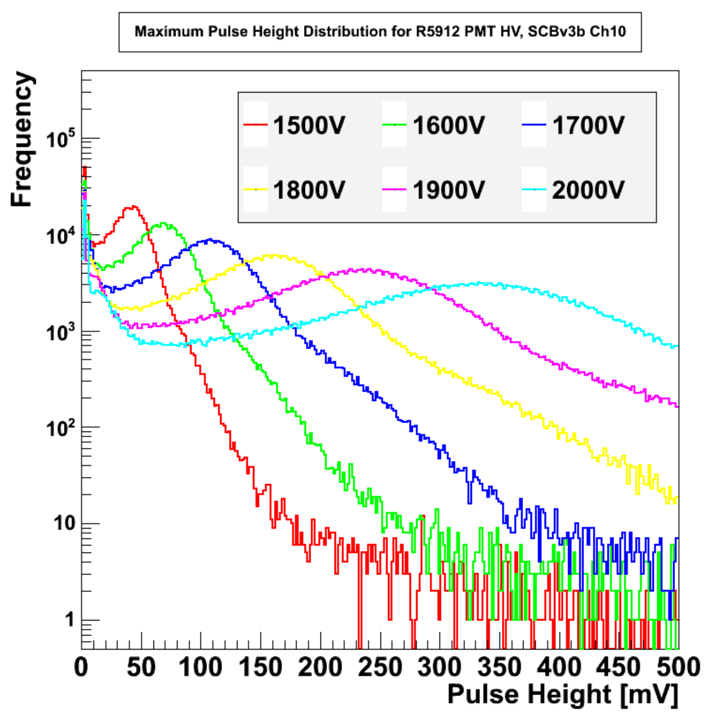


Figure 4.18: Pulse height distribution for the R5912 PMT at various supply voltages with SPEs conditioned by the SCBv3b Channel 10.

### 4.5.2 The Channel 10 Peak to Valley Ratio

The peak to valley ratio versus PMT HV (Figure 4.19) shows a linear trend without the plateau effect at the maximum PMT voltage that was observed with the SCBv2 Channel 2. The peak to valley ratio was calculated in the same manner as SCBv2 where a $6^{th}$ order polynomial function is fit to the region of the SPE distribution. From the fit the minimum of the valley between the SPE distribution and noise region is obtained along with the maximum value of the SPE distribution. The plot on the right of Figure 4.19 shows the most probable SPE pulse height versus PMT HV. As before, a second order polynomial function describes the data well. Figure 4.19 indicates the board is performing within expectation of the desired design specification, and the HV of the PMT may be increased to maximise the SPE gain without incurring unexpected behaviour in the pulse height distribution.

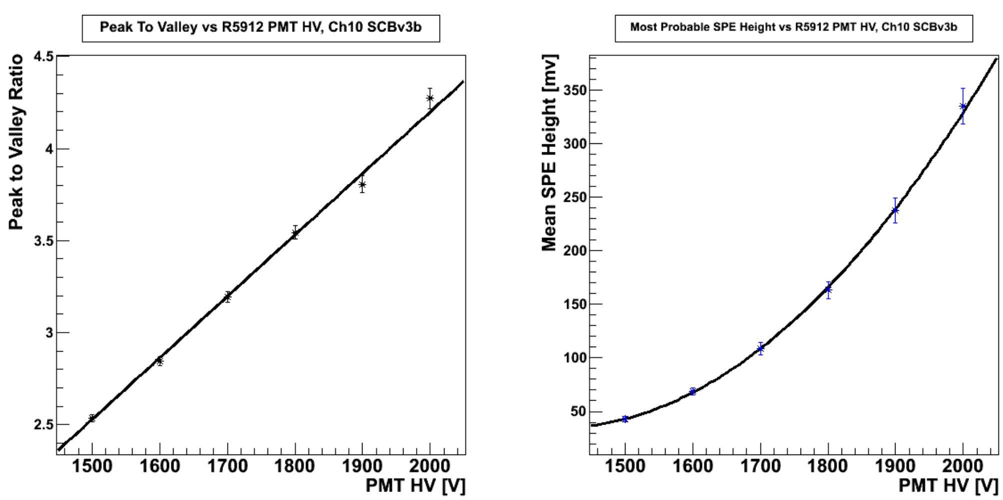


Figure 4.19: The SCBv3b peak to valley ratio versus PMT HV (left), and most probable SPE pulse height versus PMT HV (right). The fit on the left returned a reduced chi squared value of 1.03, while the fit on the right returned a reduced chi squared value of 0.10.

### 4.5.3 The Channel 10 Average Waveforms

The SCBv3b SPE average waveforms are produced while applying 1500 V to the PMT base. The average waveform for Channel 10 is shown in Figure 4.20 (blue curve) with a pulse height of 30.33 $\pm$ 0.06 mV. Also shown in Figure 4.20 for reference is the SCBv2 Channel 2 average waveform (black curve). The error in the calculated S2N ratios for both waveforms is 0.4%. For the SCBv3b Channel 10 the fall from baseline (fall time) is $\sim$ 16 ns, and the rise time (return to baseline) is $\sim$ 28 ns. The fast fall time is ideal for the SPE search algorithms, like DSPE, that use the derivative of the pulse for detection. The pulse height is very similar to the SCBv2 average waveform's pulse height, with an increase of $\sim$4%. This increase is likely due to two factors: the change in amplifier, and the lower noise level that reduces the leakage of small noise pulses into the average waveform. The rise time of the average waveform from Channel 10 is also a bit slower than the rise time of the SCBv2 average waveform, which is expected from the difference in pulse widening (4 ns time constant in SCBv2, and 6 ns in SCBv3b Channel 10).

### 4.5.4 The Channel 10 SumQ Distribution

The sumQ distribution for the SCBv3b Channel 10, shown in Figure 4.21, is fit with a $9^{th}$ order polynomial to determine the mean value of $\mu_{SPE}$=-0.604 $\pm$ 0.003 V·ns. The setup was operated in SPE mode, following the procedure used for the SCBv2 tests. The increased pulse width, relative to the SCBv2, provides a mean sumQ value increase of 44%. This increased mean is beneficial in that it will aid in distinguishing SPE pulses from noise when $F_{prompt}$ estimations by integration (waveform summing) are used. The reduced $\chi^2$ value of 0.971 indicates the $9^{th}$ order polynomial predicts the data well.

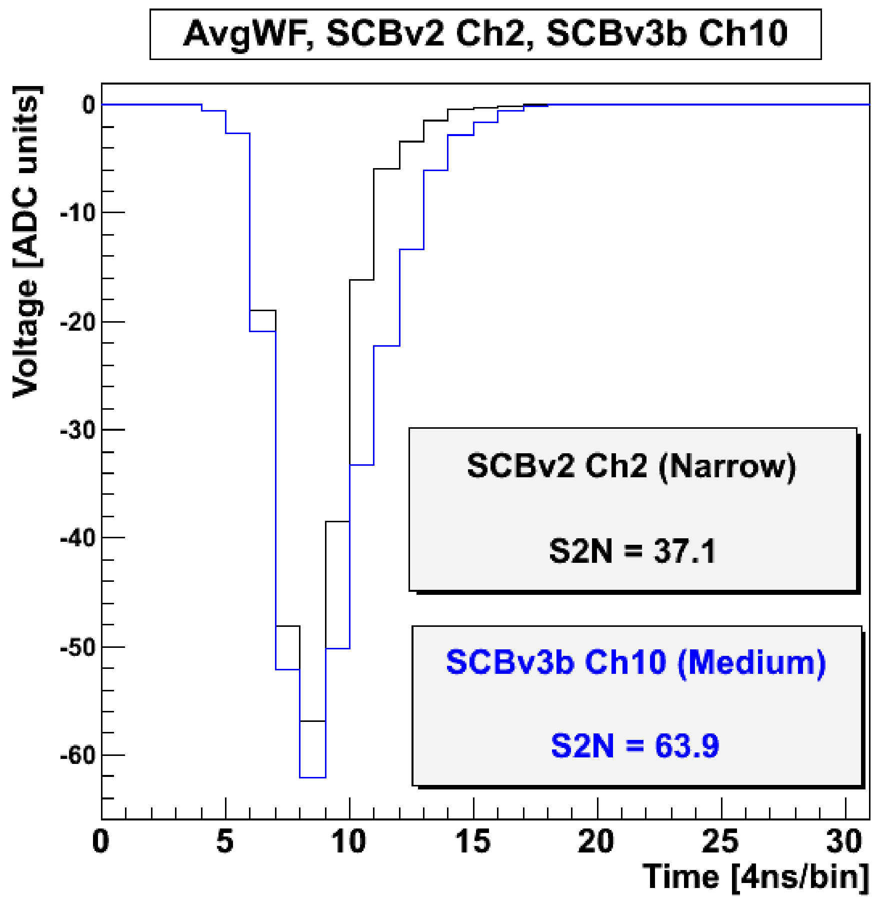


Figure 4.20: Average waveform for an SPE with the R5912 PMT operating at 1500 V, for the SCBv3b Channel 10 (blue) and SCBv2 Channel 2 (black). Signal to noise ratio is shown in legend.

### 4.5.5 The Channel 10 Noise Distributions

The 4 ns noise distribution for the SCBv3b Channel 10 is shown in Figure 4.22, and is well represented by a Gaussian function. The distribution has a reduced width (standard deviation) compared to the SCBv2, decreasing from 1.535 $\pm$ 0.005 ADC RMS to 0.972 $\pm$ 0.003 ADC RMS. The new amplifier (AD8001) is the likely source of the noise reduction. Using Equation 4.3, the 4 ns noise level is $N_{SPE,4ns}$ = 0.016 PE ($\pm$ 0.4%), which meets the design specification of $\leq$ 0.025 PE.

The 200 ns noise distribution for the SCBv3b Channel 10, shown in Fig-

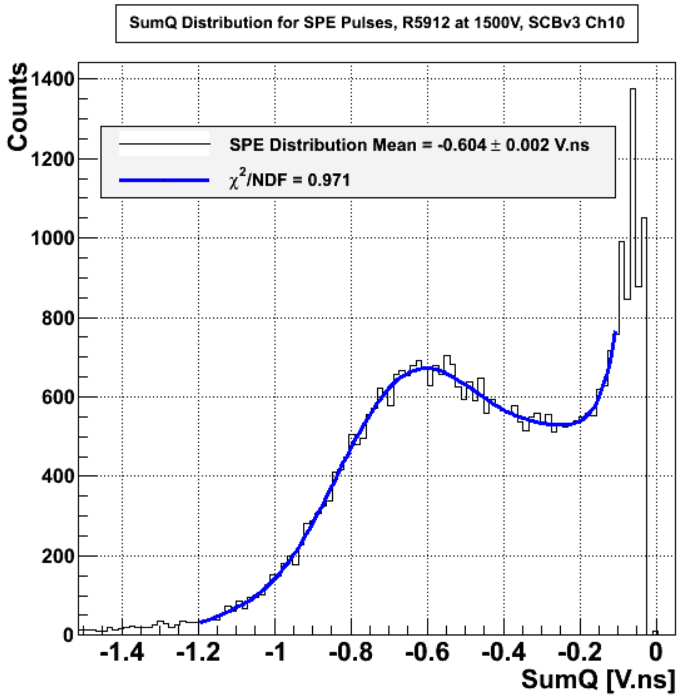


Figure 4.21: The SCBv3b Channel 10 sumQ distribution with a $9^{th}$ order polynomial fit (blue).

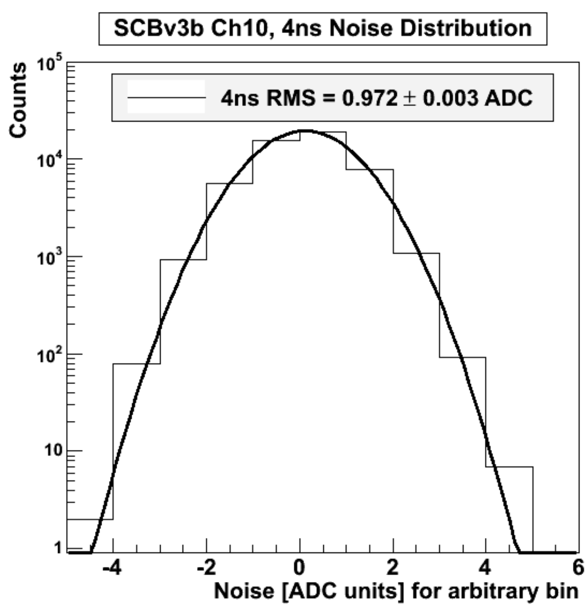


Figure 4.22: The SCBv3b Channel 10 4 ns noise distribution with Gaussian fit (black).

ure 4.23, is fit with a Gaussian function which returns an RMS of 12.70 ± 0.04 ADC. This is a significant reduction in width, 46.86%, from the SCBv2 Channel 2 distribution. Applying Equation 4.4, with appropriate units the noise for the 200 ns time window is $N_{200ns,PE} = 0.041$ PE (± 0.5%) which also meets the design criteria of $\leq$ 0.050 PE. The channel therefore has characteristics that permits an accurate estimation of $F_{prompt}$ and event energy by summing the high gain channels and integrating the total charge contained in the summed waveforms. Thus, the analog sum used for the initial stage of event filtering is expected to perform effectively with this noise level.

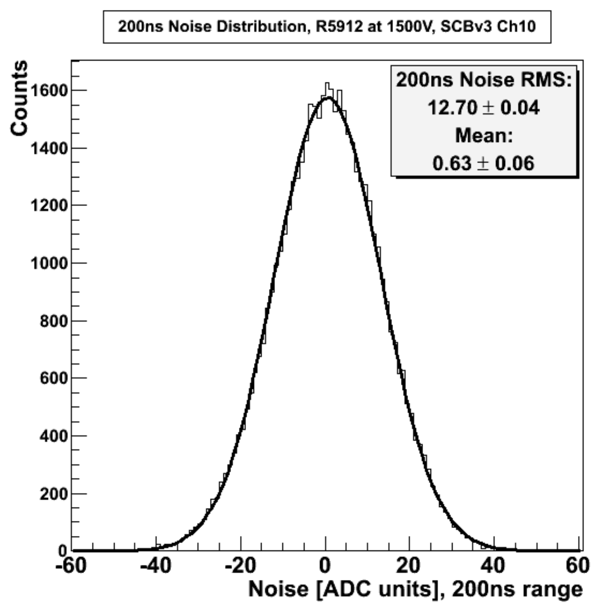


Figure 4.23: The SCBv3b Channel 10 200 ns noise distribution with Gaussian fit (black).

### 4.5.6 The Channel 10 Signal to Noise Ratio

From the output of Figure 4.20, pulse height, and Figure 4.22, noise distribution RMS, one may determine a signal to noise ratio for Channel 10 of:

$$\text{S2N}_{Ch10} = \frac{Avg\ Height = 30.33\ \text{mV}}{Noise\ RMS = 0.476\ \text{mV}} = 63.2 \tag{4.8}$$

This S2N level is more than double the design specification of 30, and 72% greater then the SCBv2, which translates to a 4 ns noise level in PE which meets design specifications.

### 4.5.7 Summary of Channel 10 Results

The results of the SCBv3b Channel 10 performance tests are summarised in Table 4.4. All of the tested parameters meet the DEAP-3600 design specifications that will permit accurate SPE detection and $F_{prompt}$ estimation when using the analog sum of the HG channels in the first stage of event filtering.

Table 4.4: Summary of the results of the SCBv3b Channel 10 tests.

| Parameter | Value | Units | Minimum Req. | Acceptable |
|---|---|---|---|---|
| Avg Pulse Height | 62.11 ± 0.12 | ADC | 40.96 | Yes |
| Avg SumQ | -0.604 ± 0.002 | V·ns | - | - |
| 4 ns Noise | 0.016 ± 0.4% | PE | 0.025 | Yes |
| 200 ns Noise | 0.041 ± 0.5% | PE | 0.050 | Yes |
| Signal to Noise | 63.9 ± 0.4% | None | 30.0 | Yes |

## 4.6 Final SCBv3 Specifications Tests

The last section of this chapter deals with analysis performed on the SCBv3 at TRIUMF to characterise the board for additional operation design specifications and performance. One requirement of the SCB is a linear correlation between the pulse heights of the LG and HG channels. Another is that the LG channel must only saturate the digitiser at $\sim$ 10000 PEs (or more) which will ensure surface alpha background events, that characteristically deposit large amounts of light in individual PMTs, may be accurately characterised.

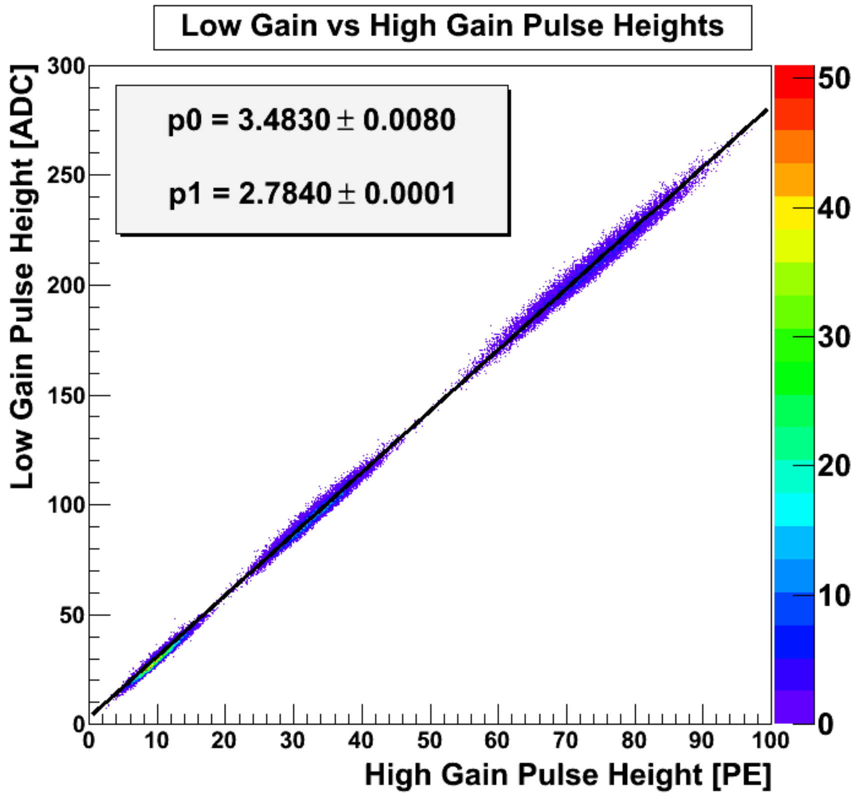


Figure 4.24: Low gain channel pulse height in ADC units versus high gain channel pulse height (PE) for the SCBv3 with the R5912 PMT operated at 1450 V. The different clusters of points represent different light levels, showing statistical variations in pulse height present in the data. The results of the $1^{st}$ order polynomial fit are shown in the statistics box.

### 4.6.1 Low Gain vs High Gain Correlation

The correlation between pulse heights of the HG and LG channels on the SCB should follow a linear relation up to a pulse height of $\sim$ 100 PE from the HG. The PMT is known to have a linear relationship between number of PE and pulse height in this region, and the SCB pulse shaping should not negatively affect this performance. That is, a linear correlation between the pulse heights produced by the two channels indicates that the pulse amplification on the HG channel is being performed linearly. In such a scenario, one may determine the light level where the HG channel saturates, permitting the low gain channel to be signalled for readout. This permits the detection and characterisation of high light output events, which will be necessary for understanding DEAP-3600 background events. To test the correlation between the LG and HG channels the pulser is set to varying levels of light intensity and waveforms for each channel are recorded. The corresponding pulse heights are calculated and plotted in Figure 4.24. A linear fit is performed on this data, to determine the correlation between the two pulse heights. Figure 4.24 shows the two channels are strongly correlated and also indicates HG channel pulse heights can exceed 100 photoelectrons without saturating the digitiser. If the HG channel was to saturate the digitiser, it would show up in Figure 4.24 as a vertical line at large HG pulse height values.

### 4.6.2 PMT Linearity Study

One of the performance criteria for the signal conditioning boards is the low gain channel should saturate the CAEN digitiser at $\geq$ 10000 PEs. This criteria ensures that if an alpha decay occurs on the surface of the acrylic vessel, generating a large amount of light in a single PMT [67], the electronics will still be able to record the full event information and thus efficiently reconstruct its energy.

To measure the saturation point of the low gain channel, the number of photons reaching the PMT is varied using digital optical attenuators, and the corresponding waveforms are recorded and analysed. For 10000 PE the pulse height of the low gain channel should be approximately 2.0 V, which maximises the dynamic range of the digitiser. Figure 4.25 shows the results for the measured pulse height versus average number of PEs generated by the PMT for three different signal types: SCB LG channel, SCB HG channel, and no SCB. For the "no SCB" test the PMT signal is split off from the high voltage using a special resistor/capacitor circuit that outputs the raw PMT pulse with no amplification and no pulse shape modification. The horizontal line in Figure 4.25 shows the 2.0 V dynamic range cutoff for the digitiser. If the

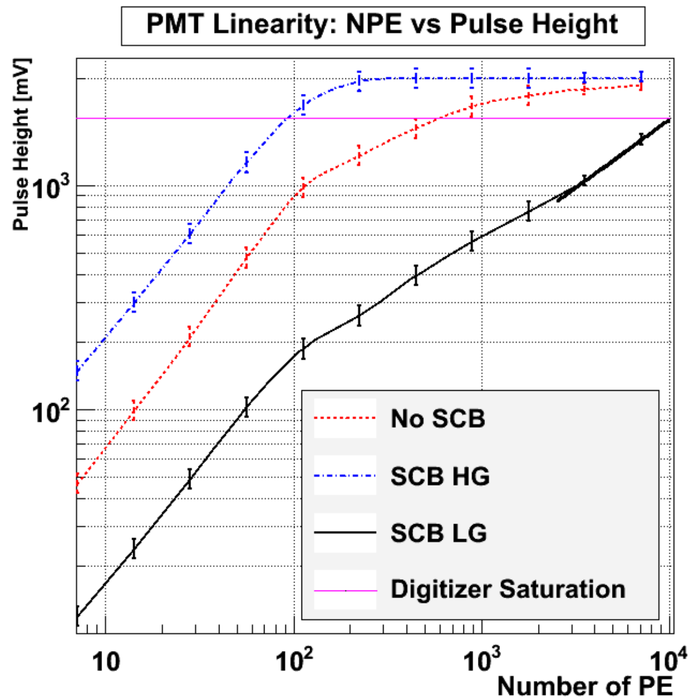


Figure 4.25: Pulse height for the SCBv3 HG channel, the SCBv3 LG channel, and no SCB for various light levels. The low gain channel is shown to intersect 2.0 V (pink horizontal line) at ∼ 10000 PEs.

SCB LG channel is extrapolated, an intersection with the 2.0 V line occurs near 10000 PE confirming that the SCB meets the large light event energy reconstruction criteria.

## 4.7 Concluding Remarks

The Signal Conditioning Boards used for the DEAP-3600 experiment will aid in the digitisation process by widening pulses to the point where their shapes can be accurately recorded by the CAEN V1720 digitisers. The SCBs will also improve the single photoelectron detection efficiency by increasing the signal to noise ratio of the digitised pulses. Low gain channels on the SCBs will be used for the detection of large light events, such as alpha decays on the inner acrylic surface of the DEAP-3600 vessel, which will saturate the high gain channels.

The first tested version of the SCB, SCBv2, was found to fall short of the design criteria for DEAP-3600 for 4 ns and 200 ns noise levels. The second tested version of the SCB (SCBv3b) had a channel (10) that was shown to meet the required specifications for the project. The SCBv3 noise levels are low enough to facilitate both single photoelectron counting and estimations of $F_{prompt}$ by summing waveforms and integrating the total pulse charges. The SCBv3b testing also provided finalised specifications for the last versions of the SCBs, including time constants used for pulse shaping, coupling capacitances, and amplifiers.

# Chapter 5

# Simulation of DEAP-3600 Waveforms and the Effect of the Electronics on WIMP Signal Extraction

The first section of this chapter will briefly describe the software used in the simulation of DEAP-3600 waveforms. The next section (RAT Simulation Parameters) describes the detector geometry implemented in the simulation, and provides a short description of the processes that occur during simulation.

Section 5.3 discusses the types of particles which are simulated for this analysis, with particular emphasis on astrophysical assumptions used for the WIMP modelling. The following section explains the different levels of electronics noise which were used in the simulated waveforms. Section 5.5 begins the simulation analysis by examining the effect of electronics noise on both a 100 GeV$\cdot$c$^{-2}$ WIMP signal and the $^{39}$Ar $\beta$-decay background. Section 5.6 investigates the effect of electronics noise on DEAP-3600 signal extraction by analysing $F_{prompt}$ distribution separations for various energy cuts. The last analysis section, Section 5.7, investigates how noise may affect the energy detection efficiency of

DEAP-3600 by comparing known event energies from the Monte Carlo data to reconstructed event energy. The radial distribution of simulated $^{39}$Ar $\beta$ events is discussed to explain features of the energy efficiency histograms. The chapter concludes with a section summarising the results of the simulation.

## 5.1 Detector Simulation

The Reactor Analysis Tool (RAT) is a simulation software package designed to model a scintillation detector surrounded by PMTs. It was initially developed by the Braidwood Collaboration for the purpose of generating Monte Carlo events and analysing the simulated data. RAT uses GEometry ANd Tracking version 4 (GEANT4), an object oriented simulation toolkit which can be used for a wide range of physics applications; from simple studies of basic particle passage through matter, to full-scale detector simulations of experiments at the Large Hadron Collider [68]. For event handling RAT uses ROOT [69], an object oriented analysis framework developed at CERN for handling large volumes of data. RAT also incorporates the GLG4sim (Generic Liquid scintillator anti-neutrino detector GEANT 4 simulation) package for additional physics about scintillator excitation states, enhancing the calculations related to the pulse shape discrimination results [70]. The RAT software has a data acquisition (DAQ) portion of code that is used to generate output in a format which is identical to the readout from the physical DEAP detector. Thus RAT may be used to simulate the data chain from event production through to the data output which will be generated. The output data can then be processed using ROOT or user generated programs, permitting testing and development of data analysis programs in advance of the actual experimental operation.

## 5.2 DEAP-3600 RAT Simulation Parameters

The geometry for DEAP-3600 was implemented in RAT by members of the DEAP collaboration prior to the author's work with the software. DEAP-3600 is modelled as an acrylic sphere, neck and lightguides. The sphere and neck are filled with liquid argon, and the sphere is surrounded by 255 PMTs located at the end of each lightguide. An additional 48 inward and outward facing PMTs act as a cosmic ray muon veto. The steel shell (Figure 3.2) which encases the acrylic vessel is included the simulation geometry, as well as the water shield tank (a 7.6 meter diameter cylindrical container surrounding the DEAP vessel). An image of this detector geometry is shown in Figure 5.1. The water, steel shell, and light guides are transparent in the image, although the outline of the shield tank can be identified by the rings of inward facing veto PMTs shown around the DEAP-3600 vessel.

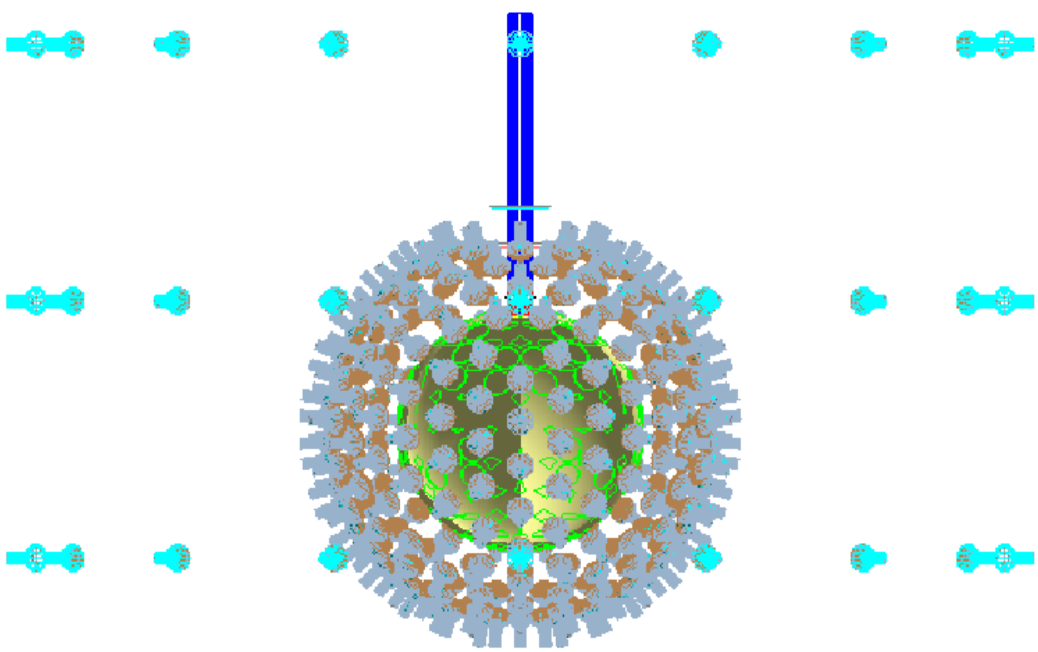

Figure 5.1: The DEAP-3600 detector geometry as implemented in RAT simulation software. Veto PMTs surrounding the detector show the outline of the water shield tank. Acrylic light guides excluded, but the vessel, the neck, and LAr PMTs are visible.

Once a particle interaction has occurred in the detector, the light created is tracked as it propagates in the volume. If light strikes the surface of a PMT, the time and hit location on the face of the PMT are recorded. The DAQ processor for RAT is then initiated, and it begins the event building. The DAQ processor then determines whether or not to generate a photoelectron from the incident photon, according to the quantum efficiency profile of the PMT. For example, a PMT with a quantum efficiency of 30% will generate 3 photoelectrons per 10 photons incident on the PMT (on average). If a photoelectron is produced, an electrical signal is simulated using the PMT response function incorporated into RAT by researchers at the University of Pennsylvania [71]. After the electrical signal from the PMT has been generated it is digitised and the resulting waveforms have electronics noise added at a user specified level. The waveforms are then compressed and stored in the file format that DEAP-3600 will use when in operation. Files containing digitised waveforms are then analysed with user generated front end programs.

## 5.3 RAT Simulated Particles

RAT is a versatile tool capable of simulating a wide range of particle types. For the purpose of this study, only two primary particles were considered: WIMPs and $^{39}$Ar $\beta$s. The properties of the simulated particle types are discussed in this section.

### 5.3.1 $^{39}$Argon $\beta$s

By far, the dominant signal detected by DEAP-3600 will be from $^{39}$Ar $\beta$-decays. $^{39}$Ar is produced in the upper atmosphere from cosmic ray spallation and neutron activation of stable argon [72], and decays via the reaction:

$$^{39}\text{Ar} \rightarrow \ ^{39}\text{K} + \beta + \bar{\nu}. \tag{5.1}$$

The resulting potassium isotope is stable (producing no effect on DEAP-3600's measurement), the anti-neutrino escapes the medium unimpeded, while the $\beta$ causes electronic recoils. $^{39}$Ar has a half life of 269 years, a natural abundance ($^{39}$Ar/Ar) of $(8.1\pm0.3)\times10^{-16}$, and a $\beta$-decay endpoint of 0.565 MeV [73]. The decay spectrum of $^{39}$Ar is shown in Figure 5.2. It should be noted that the decay spectrum encompasses the energy range of 20-80 keV which is of interest for WIMP interactions in DEAP-3600, and thus where pulse shape discrimination will be crucial for removing the $^{39}$Ar background events.

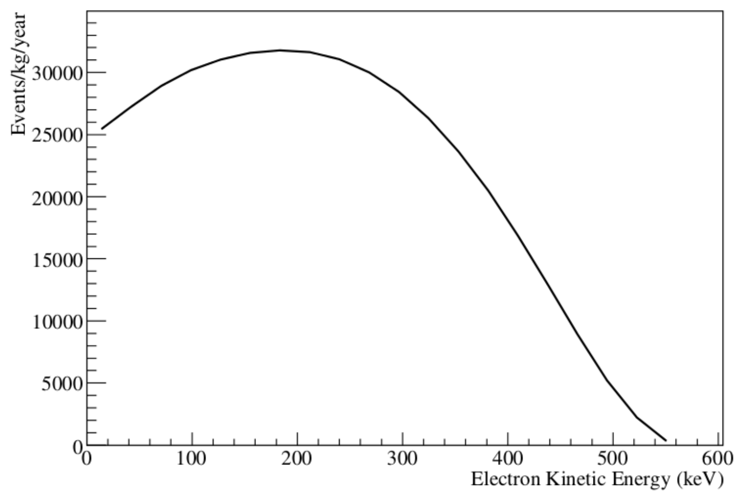


Figure 5.2: Rate of $^{39}$Ar $\beta$-decay events per kg of natural argon per year versus $\beta$ energy [74].

The measured specific activity for $^{39}$Ar is 1.01 $\pm$0.02(stat) $\pm$0.08(syst) Bq per kilogram of natural argon [75], which translates to roughly 3600 argon $\beta$-decays per second in DEAP-3600. In RAT, the LAr target volume is simulated with this activity according the the decay spectrum shown in Figure 5.2.

### 5.3.2 WIMPs

Weakly Interacting Massive Particles (WIMPs) are simulated in RAT by generating recoils of $^{40}$Ar nuclei (natural argon). The mass of the WIMP can be varied as a parameter in the simulation, although in this study the mass was set to 100 GeV·c$^{-2}$. The underlying astrophysical parameters used in the RAT simulation of WIMPs are shown in Table 5.1.

Table 5.1: WIMP RAT simulation input astrophysical parameters (Standard Halo Model) [76], [77], [78], [27].

| Parameter | Symbol | Value | Units |
|---|---|---|---|
| Local Galactic Escape Velocity | $v_{esc}$ | 544 ± 50 | km/s |
| Mean Galactic WIMP Velocity | $v_0$ | 220 ± 20 | km/s |
| Sun's Velocity Around Galactic Centre | $v_{Sun}$ | 232.0 | km/s |
| Earth-Sun Relative Velocity | $v_{Earth}$ | 15.0 | km/s |
| Local dark matter density | $\rho$ | 0.3 | GeV·cm$^{-3}$ |

WIMP interactions are set to generate a range of nuclear recoil energies between 20 keV and 300 keV, where the lower and upper energy range may be modified at run-time. The WIMP model also assumes an annual modulation in WIMP interactions based on the changing velocity of the Earth relative to the WIMP halo. The peak of the modulation (where the WIMP interaction rate is at a maximum) is set at March 1st of every year.

## 5.4 Noise Levels

The main focus of this simulation study is to determine the effect of various levels of electronics noise on DEAP-3600 measurements. These noise levels are meant to represent the idealised, realistic, and worst case scenario. Some noise distributions are generated from Gaussian functions, while others are generated directly from hardware in the DEAP-3600 electronics testbed.

- Zero noise: no noise is added to waveforms. This represents a control, as well as an idealised, noiseless electronics system.

- V1720 noise: noise histograms are generated by triggering the digitiser with no PMT signal input. This noise level represents the lowest realistically achievable level from the commercially obtained data acquisition component.

- SCBv3 noise: waveforms containing only noise (no pulses) are generated by the electronics testbed with the PMT HV applied, digitiser active, and SCBv3b configured. The digitiser is triggered at a frequency of a few hundred Hz and only waveforms containing no dark pulses are selected as noise-only waveforms. This noise level represents the most accurate description of electronics noise currently available for the DEAP-3600 experiment.

- Gaussian noise: electronics noise generated according to a Gaussian distribution. The standard deviation of the distribution is varied to represent different amounts of noise. A 0.460 mV standard deviation noise distribution is meant to reflect the SCBv3 noise level in the case that it were purely Gaussian and perfectly followed the black curve in Figure 4.22. A Gaussian distribution with a standard deviation of 0.700 mV (representing a noise level roughly 50% greater than current levels) is used to investigate the results of a hypothetical increase in noise. This type of noise does not account for pick-up noise (transient, low frequency noise) or bin to bin correlated noise.

## 5.5 Effect of Noise on DEAP's Signals

### 5.5.1 Effect of Electronics Noise on 100 GeV·c$^{-2}$ WIMP Distribution

To determine the effect of varying levels of electronics noise on a potential dark matter signal, nuclear recoils of natural argon from 100 GeV·c$^{-2}$ WIMPs are simulated in the DEAP-3600 fiducial volume. Photons from the WIMP interactions that intersect a PMT have their hit time and location on the PMTs recorded. No PMT response function is generated, and no digitisation is performed at this point in the simulation. A file containing information on the WIMP events is produced, and a secondary data processing code is later used to simulate the remainder of the DAQ chain, including the PMT response function, and additional electronics noise. The pulses are then digitised into waveforms and $F_{prompt}$ values are calculated for each event.

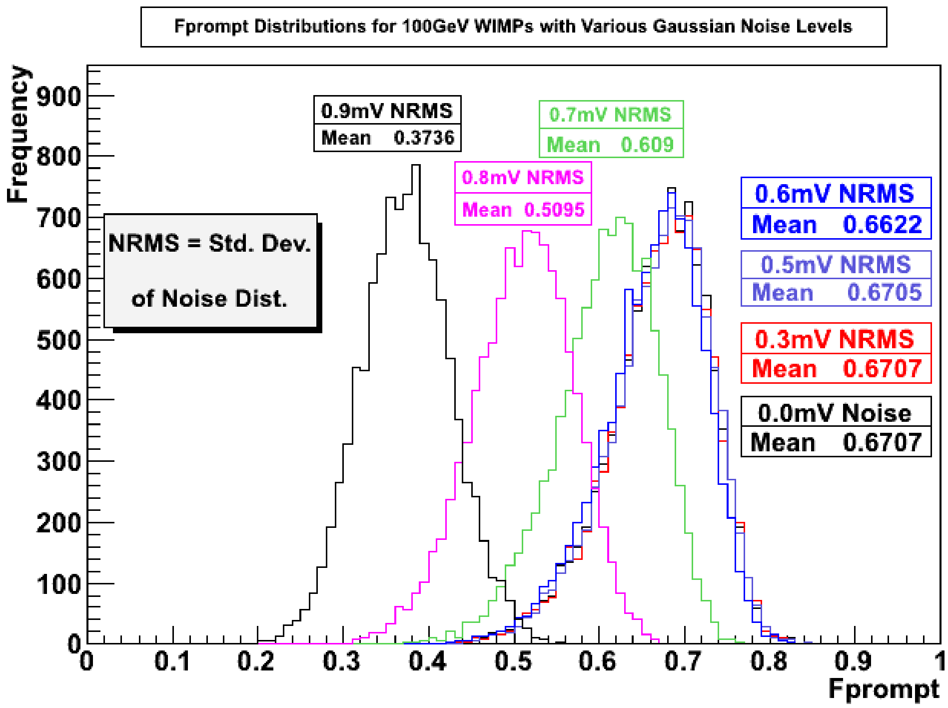


Figure 5.3: $F_{prompt}$ distributions of simulated 100 GeV$\cdot$c$^{-2}$ WIMPs for various electronics noise levels.

To investigate how increasing levels of Gaussian electronics noise affects the $F_{prompt}$ measurement of WIMP events, noise is added to waveforms from simulated WIMP interactions at the following levels: 0.0, 0.3, 0.5, 0.6, 0.7, 0.8, and 0.9 mV RMS. The noise amplitudes (in mV) for each digitised bin are created using a random number generator class in ROOT that samples a Gaussian distribution with the appropriate standard deviation. $F_{prompt}$ distributions of the WIMP events for the various noise levels are plotted on the same histogram (see Figure 5.3), and the mean value of each distribution is calculated. There is little to no shift in the mean of the distributions (less than 0.03% shift) for additional noise up to 0.5mV RMS. At 0.6 mV RMS, the $F_{prompt}$ distribution starts to shift to a lower value (1% decrease). The next noise level increase (0.7 mV) dramatically shifts the distribution to a lower mean value, and this trend continues for increasing noise levels. The extracted mean $F_{prompt}$ value for each distribution versus the noise RMS in mV is plotted in Figure 5.4. Uncertainties on the mean $F_{prompt}$ represent one standard deviation of the distribution. Figure 5.4 indicates that electronics noise has little to no effect on the $F_{prompt}$ measurement up to $\sim$ 0.6 mV RMS. At levels of 0.6 mV RMS and greater, electronics noise starts to impact the mean of the $F_{prompt}$ distribution for 100 GeV$\cdot$c$^{-2}$ WIMPs, moving it to lower values where the ability to distinguish nuclear recoils from electronic recoil events is reduced.

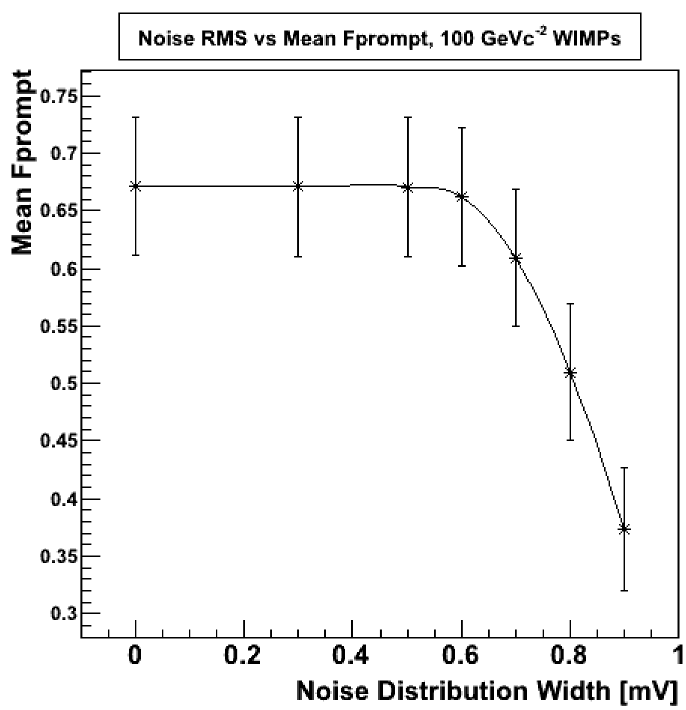


Figure 5.4: Mean $F_{prompt}$ value versus noise RMS (mV) for simulated 100 GeV$\cdot$c$^{-2}$ WIMPs.

### 5.5.2 Effect of Electronics Noise on Simulated $^{39}$Ar $\beta$ Events

The effect of varying levels of noise on the total $F_{prompt}$ distribution for $10^6$ $^{39}$Ar $\beta$-decays is investigated in this section. The $^{39}$Ar $\beta$-decays are simulated and the information up to the PMT interaction is recorded. Similar to the WIMP simulation, a secondary data processing code is later used to simulate the electronics noise and PMT response function. The $F_{prompt}$ of the events are then calculated, and the distributions for the various noise levels are superimposed on the same graph (see Figure 5.5). The most important feature to investigate on the $F_{prompt}$ distribution is the tail located on the high side of the distribution, since this would overlap with the WIMP region. The shape of the distribution's tail is what determines how low the threshold may be set on the deposited recoil energy from a WIMP interaction.

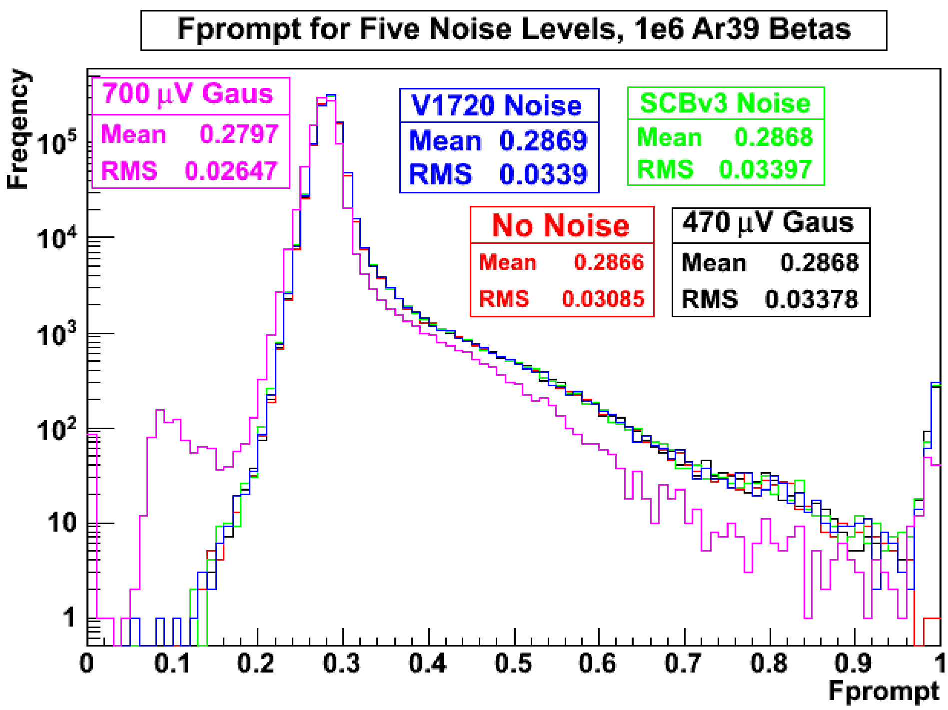


Figure 5.5: $F_{prompt}$ distributions for $10^6$ simulated $^{39}$Ar $\beta$-decays with various simulated electronics noise levels added to the waveforms.

One finds for noise levels between 0 mV RMS and $\sim$ 0.5 mV RMS, the $F_{prompt}$ distribution mean values change by less an 0.1%, and the distribution shape remains consistent. However, when the simulated noise is set to 0.7 mV RMS, the $F_{prompt}$ distribution mean decreases 2.5%, and the distribution develops a new feature at $F_{prompt} \sim 0.1$. This result indicates that current noise levels, from the SCBv3, are comparable to the lowest realistically achievable noise levels, from the V1720 alone, in terms of their effect on the $F_{prompt}$ distribution of $^{39}$Ar $\beta$-decays. If the noise distribution RMS were to roughly double ($\sim$ 0.7 mV RMS), the $F_{prompt}$ distribution would undergo noticeable changes to both the shape and mean value. For this reason, noise levels should be maintained at current levels or lower to prevent undesired $F_{prompt}$ distribution changes.

## 5.6 Effects of Noise on $F_{prompt}$ Distribution Separation for $^{39}$Ar and WIMPs

A measure of how well the $^{39}$Ar $\beta$-decay signal can be discriminated from WIMP induced recoils is determined by measuring the separation of the $F_{prompt}$ distributions for specific energy ranges. This is done by plotting the signal (WIMPs) and background ($^{39}$Ar) together on a histogram showing event energy, measured in total detected charge in photoelectrons (qPE), on the x-axis and $F_{prompt}$ on the y-axis. The $F_{prompt}$ vs detected energy (in qPE) for $10^6$ $^{39}$Ar $\beta$-decays and $10^4$ WIMPs (100 GeV$\cdot$c$^{-2}$ mass) is shown in Figure 5.6 as an example.

The energy of the event can later be converted to keV after the number of keV deposited per PE generated is determined from calibrations. For the simulation geometry, an average light yield of 11.3 PE/keV was extracted and is used for the conversion described above. Figure 5.6 shows the $\beta$ and nuclear recoil $F_{prompt}$ distributions appear to be well separated above about 220 qPE, which corresponds to $\sim$ 20 keV, the lower energy threshold of the DEAP-3600

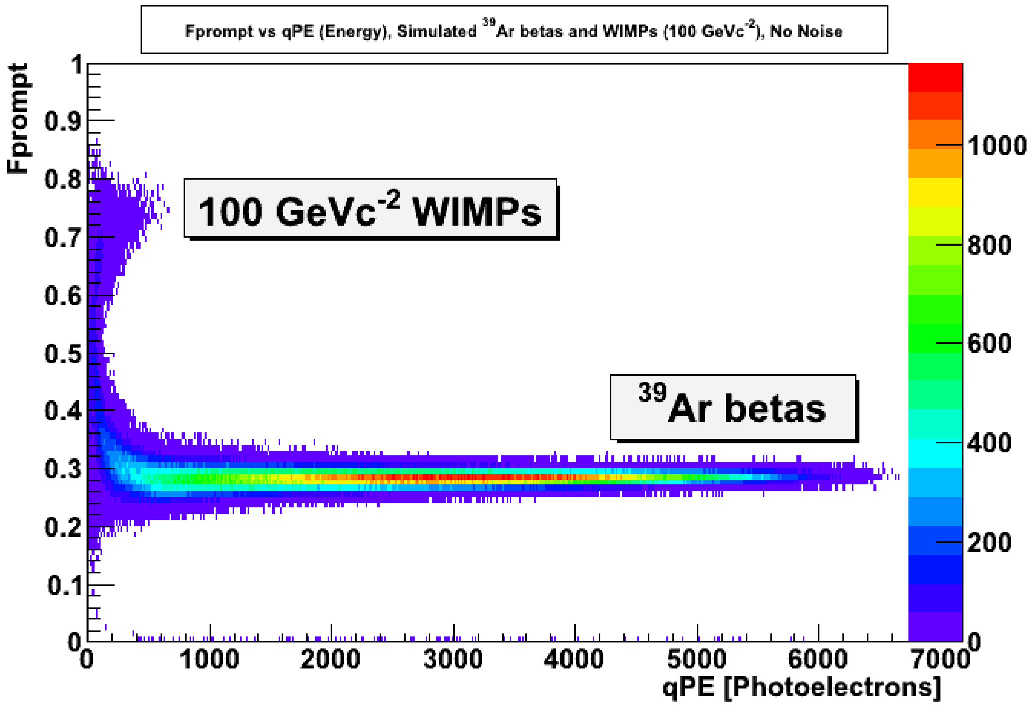


Figure 5.6: $F_{prompt}$ versus event energy (measured in detected photoelectrons) for simulated $^{39}$Ar $\beta$ events and 100 GeV$\cdot$c$^{-2}$ WIMPs, when no electronics noise is added to the waveforms.

detector design. The z-axis colour in the 2D histogram represents the frequency of points in each bin.

To measure $F_{prompt}$ separation, energy ranges of interest are selected and events falling outside of these windows are removed. The ranges considered in this study are 20 - 40 keV and 40 - 80 keV, chosen for the region where WIMPs events are favoured. Due to the lower number of events in the 40 - 60 keV and 60 - 80 keV windows, these two ranges were merged (40 - 80 keV) to increase the statistics used for the fit. Once events outside these energy ranges are removed, the y-axis is projected and the separation between the distributions is determined. An overlap of the distributions indicates potential leakage of background events into the WIMP signal region. If the two distributions are well separated then the discrimination power of the detector in that energy range is large, and the detector may be considered background free. The purpose of this study was to determine how varying levels of noise may affect the $F_{prompt}$ distribution separation for signal and background events.

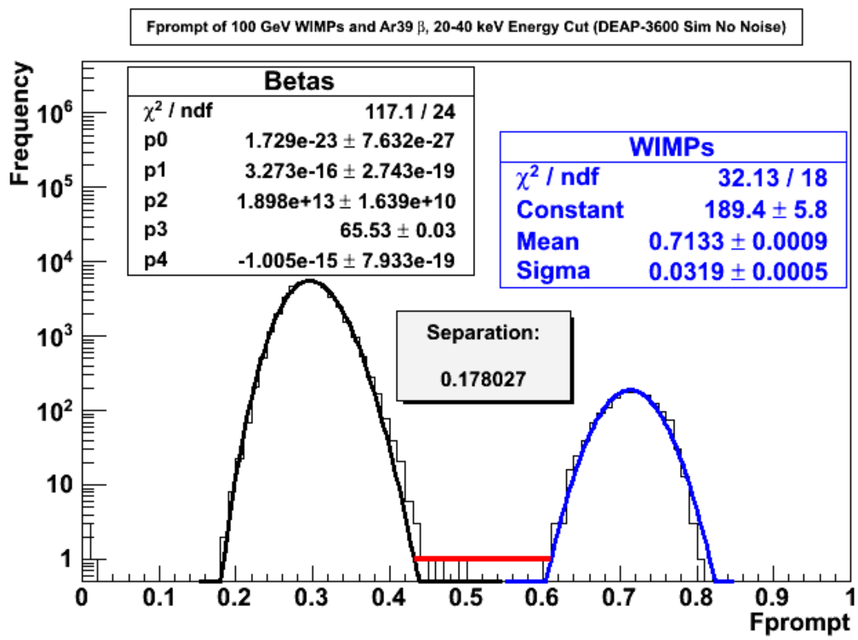


Figure 5.7: $F_{prompt}$ distribution for $^{39}$Ar $\beta$ events and 100 GeV·c$^{-2}$ WIMPs falling in the 20 - 40 keV deposited energy range.

As an example, Figure 5.7 shows the results for the 20 - 40 keV energy range where the simulated waveforms have no noise added. The WIMP distributions (high $F_{prompt}$ peak) are fit with Gaussian functions (shown in blue). However, a Gaussian distribution does not conform well to the $^{39}$Ar $\beta$ distribution on the high $F_{prompt}$ side due to the tail of the $^{39}$Ar $\beta$-decay distribution in this energy range. To provide a better description of the $^{39}$Ar distribution a power-law multiplied by a Maxwell-Boltzmann-like distribution was used (fit shown by black line in Figure 5.7) given by:

$$f(x) = \frac{x^{p_3}}{(p_0)^3} e^{\frac{-(p_4 \cdot x - p_1)^2}{(p_2 \cdot p_0^2)}} \tag{5.2}$$

where $p_0$, $p_1$, $p_2$, $p_3$, and $p_4$ are fit parameters. This equation was chosen because it resembles a Gaussian distribution with an asymmetric high side tail. After the respective functions were fit to the $^{39}$Ar $\beta$-decay and WIMP distributions, the two fits were extrapolated to locate the point of intersection of the two functions. The frequency of $^{39}$Ar events at the intersection point is then calculated. A ratio of the calculated maximum of the $^{39}$Ar distribution and frequency at the intersection (see Equation 5.3) is then used as a measure of the discrimination power (related to distribution separation):

$$D = \frac{P_{intersection}}{P_{maximum}} \quad . \tag{5.3}$$

Figure 5.8 shows the 20 - 40 keV energy range $F_{prompt}$ distributions with the fits extrapolated down to their point of intersection.

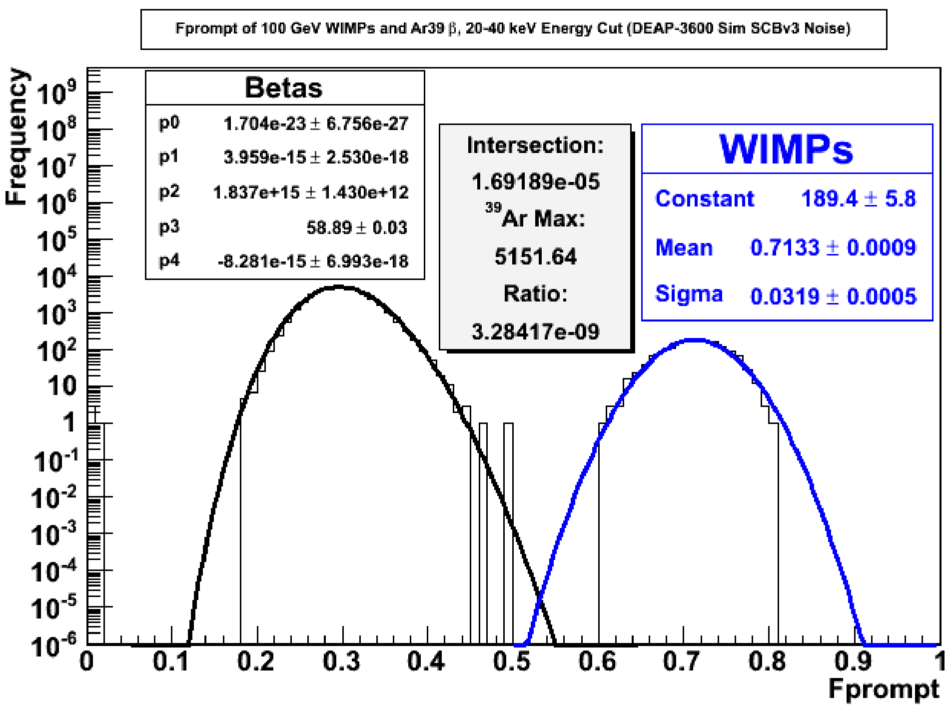


Figure 5.8: $F_{prompt}$ distribution for $^{39}$Ar $\beta$ events and 100 GeV$\cdot$c$^{-2}$ WIMPs falling in the 20 - 40 keV deposited energy range, with the fits extrapolated to determine the intersection points.

Figure 5.8 also indicates the y-axis values of the fit functions intersection point, the $^{39}$Ar distribution maximum, and the ratio of those two numbers from Equation 5.3. The statistics boxes labelled "Betas" and "WIMPs" display the fit results of Equation 5.2 for the $^{39}$Ar distribution, and the fit results of a Gaussian distribution for the WIMPs. The two $^{39}$Ar $\beta$ outliers located near $F_{prompt} \approx 0.5$ are discussed in the next subsection. Figure 5.9 shows the results of the $F_{prompt}$ projection for the 40 - 80 keV energy range.

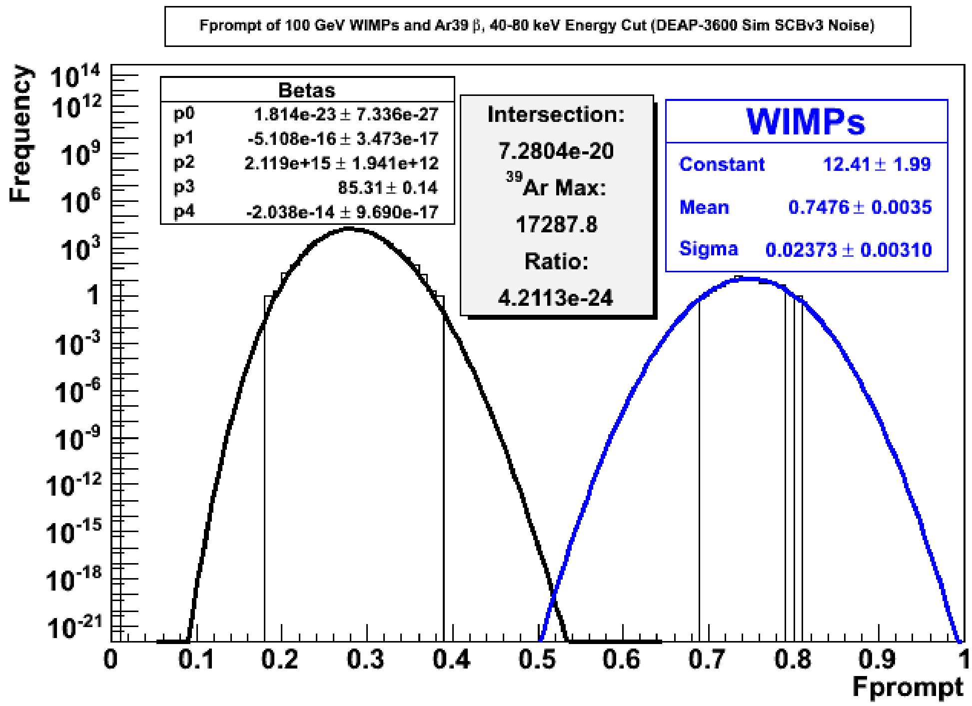


Figure 5.9: $F_{prompt}$ distribution for $^{39}$Ar $\beta$ events and 100 GeV·c$^{-2}$ WIMPs falling in the 40 - 80 keV deposited energy range, with the fits extrapolated to determine the intersection points.

These distributions change a small amount for different simulated electronics noise levels. The ratio, described in Equation 5.3, is an indicator of the detector performance for a given noise level, where a smaller D value indicates a higher discrimination power for that energy range. The values of D for the five simulated noise levels are shown for the two energy ranges in Table 5.2.

Table 5.2 shows that for the 20 - 40 keV energy range, the best detector performance (lowest value of D) occurs with the no noise scenario. The worst detector performance (highest value of D) occurs for the largest amount of noise added to the simulated waveforms: the 0.700 mV RMS noise level. The difference between the value of D for the realistic noise (SCBv3) and the lowest

Table 5.2: $F_{prompt}$ distribution separation parameters for simulated $^{39}$Ar $\beta$s and WIMPs with various electronics noise levels. $\sigma_N$ is the standard deviation of the noise distribution which was added to the simulated waveforms. D is the ratio described in Equation 5.3.

| Noise, $\sigma_N$ [mV] | Energy Range [keV] | D |
|---|---|---|
| None, 0.0 | 20-40 | $1.864\times10^{-9}$ |
| | 40-80 | $5.715\times10^{-25}$ |
| V1720, 0.446 | 20-40 | $2.479\times10^{-9}$ |
| | 40-80 | $1.959\times10^{-24}$ |
| Gaussian, 0.470 | 20-40 | $1.881\times10^{-9}$ |
| | 40-80 | $5.234\times10^{-25}$ |
| SCBv3, 0.470 | 20-40 | $3.284\times10^{-9}$ |
| | 40-80 | $4.211\times10^{-24}$ |
| Gaussian, 0.700 | 20-40 | $1.493\times10^{-8}$ |
| | 40-80 | $2.287\times10^{-24}$ |

realistically achievable noise level (V1720) is $\approx$ 25%.

For the 40 - 80 keV range, the detector performance improves dramatically when compared with the 20 - 40 keV range. This is expected, since the distributions for the higher energy WIMPs and $^{39}$Ar $\beta$ events have smaller widths, and the means have larger separation than found in the lower energy range. It is only near the detector threshold (20 keVee) that the $^{39}$Ar $\beta$ events have a high probability of leaking into the WIMP region of interest. Within the 40 - 80 keV energy range, the two lowest values of D (best detector performance) are the no noise and 0.470 mV RMS Gaussian noise. The two highest values of D (worst detector performance) are the SCBv3 and 0.700 mV RMS noise levels. This result implies that the large noise level (simulated to be about double the SCBv3 level) has less of an impact on the overall discrimination power in this energy range. The relative sizes of D for the various noise levels within the 40 - 80 keV range are less important than their size relative to the 20 - 40 keV values of D. The detector performs better in the 40 - 80 keV range than in the lower energy range, as indicated by the D value which is smaller by $\sim 15$ orders of magnitude. This result implies the discrimination power is much greater in the higher energy range, owing to the large separation in mean and small widths of the WIMP and $^{39}$Ar $\beta$-decay $F_{prompt}$ distributions.

### 5.6.1 $^{39}$Ar $\beta$ Distribution, 20 - 40 keV Energy Range Outliers

In Figure 5.8 there are two outliers which fall outside the $^{39}$Ar $\beta$ fit distribution curve. It is hypothesised that these events are from $\beta$s which have energies close to the threshold of the detector (20 keVee). At these very low energies events may leak into the "inter-peak" region from the tail of the full $^{39}$Ar distribution which begins to widen significantly (see Figure 5.6 for reference). To test this hypothesis, the $F_{prompt}$ projection of a series of energy ranges was plotted (see Figure 5.10).

It is observed that increasing the energy threshold by 1 keV (to 21 keVee) removes the two outliers from between the distributions, thus confirming the above hypothesis. In the physical DEAP-3600 detector the energy threshold will be determined following calibrations to determine the ideal threshold.

## 5.7 Effect of Noise on Detector Efficiency

### 5.7.1 Monte Carlo Event Energy versus Detected Event Charge

To determine the effect of electronics noise on the detector efficiency, the "true" event energy generated by the Monte Carlo simulation is plotted versus the "detected" event charge for varying levels of noise. The reconstructed event charge (QPE, or charge in photoelectrons) is found by counting all of the PE which are detected by the simulated PMTs. QPE can then be converted to event energy via the light yield which averages 11.3 PE/keV for this simulation.

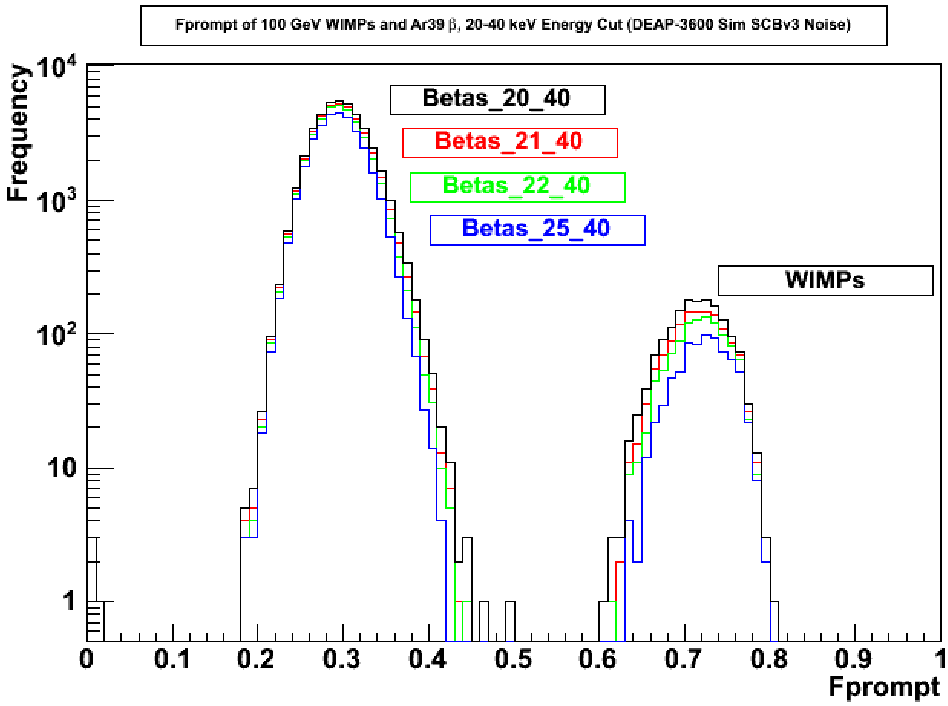


Figure 5.10: The $F_{prompt}$ projection plots for the lower energy range considered, with various detector thresholds used as the lower bound of the range. Black, red, green, and blue curves represent the 20, 21, 22, and 25 keV lower bound (energy threshold) respectively.

By plotting the true Monte Carlo event energy ($\mathrm{MC}_{KE}$) of $^{39}$Ar $\beta$-decays versus the reconstructed event charge ($EV_{QPE}$) and fitting a straight line to the data, one obtains a slope:

$$MC_{KE} = p1 \cdot EV_{QPE} + p0 \quad . \tag{5.4}$$

This slope may be converted into a measurement of the energy efficiency via:

$$\epsilon = p1 \cdot \mathrm{LY} \; , \tag{5.5}$$

where $\epsilon$ is detector energy efficiency, and LY is the light yield conversion factor. The energy efficiency of the detector for various levels of electronics noise is investigated in the following section.

### 5.7.2 Results for Five Noise Levels

A sample plot of $MC_{KE}$ (in keV) versus detected photoelectrons (in QPE) is shown in Figure 5.11. The result of the linear fit is shown by the black line, and the slope (p1) and intercept (p0) returned by the fit are shown in the statistics box. Multiplying the slope with the light yield provides a measure of detector efficiency, where $\epsilon = 1.0$ corresponds to 100% energy detection efficiency.

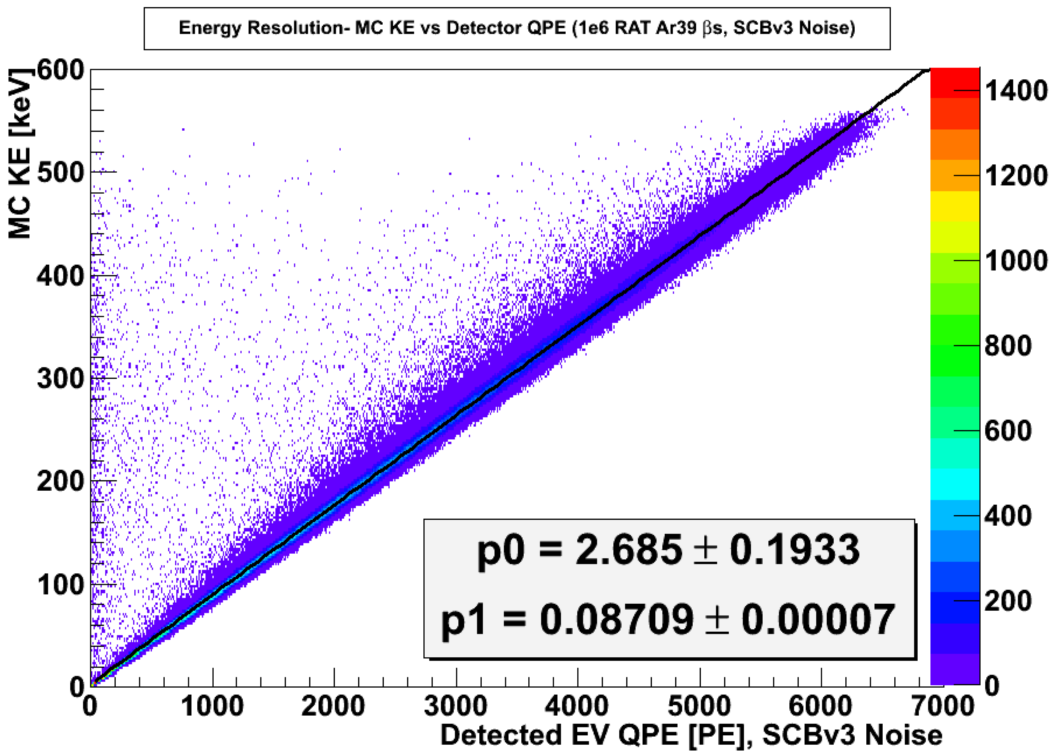


Figure 5.11: “True” Monte Carlo event energy in keV of $^{39}Ar$ $\beta$-decays plotted versus reconstructed event energy in QPE (based on detected number of photoelectrons). A linear fit shown in black.

The results of the $MC_{KE}$ versus event charge study are summarised in Table 5.3. The highest value for simulated energy efficiency comes from the scenario of no noise added to the waveforms, which is reasonable since one would expect a perfect electronics system to enhance energy detection efficiency. The difference in energy efficiency for the three realistic noise levels (SCBv3, V1720, and 0.470 mV RMS) is less than 0.05%. An unexpected increase in the noise

Table 5.3: Simulated detector energy efficiency for various levels of waveform noise added to $^{39}$Ar $\beta$-decay events.

| Noise, RMS [mV] | p0 | p1 | $\epsilon$ |
|---|---|---|---|
| None, 0.0 | 2.635 ± 0.193 | 8.714 ± 0.007 $\times 10^{-2}$ | 9.8468$\times 10^{-1}$ |
| V1720 | 2.681 ± 0.193 | 8.713 ± 0.007 $\times 10^{-2}$ | 9.8457$\times 10^{-1}$ |
| SCBv3 | 2.685 ± 0.193 | 8.709 ± 0.007 $\times 10^{-2}$ | 9.8412$\times 10^{-1}$ |
| Gaus, 0.47 | 2.624 ± 0.193 | 8.710 ± 0.007 $\times 10^{-2}$ | 9.8423$\times 10^{-1}$ |
| Gaus, 0.70 | 0.013 ± 0.195 | 8.685 ± 0.007 $\times 10^{-2}$ | 9.8141$\times 10^{-1}$ |

distribution RMS (simulated by the 0.700 mV RMS scenario) would reduce the energy efficiency by 0.28%. Comparing the V1720 noise to the current SCBv3 noise implies that the energy detection efficiency of the detector could be improved by 0.046% by reducing the noise to the lowest realistically achievable level.

### 5.7.3 Radial Distribution of $MC_{KE}$ vs QPE Outliers

The outliers shown in Figure 5.11, which are well above the linear fit, belong to a class of events which have a severely under-estimated detected event energy. This under-estimation is believed to originate from events that experience partial light detection due to the less than 100% photocoverage of the experiment. This would be true for events that occur at large radii (with respect to the centre of the DEAP-3600 acrylic vessel), where there is an increased probability of light escaping the detector through the spaces between light guides. Included in the class of large-radius events are those which occur in the acrylic neck of the detector (see Figure 5.1, shown in dark blue), or in the region directly below the neck. The acrylic neck provides a path for the argon recirculation system, and $^{39}$Ar $\beta$-decays occurring in this region may only have a small portion of their total light detected, due to their distance away from the focus point of the PMT light guides.

To test the hypothesis that the outliers are due to large radius events, a

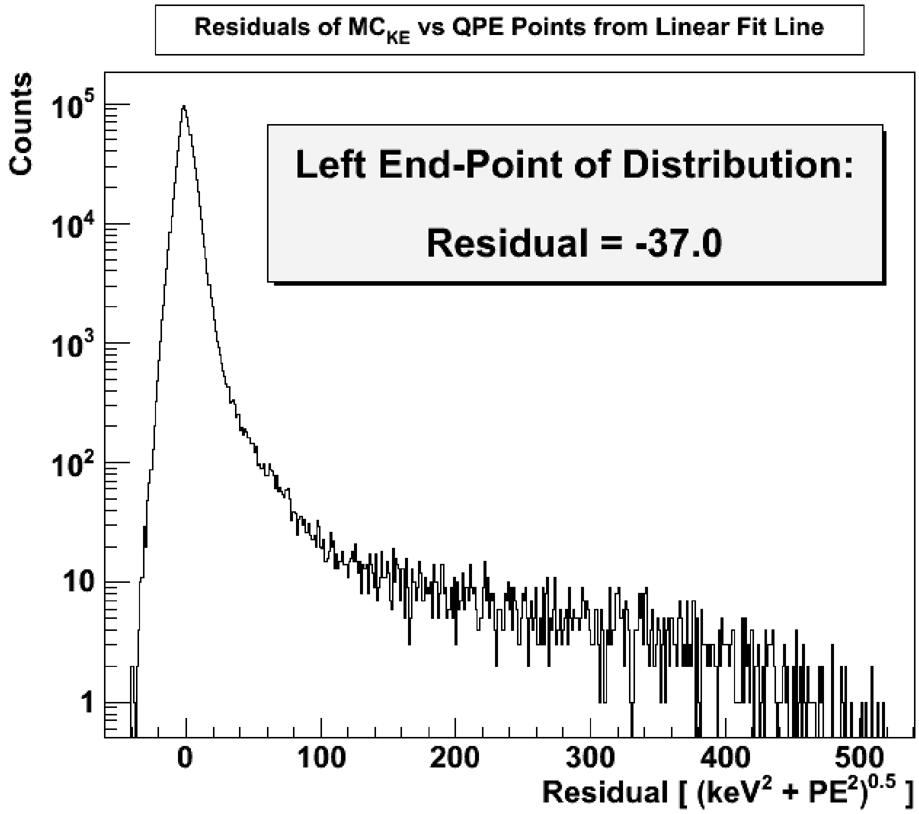


Figure 5.12: Residual (distance of closest approach) of $^{39}$Ar $MC_{KE}$ vs QPE points from linear fit line. Left end-point of distribution is at -37.0.

cut is placed on the $MC_{KE}$ vs QPE histogram. To determine where to place this cut, the outliers were defined using a residual of each point in the $MC_{KE}$ vs QPE space, as shown in Figure 5.12. The residual was calculated as the distance of closest approach of each event point and the linear fit line (black) shown in Figure 5.11. Figure 5.12 shows that for data points below the linear fit, the residuals are as large as -37.0, and the tail of the distribution is composed of the outlier events. Assuming an outlier is an event outside a symmetric distribution about the linear fit, the cut line is placed at 37.0 keV *above* the fit line (see the red cut line in Figure 5.13).

With the outliers clearly defined, the radius-cubed of each simulated $^{39}$Ar $\beta$-decay was plotted (see Figure 5.14). Radius is measured in meters from the centre of DEAP-3600. The $R^3$ event distribution is flat from the centre of

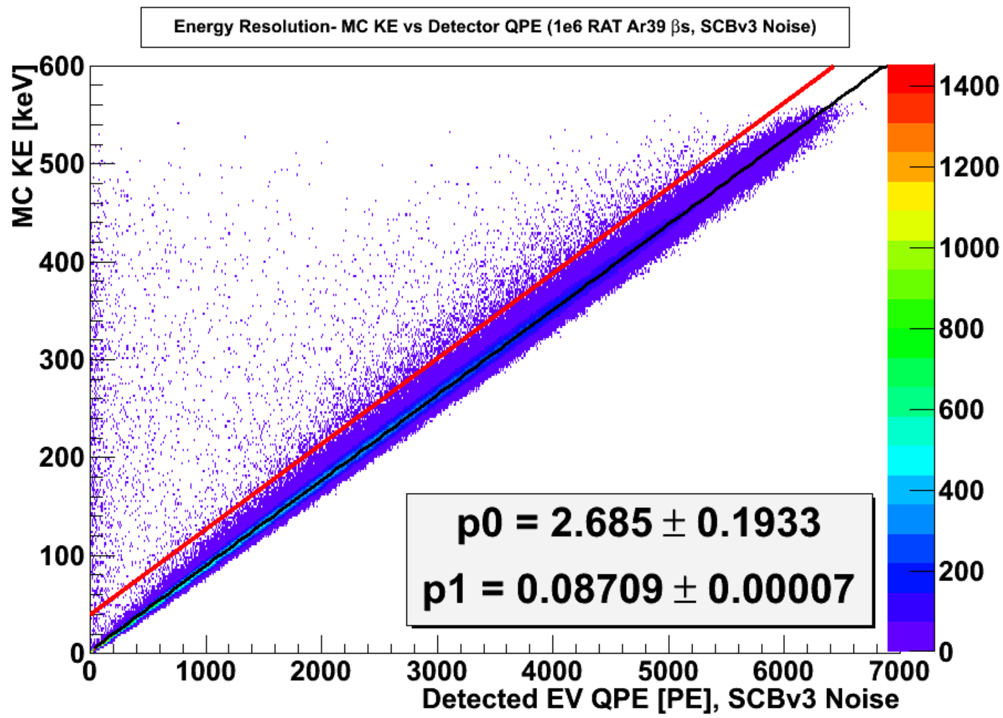


Figure 5.13: Monte Carlo event energy of $^{39}$Ar $\beta$-decays versus detected event energy for events with SCBv3 noise added to waveforms. A linear fit shown in black, and the cut defining the outliers is shown in red.

the acrylic vessel ($R^3 = 0$) to the inner acrylic surface (at $R^3 \approx 0.614$ m$^3$). Events occurring at $R^3$ greater than 0.614 m$^3$ are from $\beta$-decays in the acrylic neck. Recall that $\beta$-decays occur at any location in the detector where LAr is present, including the acrylic neck (which is used for Ar recirculation). A Cartesian cross-section (Z vs X position) of the simulated $^{39}$Ar $\beta$-decays within the DEAP-3600 vessel is shown in Figure 5.16. The coordinate system of the Z vs X plot is centred (0,0) at the centre of the DEAP vessel, and the dimensions are in meters.

Next, the $R^3$ of events falling above the cut line (outliers) are plotted in Figure 5.15. The $R^3$ distribution of the outlier events confirms the hypothesis that the incomplete energy detection of these events is correlated with the radial position. That is, the outlier events all occur at large radii. The peak of the outlier $R^3$ distribution is located at $\approx 0.614$ m, corresponding to

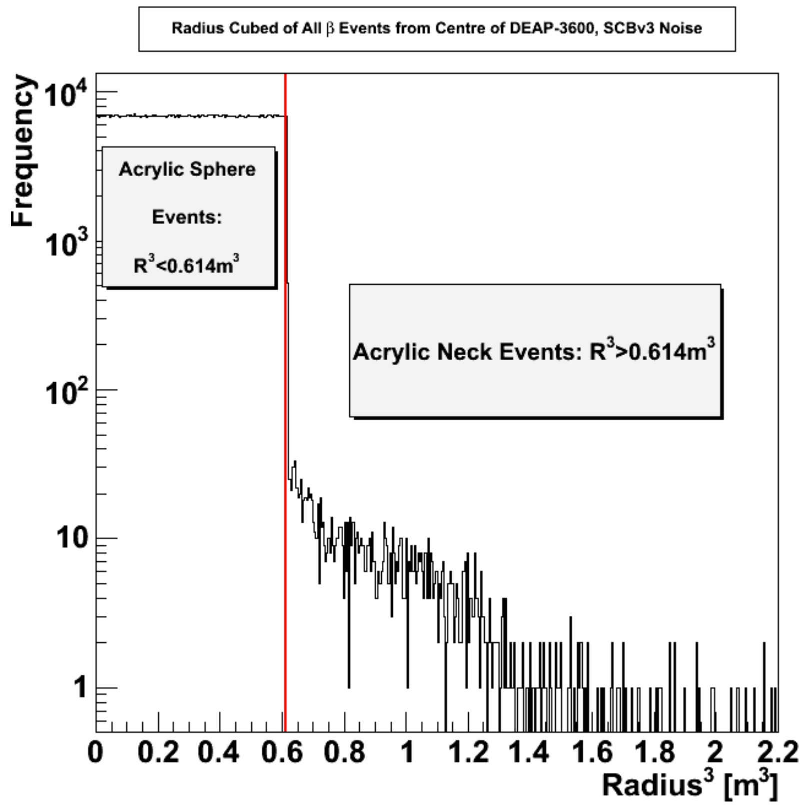


Figure 5.14: $R^3$ from centre of DEAP-3600 for all simulated $^{39}$Ar $\beta$-decay events. A red line shows the location of the inner acrylic surface of the vessel.

events occurring near the inner surface of the acrylic vessel. The neck events ($R^3 \geq 0.614$ m) are also included in the $R^3$ outlier distribution. The blue line shown in Figure 5.15 indicates the fiducial volume cut which DEAP-3600 has set as a goal ($R^3 \approx 0.176$ m$^3$) for an active target volume of 1000 kg LAr. To aid in the visualisation of the location of outlier events, their X-Z location is plotted in Figure 5.17, confirming that the majority of the outlier events occur near the neck region (X = 0 m, Z = 0.9 m). Figure 5.17 also implies that the outliers which occur at large radii but not in the neck (events to the left of the peak in Figure 5.15) are not evenly distributed around the detector, but are preferentially located in the top portion of the detector near the neck. This is the location in DEAP-3600 where photocoverage is most limited, due to the lack of local light guides and PMTs.

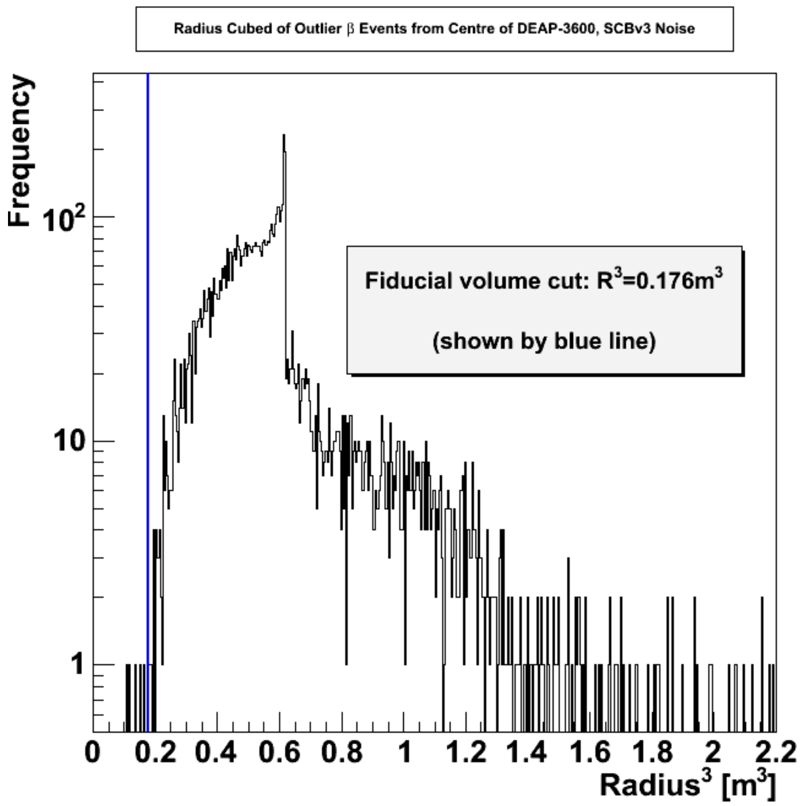


Figure 5.15: $R^3$ of the $MC_{KE}$ vs QPE outlier events. Fiducial volume cut indicated with a blue line. The outlier events appear to be large radii inner vessel events, as well as neck events.

Out of the total number of $^{39}$Ar $\beta$ events simulated ($\sim 10^6$) about 0.66% events were defined as outliers. Of these outliers, less than 0.1% fall within the fiducial region. Once DEAP-3600 has removed the majority of the outlier energy events with the radial cut to define the fiducial volume, remaining outlier events will be removed using the $F_{prompt}$ and energy cuts.

## 5.8 Concluding Remarks

The purpose of the simulation studies was to use information gathered from the electronics testbed to simulate the effect of the electronics noise on the DEAP-3600 detector's performance. Other noise levels (not based on the electronics testbed) were simulated to provide context for the results with respect to a

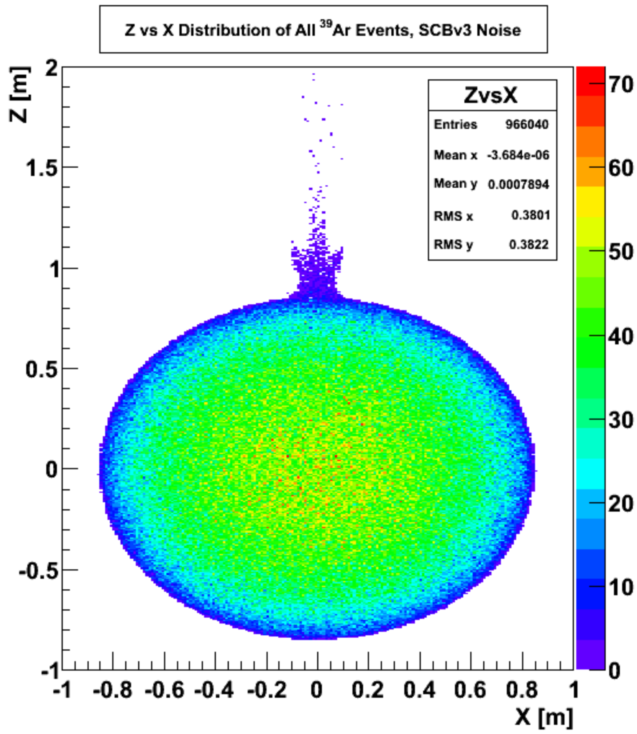


Figure 5.16: X vs Z positions of all simulated $^{39}$Ar $\beta$-decays. Recall that the $\beta$-decays may occur anywhere in the detector that contains argon, including the acrylic neck region which is used for argon recirculation.

perfect electronics system (no noise), and a hypothetical increase in noise from current design levels (0.700 mV RMS). It was shown that electronics noise can shift the overall values of $F_{prompt}$ for 100 GeV·c$^{-2}$ WIMPs by a significant amount if the noise level exceeds 0.6 mV RMS. Electronics noise levels of 0.7 mV RMS reduce the mean of the $F_{prompt}$ distribution of $^{39}$Ar $\beta$-decay events, as well as alter the distribution shape, when compared to the events generated with noise levels on the level of 0 to 0.5 mV RMS. If noise levels increased in amplitude by $\sim$ 50%, with respect to distribution RMS, it would negatively impact the ability of DEAP-3600 to separate WIMPs from background events in the lowest energy range considered, 20 - 40 keV. The current noise level leads to a separation between WIMPs and $^{39}$Ar $\beta$-decays which could be improved in the 20 - 40 keV energy range by lowering the noise to a level where it is limited by the CAEN V1720. The detector simulation shows WIMP signals

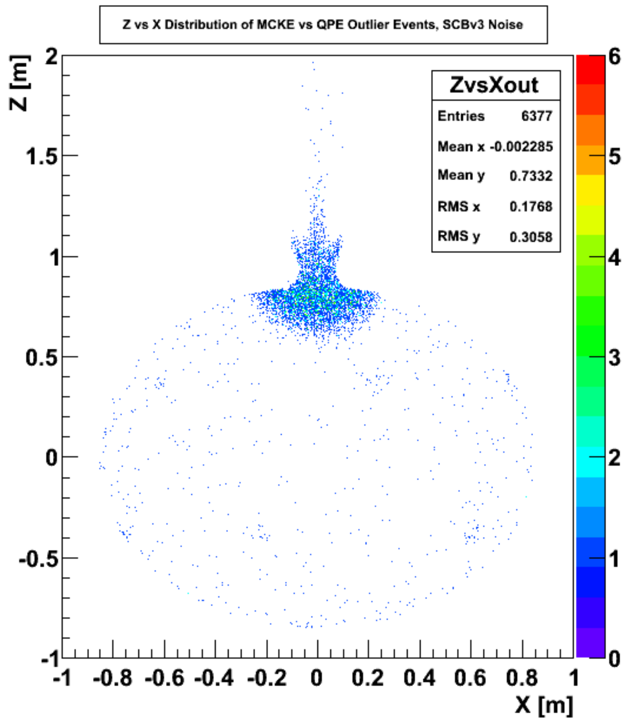


Figure 5.17: X vs Z positions of simulated $^{39}$Ar $\beta$-decay outlier events. Note that the outliers predominantly occur near the top region of the detector.

will be easiest to separate from background in the 40 - 80 keV range studied.

The current level of noise generated by the SCBv3 decreases the simulated detected energy efficiency of DEAP-3600 by $\sim 0.05\%$ compared with the lowest realistically achievable noise level from the V1720 digitiser only. An increase in noise amplitude RMS by $\sim 50\%$ would reduce the detected energy efficiency by about 0.3%. The simulation indicates the electronics noise should not negatively impact the DEAP-3600 detector with respect to signal extraction, and electronics noise should be kept at the current level or, if possible further reduced, to enhance the detector energy efficiency. The simulation also revealed that events occurring at large radii, specifically in the neck region, may have poorly resolved energy due to incomplete light detection. These large radius events may be removed from the DEAP-3600 data by the combination of fiducial volume, $F_{prompt}$, and energy cuts.

# Chapter 6

# Conclusion

DEAP-3600 aims to be one of the world's first tonne-scale direct detection dark matter experiments. It will search for dark matter in the form of weakly interacting massive particles. To facilitate the detection of photons from the liquid argon scintillation detector, signal conditioning boards will be used as a electrical pulse shaping tool. The SCBs assist in maximising single photoelectron detection, which ultimately enhances the detected energy efficiency and discrimination power of the detector.

Results from a direct detection dark matter search are often displayed in a cross section versus WIMP mass phase space. The curves traditionally found in this space represent a region above which a WIMP detection is excluded by an experiment. If WIMPs are detected, a region may be identified in the parameter space where the WIMP mass and cross section are permitted. An example of a spin-independent parameter space with the world's current leading result (XENON-100), as well as DEAP-3600's projected sensitivity after three years of background-free running, is shown in Figure 6.1. The figure shows that DEAP-3600 will explore the range of WIMP cross sections reaching as low as $10^{-46}$ cm$^2$ for WIMP masses of about 100 GeV$\cdot$c$^{-2}$ [67]. Also included in Figure 6.1 is the projected sensitivity of DEAP-3600 when operating with argon reduced in levels of $^{39}$Ar, referred to as depleted argon, which permits a lower energy threshold to be obtained. Exclusion curves typically rise quickly at low WIMP mass, which is a reflection of the individual detector's energy threshold.

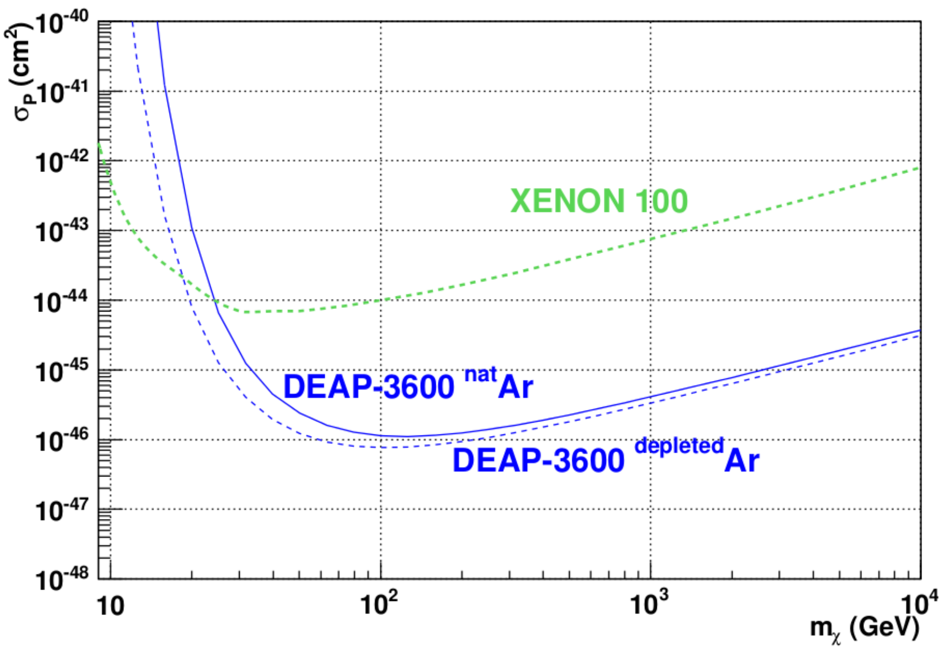


Figure 6.1: WIMP mass versus cross section exclusion plot for projected DEAP-3600 sensitivity [79]. Current leading exclusion limit (May 2012) set by XENON-100 collaboration (with 100 days exposure time) shown for reference.

The achievement of the blue exclusion curve shown in Figure 6.1 depends on DEAP-3600 successfully discriminating background and signal events above the 20 keV detected energy threshold. This thesis discussed testing of the SCBs which will help enhance the DEAP-3600 SPE detection and energy efficiency, to ultimately be able to explore the desired parameter space shown in the exclusion plot. SCB testing was an iterative process, with successively improving versions being designed and fabricated. Through primary testing of the SCBs, improvements have been implemented toward the final design. The final SCB will have high gain channels with 4.7 nF coupling capacitors, a 6 ns time constant for pulse shaping, and use the AD8001 amplifier. The noise levels on the last version of the tested boards are low enough to facilitate accurate single photoelectron detection at a level of 0.016 PE for the 4 ns time bin. The SCB was shown to behave in an acceptable fashion with respect to pulse shape and charge distributions, with an amplifier change helping to reduce a changing pulse shape with pulse height issue on the HG channel. The specifications for signal to noise ratio were found to meet design goals at the current level of $S2N \approx 64$. The SCB low gain channel saturates the digitiser at $\approx$ 10,000 PE, which is large enough to permit the study of large light events like alpha decays on the inner surface of the DEAP detector. The high gain and low gain channel of the SCB displays clear linear correlations which will allow for efficient calibration of the detector at run-time.

The thesis outlined the procedure and results of simulations performed using the RAT analysis software. The simulation was initialised with information about the electronics noise levels which DEAP-3600 will experience. The simulation indicated that noise levels of the current electronics setup of DEAP should not significantly affect the ability of the detector to separate a WIMP signal from the expected dominant background $^{39}$Ar $\beta$ decays. The simulation also revealed that an electronics noise that exceeds $\sim$ 0.6 mV RMS may dramatically affect the detector performance with respect to the expected WIMP and $^{39}$Ar $\beta$ decay $F_{prompt}$ distributions. However, the current electronics noise is below this level ($\sim$ 0.47 mV RMS), and in the energy range of 20 - 40 keV (detected event energy) the simulated $F_{prompt}$ distributions for signal and background are found to be well separated. The detector may experience a small increase in discrimination power in the lowest energy range (20 - 40 keV) if the electronics noise is reduced to a level where it is limited to the commercial device used for digitiser (V1720). The simulated detected energy efficiency of DEAP-3600 with current noise levels was also found to be within 0.05% of the level that is as low as realistically achievable. The detector energy efficiency from the simulation with the current electronic noise levels is $\sim$ 98.4%. The simulated energy efficiency study also revealed a population of outlier events which had lower detected energy than true event energy. These events were confirmed to be from $^{39}$Ar $\beta$ decays occurring at large radii, and in the acrylic neck region of the detector. It is believed that these events will be successfully removed from the DEAP-3600 data with a fiducial volume cut, which removes events occurring at reconstructed radii $\geq 0.56$ m, combined with $F_{prompt}$ and energy cuts.

With the primary testing of the prototype SCBs complete, the 32 final boards are now being produced. Acceptance testing for each, similar to that described in this thesis, will ensure the performance is adequate with respect to pulse shape and noise level. An initial simulation study has shown the electronics noise should not affect DEAP's expected discrimination power. Further simulation work is needed to incorporate the final SCB response function in the DAQ processing, and the effect of different types of pulse finding algorithms on the detector performance. The effect of changing the WIMP mass on $F_{prompt}$ distribution should also be simulated to provide an estimate of DEAP's discrimination power for a range of WIMP masses. Finally, a large scale simulation, on the order of $10^8$ to $10^9$ events, should be performed with a full electronics response to determine the lowest possible energy threshold DEAP could have while maintaining a discrimination power of $10^{-10}$.

# Bibliography


[1] Zwicky, F. Die Rotverschiebung von extragalaktischen Nebeln. *Helvetica Physica Acta*, 6:110–127, 1933.

[2] Spergel, D.N., *et al*. Three-year Wilkinson Microwave Anisotropy Probe (WMAP) observations implications for cosmology. *The Astrophysical Journal Supplement Series*, (170):377–408, 2007.

[3] Clark, K. A New and Improved Spin-Dependent Dark Matter Exclusion Limit Using the PICASSO Experiment. *PhD Thesis*, 2008.

[4] Acharya, B. S., Kane, G., Watson, S., Kumar, P. Nonthermal "WIMP miracle". *Physical Review D*, (80):083529, 2009.

[5] Capozziello, S., Consiglio, L., De Laurentis, M., De Rose, G., Di Donato, C. The missing matter problem: from the dark matter search to alternative hypothesis. *arXiv eprints, 1110.502v6*, 2011.

[6] Blumenthal, G. R., Faber, S. M., Primack, J., Rees, M. Formation of galaxies and large scale structure with cold dark matter. *Nature*, 1984.

[7] Rubin, V., Ford, W. K. Jr. Rotation of the Andromeda Nebula from a Spectroscopic Survey of Emission Regions. *Astrophysical Journal*, (159): 379–403, 1970.

[8] *http://bustard.phys.nd.edu/Phys171/lectures/dm.html*.

[9] Begeman, K.G. HI rotation curves of spiral galaxies. *Astronomy and Astrophysics*, (223):47–60, 1989.

[10] Ashman, K. M. Dark Matter in Galaxies. *Pub. Astronomical Society of Pacific*, (104):1109–1138, 1992.

[11] Casertano, S., van Gorkom, J. H. Declining Rotation Curves: the End of a Conspiracy? *Astronomical Journal*, (101):1231–1242, 1991.

[12] Sahu, S., Patil, M., Narasumha, D, and Joshi, P.S. Can strong gravitational lensing distinguish naked singularities from black holes? *Physical Review D*, 86(063010), 2012.

[13] NASA, ESA & L. Calçada. http://astronomy.com/, 2012.

[14] Dyson, Sir F. W., Eddignton, A.S., and Davidson, C. A Determination of the Deflection of Light by the Sun's Gravitational Field, from Observations made at the Total Eclipse of May 29, 1919. *Philosophical Transactions of the Royal Society of London*, Series A, 1919.

[15] Ellis, R.S. Gravitational lensing: a unique probe of dark matter and energy. *Philosophical Transactions of the Royal Society*, (368):967–987, 2010.

[16] Hubble Space Telescope. *http://apod.nasa.gov/apod/image/0110/a2218c_hst_big.jpg*.

[17] Grillo, C. Projected central dark matter fractions and densities in massive early-type galaxies from the SLOAN Digital Sky Survey. *Astrophysical Journal*, (722):779–787, 2010.

[18] Clowe, D., Bradac, M., Gonzalez, A. H., Markevitch, M., Randall, S. W., Jones, C., Zaritsky, D. A Direct Empirical Proof of the Existence of Dark Matter. *Astrophysical Journal*, (648):L109–L113, 2006.

[19] Massey, R. Cal-tech, National Aeronautics and Space Administration, European Space Agency. *http://www.space.com/3319-astronomers-create-3d-map-dark-matter.html*, 2010.

[20] Massey, R., *et al*. Dark matter maps reveal cosmic scaffolding. *Nature 05497*, 2007.

[21] Springel, V., *et al*. Simulations of the formation, evolution, and clustering of galaxies and quasars. *Nature 03597*, 2005.

[22] Bennett, C.L., *et al*. First Year Wilkinson Microwave Anisotropy Probe (WMAP1) Observations: Preliminary Maps and Basic Results. *Astronomical Journal Supplement Series*, 148(101):1–27, 2003.

[23] Bennett, C.L., *et al*. Cosmic temperature fluctuations from two years of COBE differential microwave radiometers observations. *Astronomical Journal*, 436(2):423–442, 1994.

[24] Bertone, G. Particle Dark Matter. *Cambridge University Press*, 2010.

[25] Nakamura, K., *et al*. Cosmic Microwave Background. *Particle Data Group Review*, 075021(JP G 37), 2011.

[26] Komatsu, E., *et al*. Seven Year Wilkinson Microwave Anisotropy Probe (WMAP) Observations: Cosmological Interpretation. *Astronomical Journal Supplement Series*, 192(2), 2011.

[27] Vergados, J.D., Owen, D. Direct Dark Matter Event Rates with a Velocity Distribution in the Eddington Approach. *arXiv eprints, 0603.3704v2*, 2006.

[28] Bertone, G. The moment of truth for WIMP dark matter. *Nature Review 09509*, (468):389–393, 2010.

[29] Feng, J. Dark Matter Candidates from Particle Physics and Methods of Detection. *Annual Review of Astronomy and Astrophysics*, 48:495–545, 2010.

[30] Jungman, G., Kamionkowski, M., Griest, K. Supersymmetric Dark Matter. *Physics Reports*, (267):195–373, 1996.

[31] Beringer, J., *et al*. Supersymmetry, Part I (Theory), *http://pdg.lbl.gov*. *Particle Data Group Review*, (D86), 2012.

[32] Cirelli, M. Indirect searches for dark matter: a status review. *Pramana Journal of Physics*, 2012.

[33] Kavanagh, B. J. and Green, A. M. Improved determination of the WIMP mass from direct detection data. *Physical Review D*, 065027(86), 2012.

[34] Chung-Lin, S. Estimating the Spin–Independent WIMP–Nucleon Coupling from Direct Dark Matter Detection Data . *arXiv eprints, 1103.481v2*, 2011.

[35] Schumann, M. Dark Matter Search with Liquid Noble Gases. *arXiv eprints, 1206.2169v1*, June 2012.

[36] Hime, A., Boulay, M.G. Techniques for direct detection of weakly interacting massive particles using scintillation time discrimination in liquid argon. *Astroparticle Physics*, (25):179–182, 2006.

[37] Hennings-Yeomans, R. for DEAP/CLEAN Collaboration. Direct Detection of Dark Matter with MiniCLEAN. *Journal of Physics: Conference Series*, (315), 2010.

[38] Chemicool.com. Chemicool Periodic Table. *http://www.chemicool.com/elements/neon.html*, 2011.

[39] Nikkel, J.A., Gozani, T., Brown, C., Kwong, J., McKinsey, D.N., Shin, Y., Kane, S., Gary, C., Firestone, M. Liquified Noble Gas (LNG) detectors for detection of nuclear materials. *2nd International Workshop on Fast Neutron Detectors and Applications*, 2012.

[40] Gascon, J., Lyon, V.S.I, Lemrani, R. Dark matter online tools. *http://pisrv0.pit.physik.uni-tuebingen.de/darkmatter/.*

[41] Solovov., V.N., *et al*. Position Reconstruction in a Dual Phase Xenon Scintillation Detector. *arXiv eprints, 1112.1481v1*, 2011.

[42] Aprile, E., *et al.* (The XENON100 Collaboration). Dark Matter Results from 100 Live Days of XENON100 Data. *Physics Review Letters*, (107): 131302, 2011.

[43] Akerib, D.S., *et al.* (LUX Collaboration). Data Acquisition and readout system for the LUX dark matter experiment. *Nuclear Instruments and Methods in Physics Research A*, (668):1–8, 2012.

[44] Doke, T., Hitachi, A., Kikuchi, J., Masuda, K., Okada, H., Shibamura, E. Absolute Scintillation Yields in Liquid Argon and Xenon for Various Particles. *Japan Society of Applied Physics*, (41):1538–1545, 2002.

[45] Gaster, D., *et al*. Measurement of scintillation efficiency for nuclear recoils in liquid argon. *arXiv eprints, 1004.0373v3*, 2012.

[46] Behnke, E., Behnke, J., Conner, A., Grace, E., Levine, I. Moan, T., Nania, T., *et al*. First Dark Matter Search Results from a 4-kg CF3I Bubble Chamber Operated in a Deep Underground Site. *arXiv eprints, 1204.3094v1*, 2012.

[47] Aharmim, B., *et al.* (SNO Collaboration). Measurement of the Cosmic Ray and Neutrino-Induced Muon Flux at the Sudbury Neutrino Observatory. *Physical Review D*, (80):012001, 2009.

[48] Boulay, M. *http://deap.phy.queensu.ca/*, 2012.

[49] Boulay, M.,*et al*. Measurement of the scintillation time spectra and pulse shape discrimination of low-energy beta and nuclear recoils in liquid argon with DEAP-1. *arXiv eprints, 0904.2930v1*, 2009.

[50] Hime, A. for the MiniCLEAN Collaboration. The MiniCLEAN Dark Matter Experiment. *Proceedings of the DPF-2011 Conference*, 2011.

[51] McKinsey, D.N., *et al.* Fluorescence efficiences of thin scintillating films in the extreme ultraviolet spectral region. *Nuclear Instrumentations and Methods in Physics Research B*, (132):351–358, 1997.

[52] M. Boulay, B. Cai, T. Pollmann, B. Cleveland, and DEAP Collaboration. Surface backgrounds in the DEAP-3600 dark matter experiment. volume 1338 of *Topical Workshop on Low Radioactivity Techniques*, pages 137–146, 2011.

[53] Peiffer, P., Pollmann, T., Schonert, S., Smolnikov, A., Vasiliev, S. Pulse shape analysis of scintillation signals from pure and xenon-doped liquid argon for radioactive background identification. *Institute of Physics Publishing and SISSA*, 2008.

[54] Pollomann, T., Boulay, M. DEAP: Liquid argon based dark matter detection. *CAP 2012 Poster Conference*, 2012.

[55] Manalis, S., So, P., Shusteff, M,. Biological Engineering II: Instrumentation and Measurement. *MIT Open Courseware*, 2006.

[56] Leskovar, B., Lo, C.C. Single Photoelectron Time Spread Measurement of Fast Photomultipliers. *Nuclear Instruments and Methods*, (123):145–160, 1975.

[57] Olsen, K., Hallin, A., on behalf of DEAP/CLEAN Collaboration. SPE analysis of high efficiency PMTs for the DEAP-3600 dark matter detector. *Journal of Physics: Conference Series*, (312):070215, 2011.

[58] Hamamatsu Photonics R5912 Photomultiplier Tube Spec Sheet. *http://sales.hamamatsu.com/en/products/electron-tube-division/detectors/photomultiplier-tubes/part-r5912.php*, 2012.

[59] Pearson, C. High-Speed, Analog-to-Digital Converter Basics. *Texas Instruments Application Report, SLAA510*, 2011.

[60] Technical Information Manual. *Revision n. 21, MOD V1720, 8 CHANNEL 12 BIT 250 MS/s DIGITIZER*, 2012.

[61] Lockhart, R.W. How much ADC resolution do you really need? *Article by DATAQ Instruments*, 2012.

[62] *https://midas.psi.ch/htmldoc/index.html*, 2012.

[63] Mizuno, I., *et al*. Development of UV image intensifier tube with GaN photocathode. *Proceedings of SPIE*, 2008.

[64] Hamamatsu Photon Counting Guide. *Hamamatsu Photonics K.K., Electron Tube Division*, 2005.

[65] Becker, W. Advanced Time-Correlated Single Photon Counting Techniques. *Springer Series in Chemical Physics*, (81):231, 2005.

[66] Horowitz, P., Hill, W. *The Art of Electronics*. 2nd edition, 1989.

[67] Duncan, F. DEAP-3600 Conceptual Design Report. *SLDO-DEC-TR-0016*, 2011.

[68] Agostinelli, S. *et al*. (GEANT Collaboration). GEANT4- a simulation toolkit. *Nuclear Instruments and Methods in Physics Research A*, (506): 250–303, 2003.

[69] Brun, R. and Rademakers, F. ROOT - An Object Oriented Data Analysis Framework. *Nuclear Instruments and Methods in Physics Research*, A (389):81–86, 1996.

[70] *http://neutrino.phys.ksu.edu/∼GLG4sim/*.

[71] Caldwell, T. R5912-02 PMT Response Model at Cryogenic Temperatures. *DEAP-CLEAN Internal Documents*, 2012.

[72] Yokochi, R., Sturchio, N. C., Purtschert, R. Determination of crustal fluid residence times using nucleogenic $^{39}$Ar. *Geochimica et Cosmochimica Acta*, 88:19–26, 2012.

[73] McKinsey, D.N., Orzel, C. Radioactive krypton background evaluation using atom counting. *Nuclear Instruments and Methods in Physics Research*, A(545):524–531, 2005.

[74] Lidgard, J. J. Pulse Shape Discrimination Studies in Liquid Argon for the DEAP-1 Detector. *Master's Thesis*, 2008.

[75] Benetti, P. *et al*. Measurement of the specific activity of $^{39}$Ar in natural argon. *Nuclear Instruments and Methods in Physics Research*, A(574): 83–88, 2007.

[76] Smith, M. *et al*. The RAVE Survey: Constraining the Local Galactic Escape Speed. *Monthly Notices of the Royal Astronomical Society*, 379: 755–772, 2007.

[77] Kerr, F. J. and Lynden-Bell, D. Review of galactic constants. *Monthly Notices of the Royal Astronomical Society*, 221:1023–1038, 1986.

[78] Schnee, R.W. Introduction to Dark Matter Experiments. *Proceedings of the 2009 Theoretical Advanced Study Institute in Elementary Particle Physics*, pages 629–681, 2011.

[79] Boulay, M., for the DEAP Collaboration. DEAP-3600 Dark Matter Search at SNOLAB. *arXiv eprints, 1203.0604v1*, 2012.